

DESIGN OF A CARBON FIBRE PASSENGER CAR RIM

Lehoelere Frederick Maserumule

A research report submitted to the Faculty of Engineering and Built Environment of the University of the Witwatersrand in partial fulfilment of the requirements for the degree of Master of Science in Engineering.

Johannesburg 2015

Declaration

I Lehoelere Frederick Maserumule hereby declare that this research report is my own unaided work. It is being submitted to the Degree of a Masters in Science in Engineering to the University of the Witwatersrand, Johannesburg. It has not been submitted before for any degree or examination to any other University.

.....
L.F Maserumule 0505585E

..... day of,

Dedication

In memory of my late aunt Masemola Granny

Acknowledgements

I would like to acknowledge Dr Frank Kienhofer (my supervisor) for his assistance in obtaining the strain gauge experimental test results of the 1098 Ducati Rim. His supervisory role provided the necessary assistance and guidance in the key aspects of this research report.

The guidance of Craig Goodrum was also invaluable in understanding composite theory, and the manufacturing process of the rim at BlackStone Tek.

I would like to thank Makgomo Maserumule, Frank Maserumule, Tseke Maserumule, Mamagane Maserumule and Ayanda Mkhasibe for the emotional support during the research process.

Abstract

The wheel is an important component for all land transport vehicles and the following research report investigates the feasibility of a passenger car wheel manufactured from carbon fibre. Previous research, evaluated a strain gauged BlackStone Tek motorcycle Ducati rim loaded to 700 Nm on a dynamic cornering test machine. In the current study, these experimental results were used to validate an FEA model of the BlackStone Tek Ducati rim. The validated FEA was used to investigate the feasibility of using carbon fibre to manufacture a passenger car rim. The FEA model did not include the aluminium hub, and the analysis was therefore considered valid for the spokes and rim only. The FEA strains of the Ducati rim spokes were within an acceptable 25% correlation range with the experimental results. The FEA strains were generally higher than the experimental results. Having validated the FEA model, a carbon fibre passenger car rim, was analysed at a bending moment of 2000 Nm. The inverse of the factor of safety from the spoke to the rim section was below 1. This indicates that the newly designed rim should pass the dynamic cornering test, a vital standard proving that the rim is structurally durable to function on a small to medium sized passenger car. In comparison to aluminium rims of the equivalent size, a weight saving of 62.2% can be expected from a carbon fibre passenger car rim.

Table of Contents

Declaration	ii
Dedication	iii
Acknowledgements	iv
Abstract	v
Table of Contents.....	vi
List of Figures	viii
List of Tables.....	xi
List of Symbols	xii
Chapter 1: Introduction	1
1.1 Background	1
1.2 BlackStone Tek Ducati Rim	3
1.3 Wheel Test Methods.....	4
1.4 Problem Description.....	6
1.5 The Proposal.....	7
Chapter 2: General Theory	8
2.1 Design Standards for Wheels.....	9
2.2 Experimental Analysis of the Ducati Rim.....	12
2.2.1 Stress strain relationship of a lamina	12
2.2.2 Principles of strain gauging.....	14
Chapter 3: Literature Review	16
3.1 Experimental Analysis	16
3.2 Numerical Analysis.....	19
3.3 Previous Work on Composites.....	21
Chapter 4: Objectives	22
4.1 Research Scope	22
4.2 Research Outline.....	23

Chapter 5: Experimental Analysis: 1098 Ducati Rim	24
Chapter 6: FEA: 1098 Ducati Rim.....	27
6.1 Methodology.....	27
6.1.1 Model preparation	27
6.1.2 Project schematic.....	29
6.1.3 Material design	30
6.1.4 Meshing	39
6.1.5 Load cases	41
6.2 Result Evaluation: Current 1098 Ducati Rim	43
6.2.1 Strains	43
6.2.2 Maximum strain: failure criterion	48
Chapter 7: FEA – Passenger Car Rim.....	56
7.1 Ducati Rim Exposed to Passenger Vehicle Loads.....	58
7.1.1 Strains	58
7.1.2 Maximum strain failure criterion	61
7.2 Model Preparation.....	64
7.2.1 Segmentation.....	65
7.2.2 Stacking sequence.....	65
7.2.3 Meshing	71
7.3 Result Evaluation: Passenger Vehicle Rim.....	72
7.3.1 Strains	72
7.3.2 Maximum strain failure criterion	77
Chapter 8: Discussion and Conclusion.....	83
8.1 Discussion	83
8.2 Conclusion and Recommendations.....	88
References	89
Appendix A.....	94
Micromechanics of composite material.....	95

List of Figures

Figure 1: 1098 Ducati BlackStone Tek Rims [5].....	1
Figure 2: Anatomy of the BST Ducati Rim.....	4
Figure 3: Wheel Test Methods [10; 11]	5
Figure 4: Wheel Dynamic Variables [23].....	8
Figure 5: 1098 Ducati Rim Setup for Cornering Fatigue Test.....	10
Figure 6: Unidirectional Fibres [28].....	12
Figure 7: Strain Gauge Rosette [29] and Wheatstone bridge Circuit [2].....	14
Figure 8: 45 Degree Rosettes Instrumented on the Wheel [edited 11].....	17
Figure 9: Strain Gauged Ducati Rim and Experimental Setup [edited 8].....	24
Figure 10: Strain Gauge Results of 1098 Ducati Rim during One Test Run [8].....	25
Figure 11: Surface Model of the 1098 Ducati Rim.....	27
Figure 12: Illustration of 1098 Ducati Rim Inner and Outer Sections.....	28
Figure 13: Project Schematic of the FEA Analysis	29
Figure 14: Definition of Material Properties in Engineering Data.....	30
Figure 15: Rim Flange, Outer Spoke and Outer Hub of the 1098 Ducati Rim	32
Figure 16: Inner Spoke and Inner Hub of the 1098 Ducati Rim.....	32
Figure 17: Rim Flange Cosmetic, Spoke to Spoke Re-enforcement, Outer Spoke to Rim Re-enforcement of the 1098 Ducati Rim.....	33
Figure 18: Inner Spoke to Rim Re-Enforcement and Inner Spoke to Outer Spoke Re-Enforcement.....	33
Figure 19: Example of Co-ordinate Systems of Components.....	34
Figure 20: Example of Co-ordinate System for Spoke to Spoke Re-enforcements..	34
Figure 21: Material of 1098 Ducati Setup in ACP Pre Setup	35
Figure 22: ACP Pre Process: Modelling Ply Groups	35
Figure 23: Sampling Element in the Hub Section.....	36
Figure 24: Illustration of Orientated Element Sets of Rim Flange.....	37
Figure 25: Illustration of Reference Fibre Direction (Yellow Arrow) and Fibre Direction (Green Arrow)	37
Figure 26: Thickness Variation: Ducati Rim	38
Figure 27: Thickness Variation: Outer Section-Ducati Rim	38
Figure 28: Meshed Imported Layered Section of 1098 Ducati Rim (Coarse Mesh) .	39

Figure 29: Refinement of the Ducati Rim Mesh.....	40
Figure 30: Illustration of Fixed Support on the Ducati Rim	41
Figure 31: Remote Loading of the Ducati Rim	41
Figure 32: Longitudinal Strains: Outer Section - Ducati Rim	43
Figure 33: Longitudinal Strains: Inner Section - Ducati Rim	44
Figure 34: Transverse Strain: Outer Section - Ducati Rim	45
Figure 35: Transverse Strains: Inner Section- Ducati Rim	46
Figure 36: In Plane Shear Strain: Outer Section - Ducati Rim.....	46
Figure 37: In Plane Shear Strain: Inner Section - Ducati Rim	47
Figure 38 : Defining the Maximum Failure Criterion	50
Figure 39: IRF - Longitudinal Strain Mode: Outer Section - Ducati Rim	51
Figure 40: IRF - Longitudinal Strain Mode: Inner Section - Ducati Rim.....	51
Figure 41: IRF - Longitudinal Strain Mode: Inner Section - Ducati Rim.....	52
Figure 42: IRF - Transverse Strain Mode: Outer Section - Ducati Rim	52
Figure 43: IRF - Transverse Strain Mode: Inner Section - Ducati Rim	53
Figure 44: IRF - Transverse Strain Mode: Inner Section - Ducati Rim	53
Figure 45: IRF- In Plane Shear Strain Mode: Outer Section - Ducati Rim.....	54
Figure 46: Maximum Strain - In Plane Shear Strain Mode: Inner Section - Ducati Rim	54
Figure 47: IRF - In Plane Shear Strain Mode: Outer Section - Ducati Rim.....	55
Figure 48: Load Case of Passenger Vehicle Carbon Fibre Rim.....	57
Figure 49: Longitudinal Strains: Outer Section - Ducati Rim (2000 Nm)	58
Figure 50: Longitudinal Strains: Inner Section - Ducati Rim (2000 Nm)	58
Figure 51: Transverse Strains: Outer Section - Ducati Rim (2000 Nm).....	59
Figure 52: Transverse Strains: Inner Section - Ducati Rim (2000 Nm).....	59
Figure 53: In Plane Shear Strain: Outer Section - Ducati Rim (2000 Nm).....	60
Figure 54: In Plane Shear Strain: Inner Section - Ducati Rim (2000 Nm).....	60
Figure 55: IRF- Longitudinal Strain Mode: Outer Section - Ducati Rim (2000 Nm) ..	61
Figure 56: IRF - Longitudinal Strain Mode: Inner Section - Ducati Rim (2000 Nm) ..	62
Figure 57: IRF - Transverse Strain Mode: Outer Section - Ducati Rim (2000 Nm)...	62
Figure 58: IRF- Transverse Strain Mode: Inner Section - Ducati Rim (2000 Nm)	63
Figure 59: IRF - In Plane Shear Strain Mode: Outer Section - Ducati Rim (2000 Nm)	63

Figure 60: IRF - In Plane Shear Strain Mode: Inner Section - Ducati Rim (2000 Nm)	64
Figure 61: Passenger Car Carbon Fibre Rim Hub Segments	65
Figure 62: Thickness Variation: Passenger Car Rim	70
Figure 63: Thickness Variation: Outer Section- Passenger Car Rim	70
Figure 64: Refinement of the Passenger Car Mesh	71
Figure 65: Longitudinal Strain: Outer Section - Passenger Car Rim	73
Figure 66: Longitudinal Strain: Inner Section - Passenger Car Rim	73
Figure 67: Transverse Strain: Outer Section - Passenger Car Rim	74
Figure 68: Transverse Strain: Inner Section - Passenger Car Rim	74
Figure 69: In-Plane Shear Strain: Outer Section - Passenger Car Rim	75
Figure 70: In-Plane Strain: Inner Section - Passenger Car Rim	75
Figure 71: Maximum Strain Failure Criterion - Longitudinal Strain Mode: Outer Section - Passenger Rim	77
Figure 72: IRF - Longitudinal Strain Mode: Inner Section - Passenger Rim	78
Figure 73: IRF - Longitudinal Strain Mode: Inner Section - Passenger Rim	78
Figure 74: IRF - Transverse Strain Mode: Outer Section - Passenger Rim	79
Figure 75: IRF - Transverse Strain Mode: Inner Section - Passenger Rim	79
Figure 76: IRF - Transverse Strain Mode: Inner Section - Passenger Rim	80
Figure 77: IRF - In Plane Shear Strain Mode: Outer Section - Passenger Rim	80
Figure 78: IRF - In Plane Shear Strain Mode: Inner Section - Passenger Rim	81
Figure 79: IRF - In Plane Shear Strain Mode: Inner Section - Passenger Rim	81
Figure 80: Example of Strain Variation	84
Figure 81: Stress Illustration on Cube [edited 45]	95
Figure 82: Longitudinal Uniform Strain Loaded on RVE [edited 45]	96
Figure 83: Illustration of In-Plane Shear [edited 45]	98
Figure 84: Illustration of Intra-Lamina Shear [edited 45]	99
Figure 85: Residual Strength Curves of the Composites [edited-32]	100

List of Tables

Table 1: Voltage Results at Zero Load of the 1098 Ducati Rim [8].....	25
Table 2: Average Compression and Tensile Strain	26
Table 3: Properties of the Carbon Fibre Plies [34]	31
Table 4: Evaluation of Mesh Sizing	40
Table 5: Comparison of FEA and Experimental Strains	48
Table 6: Example of Bending Moment Calculation for the Vehicle.....	56
Table 7: Stacking Sequence of the Passenger Car Carbon Fibre Rim: Hub Section	66
Table 8: Stacking Sequence of the Passenger Car Carbon Fibre Rim: Spoke Section	67
Table 9: Stacking Sequence of the Passenger Car Carbon Fibre Rim: Rim Section	68
Table 10: Stacking Sequence of the Passenger Car Carbon Fibre Rim: Rim Re- inforcement	69
Table 11: Evaluation of Mesh Sizing (Passenger Car Rim).....	71
Table 12: Comparison of the FEA strain of Passenger Car and Ducati Rim	76
Table 13: Comparison of the Ducati (2000 Nm) and Passenger Rim Strains.....	76
Table 14: Comparison of the Ducati (2000 Nm) and Passenger Rim IRF	82
Table 15: Thickness Comparison of the Rims.....	86

List of Symbols

A	Total area (mm ²)
A_m	Matrix area (mm ²)
A_f	Fibre area (mm ²)
E_f	Fibre modulus (MPa)
E_1	Longitudinal modulus (MPa)
E_2	Transverse in-plane modulus (MPa)
E_3	Transverse out of plane modulus (MPa)
E_m	Matrix modulus (MPa)
F	Force (N)
F_r	Permissible static wheel load (N)
G_f	Fibre shear modulus (MPa)
G_m	Matrix shear modulus (MPa)
G_{13}	Shear modulus through the thickness (MPa)
G_{12}	In-plane shear modulus (MPa)
G_{23}	Shear modulus in the plane perpendicular to the fibre (MPa)
M	Moment (Nm)
M_{bmax}	Maximum bending moment (Nm)
N_f	Fatigue life
V_f	Fibre volume percentage (%)
V_m	Matrix volume percentage (%)
d	Offset (m), the distance between the hub and the rim centreline

m	Mass (kg)
r_{dyn}	Dynamic tyre radius of largest intended tyre (m)
r	Radius (mm)
ϵ_m	Matrix strain
ϵ_f	Fibre strain
ϵ_1	Longitudinal strain
ϵ_1^1	Strain in 1 ¹ direction
ϵ_2	Strain in 2-direction
ϵ_{12}	In plane strain
f	Wheel load increase factor
σ_f	Fibre stress (MPa)
σ_m	Matrix stress (MPa)
σ_1	Longitudinal stress (MPa)
σ_{12}	In plane stress
σ_2	Transverse stress (MPa)
σ_1^t	Longitudinal tensile strength (MPa)
σ_1^c	Longitudinal compression strength (MPa)
σ_2^t	Transverse tensile strength (MPa)
σ_2^c	Transverse compressive strength (MPa)
τ_{12}	In plane shear (MPa)
ν_{12}	In-plane Poisson`s ratio
ν_f	Fibre Poisson`s ratio

ν_m	Matrix Poisson`s ratio
μ	Coefficient of friction
γ_{12}	Shear strain
θ	Strain gauge angle

Chapter 1: Introduction

1.1 Background

The wheel (rim) is a critical component in its form and function with respect to vehicle motion in the automotive industry [1]. The wheel is used in major forms of land transport (passenger vehicles, heavy industrial vehicles and motorcycles) and no one can dispute the importance of the wheel. The main function of the wheel is to transfer energy from the vehicle to the tyre [2]. The wheel assists in vehicle support, the comfort of the vehicle ride and torque transfer during braking and acceleration [2].

In the last decade, wheel manufacturers have focused on lightweight wheel designs. This was done by introducing new materials and manufacturing technologies, which are in line with the changing requirements in the automotive industry [3]. According to the above mentioned functions it is evident that the wheel is so important and ubiquitous, that designing an improved wheel from a new and more advanced material would have a major benefit on the transport industry. The major benefit for the transport industry will amount to fuel saving due to the high increase in fuel prices. The use of lighter materials with the required stiffness in vehicles will result in decreased fuel usage [4]. The main focus point of this research is to investigate the feasibility of a carbon fibre rim for a passenger vehicle.



Figure 1: 1098 Ducati BlackStone Tek Rims [5].

This research is a continuation of the investigation that evaluated the novel use of carbon fibre in designing an automotive car rim by Sali et al. [6]. The investigation looked at adapting the 1098 BST (BlackStone Tek) motorcycle rim (which is illustrated in Figure 1).

Grech-Cumbo [7] investigated the heating of the carbon fibre rim from the brakes of a car. A steel cylinder the same size as a brake disc was heated to 600 °C in a furnace and placed onto the hub of the BST 1098 motorcycle rim to simulate the heating of the rim from the brakes. The carbon fibre showed some discolouration and further investigation suggested to understand and quantify the heating of the carbon fibre from the car's brake discs. Further work was required to ensure that the structural strength of the carbon fibre is not compromised by the heat from the brakes of the car.

Sali et al. [6] investigated the structural integrity of the rim required to pass the dynamic cornering fatigue test requirements (the wheel testing concepts will be discussed in further detail in section 1.3). The computational calculations showed that the BST 1098 rim would be strong enough to support the increased loads of a car by adding more layers of carbon to the spokes and by redesigning the aluminium hub. The FEA (finite element analysis) calculations were not validated with experimental results.

The focus of this research report is to investigate if carbon fibre rims are feasible for use on passenger cars. In 2010, Kienhöfer [8] performed the cornering fatigue test on the BlackStone Tek Ducati rim; to simulate the strains experienced during the test. The strain results will be utilised to validate the FEA model of the BlackStone Tek Ducati rim and investigate the feasibility of a carbon fibre passenger rim. The Ducati rim will be further discussed in the section below.

1.2 BlackStone Tek Ducati Rim

Wheel design has seen an evolution in material, from polymeric composites (wood) to metals (steel and aluminium), to carbon fibre as illustrated by BlackStone Tek (BST). BST is a South African company that designs, manufactures and tests composite motorcycle rims. BST is a ISO 9001:2008 certified company, and manufactures aftermarket rims that can be used in competitive motorcycle racing [5]. The rims are manufactured as one unit using the autoclave manufacturing process. This process assists in the manufacturing of the rim through regulation of the pressure and temperature in the envelope of the autoclave oven, which is essentially a pressure vessel [3]. Rim Technology, Eurotype Test Centre and German TÜV have tested the wheels and they have met all requirements with regards to road certification [5].

The 1098 Ducati rim (Figure 1) weighs 2.7 kg. The composite motorcycle rims reduce the mass and rotating moment of inertia, which significantly reduces the forces required to move or steer the motorcycle [5]. Therefore the lighter wheel improves handling, acceleration and deceleration, which can be attributed to the mass distribution in the wheel [5]. The composite rims also offer excellent aesthetic appeal.

Figure 2 illustrates the components of the BST Ducati rim. These components assist in the basic functionality of the rim (wheel) and the fitment of the tyre to the rim section. The wheel loads are dependent on the vehicle characteristics (tyre pressure; weight; suspension system etc.) and service conditions [9].

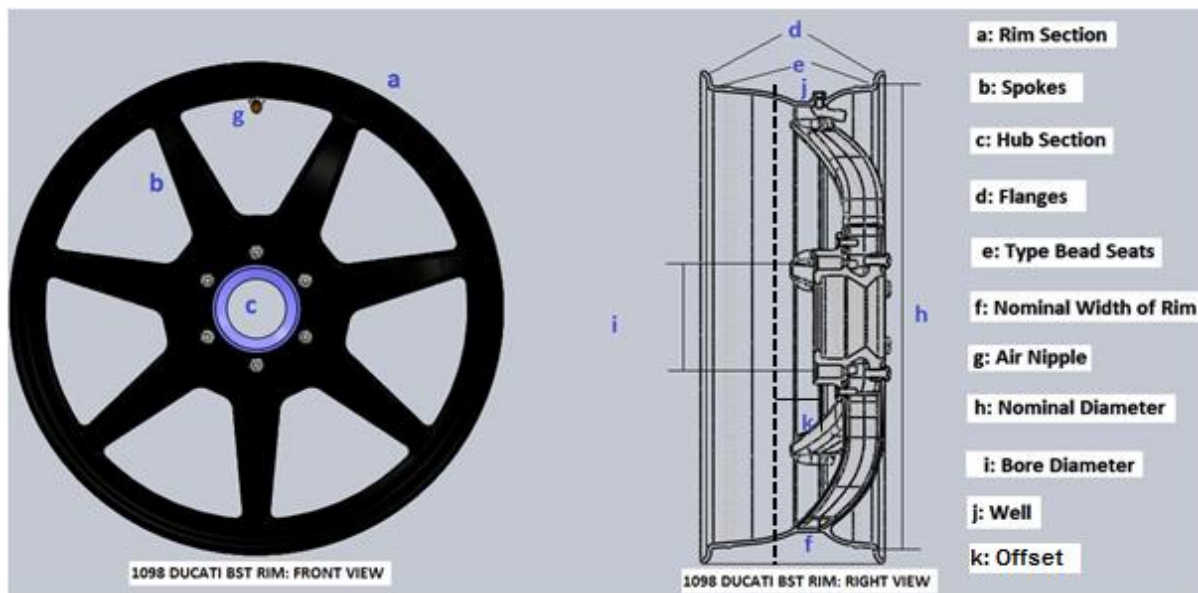


Figure 2: Anatomy of the BST Ducati Rim

The wheel's main components are:

- ❖ **Hub:** the attachment point between the wheel and the vehicle. This section consists of bolt holes along the bore diameter to facilitate in the fastening of the wheel to the vehicle [2].
- ❖ **Rim:** the interface between the wheel and tyre, that assists in tyre fitment [2].
- ❖ **Spokes:** the structural members that transfer the loads from the hub to the rim.

The 1098 Ducati BST rim as indicated in Figure 2, will be the reference design for the development of the carbon fibre passenger vehicle rim. The BST motorcycle rim is used as a benchmark design, due to the moulds being expensive (approximately R250 000 each). The same motor cycle rim moulds will be used to manufacture the carbon fibre passenger vehicle rims, once the structural integrity checks have been done. If the integrity checks give a positive result; then the secondary problem of the heating of the carbon fibre can be evaluated and possible solutions developed. The wheel testing specification will be discussed in the section 1.3.

1.3 Wheel Test Methods

The structural integrity of the wheel can be evaluated using the test methods outlined in Figure 3. The tests evaluate the accelerated fatigue life of the wheel. Wheels that are intended for passenger use must pass an impact test, cornering fatigue test and radial fatigue test before they go into production [3].

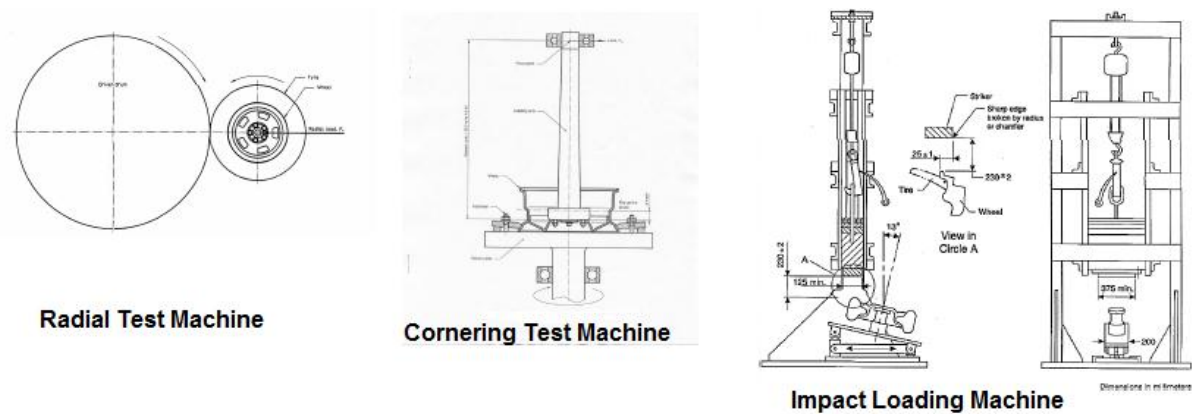


Figure 3: Wheel Test Methods [10; 11]

- ❖ **Radial Fatigue Test:** A wheel with a tyre is loaded against a rotating drum to simulate straight ahead driving conditions [10]. Accelerated loads are applied to evaluate stresses into the tyre and rim [10].
- ❖ **Cornering Fatigue Test:** The cornering fatigue test entails constraining the rim flange while a force is applied to the hub through a load arm [12]. The test simulates cornering driving conditions.
- ❖ **Impact Test:** The rim flange of a wheel and tyre assembly is impact loaded [11]. The assembly is mounted at a 13 degree angle to the horizontal plane, before the load is applied. This test simulates the loading experienced when a vehicle drives over a pavement or experiences a sudden impact.

The failure criterion for each of the tests is considered to be any permanent deformation of the wheel or wheel assembly (tyre and wheel). This ranges from crack initiation or loss of tyre pressure due to wheel deformation depending on the test in question. The carbon fibre rim will be structurally validated through the cornering fatigue test with reference to the Society of Automotive Engineers (SAE)

Handbook J328 [13] as illustrated in Figure 3. Karandikar et al. [14], Raju et al. [3], Guo et al. [15], Fischer et al. [16], Kocabicak et al. [17], Riesner et al. [18] and Wang et al. [19] [12] have compiled research papers outlining the simulation of the dynamic cornering fatigue tests of metal (steel and aluminium) automotive wheels. The papers outlined above overlook the dynamic cornering fatigue test (CFT) of carbon fibre rims, as they are intended for metallic rims, but are relevant with regards to carbon fibre rims. The CFT has the highest failure rate amongst the three tests [3]. Therefore the CFT is the relevant test with regards to the research investigation.

1.4 Problem Description

The automotive industry is a crucial industry of the economy. The retail sales of automotive fuel in 2009 formed 29% of the income of R365 906 million of the motor trade industry in South Africa [20]. Retail sales of motor vehicle and sales of new motor vehicle parts and accessories are 49% and 9% respectively as indicated by Statistics South Africa [20]. It is evident that wheels (rims) play a crucial role in everyday life, due to the size of the motor trade industry, which contributes 6% to the GDP of South Africa [14]. The industry is a significant size, but carbon fibre rims for passenger cars have a non-existent share of the market. Steel and aluminium rims currently dominate the market [14] and therefore the development of a carbon fibre passenger car rim (wheel) will stimulate additional market growth in the motor trade industry.

In the development of new material for wheels (rims), it is essential that fatigue testing be conducted on the wheels in order to validate the wheel's structural and material integrity. The material shift from the conventional steel to aluminium wheels in the late 90s was part and parcel of the research done to develop fatigue curve results for aluminium wheels [10]. Carbon fibre is an extremely strong and light material. Its use as a suitable material to manufacture passenger car rims will be investigated in this report.

1.5 The Proposal

BlackStone Tek in partnership with the University of the Witwatersrand will be evaluating the feasibility of using carbon fibre to manufacture a passenger car rim. The 1098 Ducati rim will be used as a reference design for the carbon fibre passenger car rim as discussed earlier. The 1098 Ducati rim CFT strain results obtained by Kienhöfer [8] will be the starting point of the research. An FEA model of the 1098 Ducati rim will be developed to simulate the experimental CFT conditions. A good correlation between the Ducati rim`s dynamic cornering fatigue experimental and FEA strain results will validate the finite element technique.

The finite element technique will be utilised to develop the passenger vehicle rim FEA model. The structural integrity will be evaluated on strains on the wheel. The wheel`s ability to pass the cornering fatigue test will determine the fatigue life and durability of the rim [18].

In the next section/chapter the literature, apparatus and tests required to design and structurally verify a wheel design will be covered. This will include experimental and finite element analysis.

Chapter 2: General Theory

Wheels have been in existence since the Sumerian civilization of Mesopotamia [21]. The wheel has evolved from wooden chariot wheels; to wire spoke wheels; and finally steel and aluminium wheels [10]. Initially the fatigue failure of wheels was not evaluated due the low speeds and short vehicle life spans [10]. Once the vehicles could travel greater distances and reach faster speeds, then fatigue analysis of wheels became a priority. Fatigue analysis requires an understanding of the form, function and material of the wheel.

The foundation of design is in line with “the form follows function” principle as stated by Louis Sullivan an American architect [22]. The form follows material principle is a build on to the form follows function principle and addresses material design with respect to products structural form [22].

Form follows function is influential when it comes to the technical aspects of rim design. These aspects can be attributed to the rim components (Figure 2); rim shape; mass distribution within the rim (wheel) sections; moment of inertia of rim and the load cases experienced during braking; cornering and acceleration.

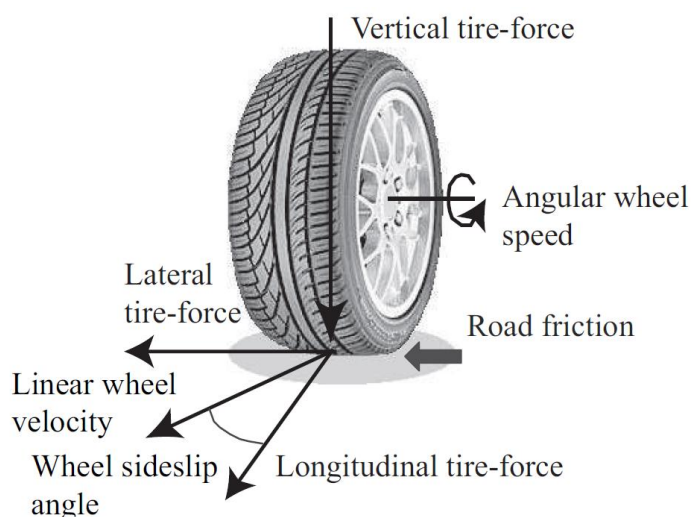


Figure 4: Wheel Dynamic Variables [23]

The dynamic load cases on the wheel are illustrated in Figure 4. The automobile weight is shared between the front and rear wheels. The weight distribution and suspension configuration on the vehicle will determine the load on each wheel. In

general the front wheels are used as the design reference point, in that they sustain greater load compared to the rear wheels. The wheel will experience lateral and longitudinal tyre force during cornering, braking, deceleration and acceleration through the tyre. The rim (wheel) should be able to handle these loads and maintain its structural integrity.

The material selection is in line with minimising the weight of the rim. The reduced density and volume properties of the material will determine the mass of the composite wheel.

The reduction in weight due to carbon fibre usage will improve the strength to weight ratio and minimise the moment of inertia [5]. The aim is to ensure that the centre of gravity coincides with the geometric centre of the wheel. Composite rim allows for the reduction in the overall weight in comparison to aluminium rims [5]. Therefore mass distribution and overall weight can reduce the moment of inertia and resistance to angular acceleration.

Form follows material is influential in material design with respect to composite rims. The general rule is that material should be used in the most efficient way, which allows for their properties and material malleability to benefit the product form and ultimately the function [22].

The structural integrity of the rim is dependent on the loading, manufacturing process, the mechanical properties and allowable stresses of the material [8]. Classical micromechanics as outlined in appendix A will assist in defining the properties of the composite material. The stiffness properties of the wheel are dependent on the material micromechanics. This fundamentally determines the rim's ability to resist deformation. The specification of CFT is outlined in section 2.1.

2.1 Design Standards for Wheels

Design standards of the wheels analyse the wheel fatigue strength by simulating load cases (radial and cornering loads) on a wheel during road usage [10]. The load cases are cyclic and encompass different load spectrums considering the load amplitude and frequency, which is dependent on the vehicle motion (braking, cornering, decelerating and accelerating) [24]. SAE (Society of Automotive

Engineers) J328 for passenger car and light truck steel wheels is the industry standard for fatigue test specification [10]. The SAE test specification has since evolved to take into account material changes and application changes in the wheels as illustrated in specifications such as SAE J1204 (trailer applications), SAE 328/J267 (temporary compact spares usage wheel) and SAE J1992 (military applications for take apart wheels) [10].

ISO 3006: 2005 (Road vehicles—Passenger car wheels for road use—Test methods) and ISO 3894:2005 (Road vehicles—Wheels/rims for commercial vehicles—Test methods) are based on SAE specifications [10]. The specification assisted in the development of material fatigue curves for wheels based on the material's condition and the type of loading under study. The results were later normalised to the ultimate fatigue life required from the wheel in service [10].

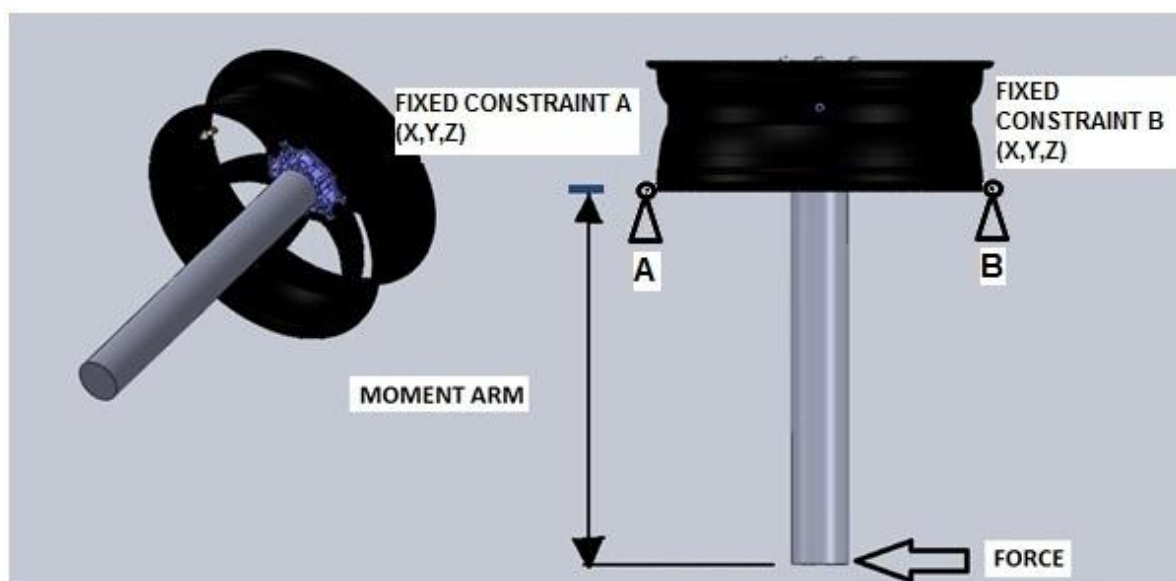


Figure 5: 1098 Ducati Rim Setup for Cornering Fatigue Test

The loading conditions that the rim will be exposed to during the cornering fatigue test are highlighted in Figure 5. The rim flange is constrained while a force is applied to the hub at a moment's arm through a rigid shaft, during the rotation of the rim [10]. During the test the rim is fitted with strain gauges in order to evaluate and quantify the strains. This is very important in product verification. In accordance with SAE specification the constant force needs to be applied at a minimum distance of 30 in

(762 mm) [10]. The deflection is measured at the loaded point on the shaft and the load is parallel to the plane through the centre of the rim as illustrated in Figure 5 [10]. In the detail rim design the dynamic cornering fatigue test is critical. The fatigue properties of the wheel (rim) is the ability of the rim to be subjected to a bending moment for 100000 cycles without displaying any evidence of harmful cracks, significant deformation or any abnormal looseness at joints [25]. This is applicable to specifications such as TÜV, ISO 3006:2005 and SAE Handbook J328.

Load formula

The maximum bending moment experienced by the rim during cornering fatigue test is expressed in equation 2.1 [10].

$$M_{bmax} = fF_r(\mu r_{dyn} + d) \dots \dots \dots \text{(Eq. 2.1)}$$

Where:

M_{bmax}	Maximum bending moment [Nm]
f	Wheel load increase factor is 1.5 which can be obtained by standards [17].
μ	Coefficient of friction between the tyre and the road. Drop centre rims ($\mu = 0, 7$) and bead seat rims ($\mu = 0, 65$) [26].
r_{dyn}	Dynamic tyre radius of largest intended tyre [m]
d	offset [m]. The distance between the hub and the rim centreline as illustrated in Figure 2.
F_r	Permissible static wheel load [N]

The assumption is that the passenger car total weight, consists of the passengers, vehicle and luggage load. The front wheels each support 30% of the total load and the rear wheels support 20% each. Therefore the front wheels are analysed as they experience the largest load. This is considered to be the permissible static wheel load. The CFT will be utilised to test the rim experimentally and through FEA. The

experimental analysis was done using strain gauges to obtain the longitudinal directional strains due to their versatility and precision of measurement [2]. The strain gauge results will be converted into longitudinal, transverse and in plane shear strain using the formulas in section 2.2.

2.2 Experimental Analysis of the Ducati Rim

The validity of the finite element technique will be dependent on the experimental strain results. The experimental testing will lay the foundation for all the FEA modelling to follow. The section 2.2 illustrates an overview of the stress-strain relationship and the principles of strain gauging. Classical micromechanics were the fundamental basis of this report as illustrated in appendix A.

2.2.1 Stress strain relationship of a lamina

A lamina is a single layer of carbon fibre. The lamina is assumed to be stress free, void free and perfectly bonded [28]. A laminate is a combination of two or more bonded laminae [27]. The strain stress relationship is based on the assumption listed below:

- ❖ The matrix, fibre and lamina is isotropic and linearly elastic [27]

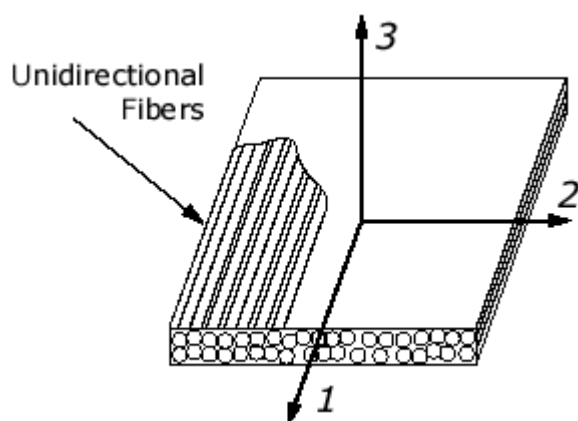


Figure 6: Unidirectional Fibres [28]

The strain stress relationship in the principal directions is illustrated in the matrix formula in equation 2.2 [27]. Hooke's law stress-strain relationship in a 1-2-3

orthogonal system forms a six by six matrix indicating 6 stresses, 6 strains and 6 displacements. Equation 2.2 is a simplified 3 by 3 matrix, because a lamina is a thin layer and can be modelled using a plane stress model. The two dimensional analysis or plane stresses will assist in analysing surface stresses and strains in two dimensions [2].

$$\begin{pmatrix} \varepsilon_1 \\ \varepsilon_2 \\ \gamma_{12} \end{pmatrix} = \begin{pmatrix} \frac{1}{E_1} & -\frac{\nu_{12}}{E_1} & 0 \\ -\frac{\nu_{21}}{E_2} & \frac{1}{E_2} & 0 \\ 0 & 0 & G_{12} \end{pmatrix} \begin{pmatrix} \sigma_1 \\ \sigma_2 \\ \sigma_{12} \end{pmatrix} \dots\dots\dots \text{(Eq. 2.2)}$$

The stiffness matrixes are symmetrically as illustrated in equation 2.2 [28].

$$\frac{\nu_{12}}{E_1} = \frac{\nu_{21}}{E_2} \dots\dots\dots \text{(Eq.2.3)}$$

Where:

- E_1 Longitudinal modulus (MPa)
- ε_1 Longitudinal strain
- σ_1 Longitudinal stress (MPa)
- E_2 Transverse modulus (MPa)
- σ_2 Transverse stress (MPa)
- ν_{12} In-plane Poisson`s ratio
- G_{12} In-plane shear modulus (MPa)
- γ_{12} Shear strain
- σ_{12} In plane stress (MPa)

The two dimensional analysis will assist in linking up to the strain data obtained in the experimental testing. The principles of strain gauging will be discussed in section 2.2.2.

2.2.2 Principles of strain gauging

Strains are related to a small change in electrical resistance within a Wheatstone bridge circuit as indicated in Figure 7 [2]. The individual strain gauges measure longitudinal strains. The individual strains are transformed from the 1-2 coordinates into the 1¹ coordinate using equations 2.4 [29]. The engineering shear strain (γ_{12}) is twice the tensor shear strain (ϵ_{12}).

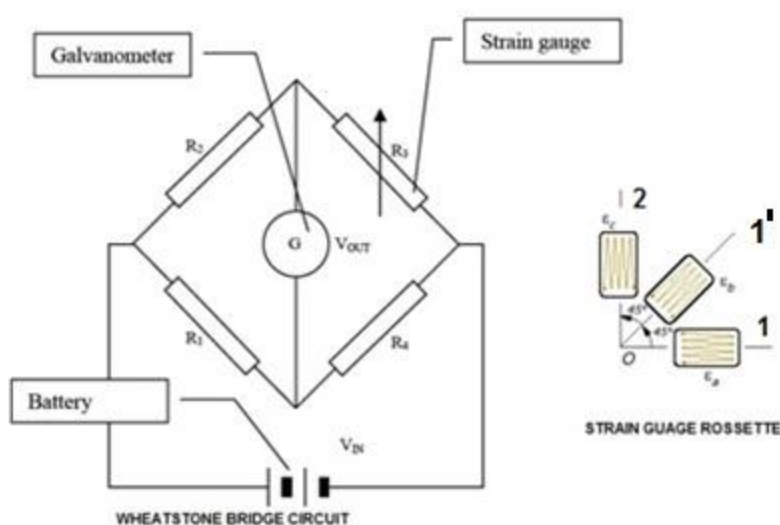


Figure 7: Strain Gauge Rosette [29] and Wheatstone bridge Circuit [2]

$$\epsilon_{1'} = \frac{\epsilon_1 + \epsilon_2}{2} + \frac{\epsilon_1 - \epsilon_2}{2} \cos \theta + \epsilon_{12} \sin \theta \dots \dots \dots \text{(Eq. 2.4)}$$

Where:

- $\epsilon_{1'}$ Longitudinal strain (1¹ – direction)
- ϵ_1 Strain in longitudinal-direction (1 – direction)
- ϵ_2 Strain in transverse-direction (2 – direction)
- ϵ_{12} In plane shear strain
- θ The angle between axis 1 and axis 1¹

The wheatstone bridge circuit and strain gauge were used to evaluate the surface strains of the Ducati rim. The experimental strain will be compared to the FEA strain. The literature review is highlighted in chapter 3, to evaluate relevant research in line with the subject matter.

Chapter 3: Literature Review

This section outlines the experimental analysis and numerical analysis of rims with respect to the cornering fatigue test. The detailed rim design entails understanding the loading conditions, material design and structural design. The design was validated through experimental and numerical methods.

3.1 Experimental Analysis

The SAE (Society of Automotive Engineers) J328 for passenger car and light truck steel wheels is the industry standard for fatigue test specification [10]. An excellent and a concise overview of the development of experimental fatigue tests for wheels was compiled by Kinstler [10]. One test method is the radial loading of a wheel assembly (tyre on the wheel), which is at a camber angle relative to the rotating drum [10]. This method is a build on to the straight driving radial testing, but in this case it was meant to simulate cornering driving conditions. The wheel assembly is loaded against the rotating drum using camber angles ranging from 5° to 30° [10]. This test proved to be difficult to execute; due to the low tyre life, which required frequent tyre changes to complete the test [10]. The test made it difficult to evaluate the wheel for cracks and deflection [10].

A second approach is to clamp the wheel assembly to a rotating table and apply a bending moment to the wheel (rim), through a shaft attached to the hub. Increased shaft deflection, fatigue cracking on the wheel and a decreased clamping force (loose clamps and nuts) is used as indication to terminate the test [10]. The method allows for easy and fast testing execution. The absence of the tyre allowed for higher test factors and cycles of wheel rotation, but these settings varied from each wheel manufacturer [10]. Therefore the SAE standardised the test equipment and procedure such as loading and cycles.

Muthuraj et al. [1] carried out experimental stress analysis on aluminium alloy wheels (original and modified design) using strain gauges to capture strains during the dynamic cornering fatigue test. Stresses were calculated through Hooke's law of

elasticity using the strains obtained through the strain gauges [1]. The elastic strain and isotropic Young's modulus in the wheel allows for the use of Hooke's law.

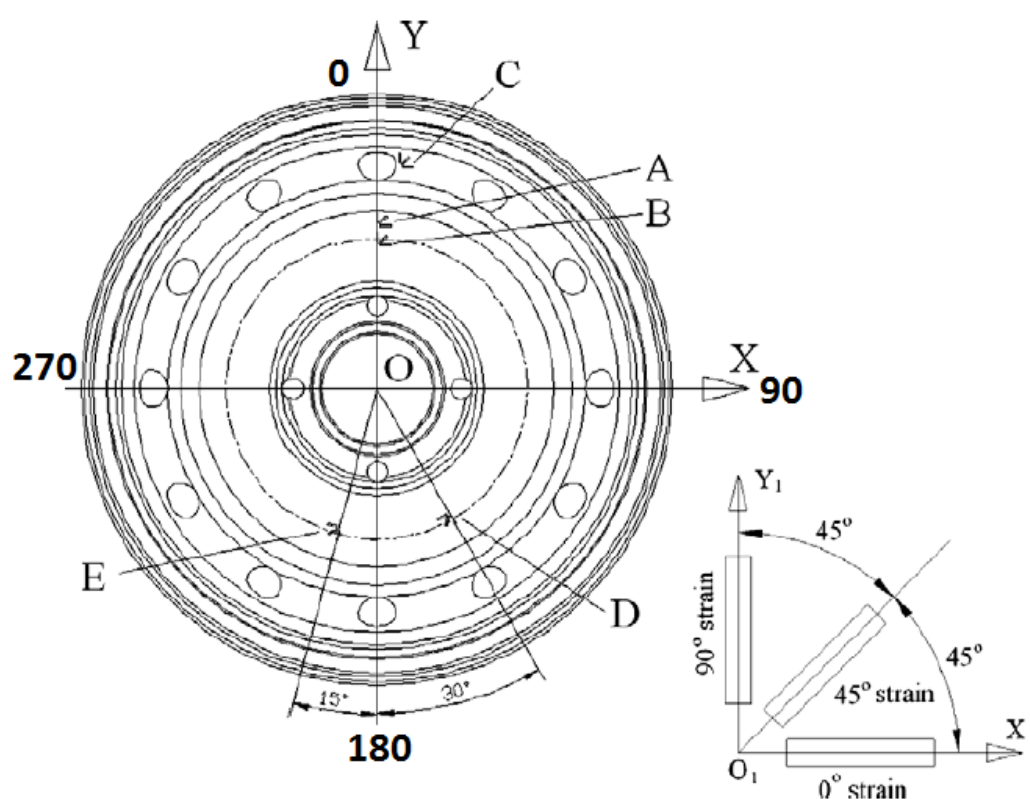


Figure 8: 45 Degree Rosettes Instrumented on the Wheel [edited 11]

Wang et al. [12] simulated the dynamic cornering fatigue test of a steel passenger car wheel [12]. The strain data are obtained from the instrumented wheel at points A, B, C, D and E as illustrated in Figure 8. The points are instrumented with 45 degree rosettes, which consist of three strain gauges orientated at 0, 45 and 90 degrees [12]. The strains on the wheel were measured at four positions (0, 90, 180 and 270 degree orientations) during the cornering fatigue simulation, where the force application was aligned with these positions as illustrated in Figure 8 [12].

The captured strains at the points were utilised to calculate the von Mises stresses [12]. The strain data illustrated the strain variation with the position of the wheel and the application of the force [12]. The data indicate a sinusoidal wave relationship between the strains obtained and the position of the wheel and force application. This relationship was expected as the largest strains are experienced only when the orientation of the strain gauges was in line with the force application path. The local

strain approach was used to predict fatigue failure of the wheel, using the stress strain curve. The experimental fatigue testing of metallic wheels is illustrated in this section, but relevance can be drawn with regards to carbon fibre rims. The Ducati rim was subjected to CFT conditions and instrumented with strain gauges to evaluate the longitudinal strains. The highlighted research papers evaluate the experimental data of metallic rims as intended; but research papers evaluating carbon fibre rims for passenger vehicles are limited. The numerical (FEA) analyses of wheels will be discussed in section 3.2.

3.2 Numerical Analysis

Karandikar et al. [14] developed FLIPS, which is a prototype computer based system that can predict the fatigue life of wheels. The FEA package is able to simulate the rotating bending moment fatigue test to obtain the lower bound on the fatigue life and the critical areas of the wheel, which is based on the local strain approach [14].

Guo et al. [15] outlined the FEA procedure to evaluate the fatigue life of a cast aluminium wheel using the S-N approach for a constant reverse loading condition [15]. The wheel was fatigue tested with reference to SAE J328, to evaluate the effect the clamp loads inclusion and exclusion have with regards to fatigue life predictions. The research illustrated that to accurately evaluate fatigue life prediction close to bolt locations, it was essential to include the mean stress changes induced by the clamping force [15].

Fischer et al. [16] evaluated the critical parameters to design a durable light-weight wheel (hub) design. The research indicated that the operational loading (straight driving and cornering stress) required to test the fatigue properties of the hub, which are dependent on the material and manufacturing process.

Hsu et al. [30] described the prediction of fatigue failures of aluminium disc wheels using the failure probability contour based on historical test data [30]. The historical data of dynamic cornering fatigue test were linked with simulation results to construct probability failure contours [30]. The finite element simulations captured the mean stress and stress amplitudes that were plotted on a two-dimensional plane [30]. Therefore for a new wheel, the failure probability of dynamic cornering fatigue test can be read directly from this probability contour [30].

Kocabicak et al. [17] performed a wheel numerical analysis using the bi-axial load-notch strain approximation for proportional loading [17]. The method estimated the fatigue life of a passenger car wheel during the cornering fatigue test under plane stress conditions [17]. The total deformation theory of plasticity evaluated the elasto-plastic strain of the component and the Palgren-Miner rule was the applicable damage accumulation method [17].

Wang et al. [19] proposed a fatigue failure life prediction method of aluminium wheels that integrates finite element analysis and the nominal stress method [18]. A static load finite element model of the aluminium wheel simulated the rotary fatigue test to obtain the equivalent stresses [19]. The equivalent stress was calculated using the nominal stress method based on effects such as the mean load size, fatigue notch, surface finish and scatter factors [19]. The fatigue life of the aluminium wheel was predicted using the equivalent stress amplitude and aluminium alloy wheel S-N curve [19]. This method resulted in accurate correlation between the bench test and the finite element model.

Fleischhauer et al. [31] evaluated the non-linear simulation of a lightweight composite rim. The relevance will be drawn from the finite element modelling performed on the Formula Student Race vehicle wheel. The initial design entailed the optimisation of the isotropic rim geometry, through evaluation of main stresses and local stress maxima induced by the maximum side and vertical load [31]. The optimised geometry allowed for evaluation of main stress plots, which allowed for optimisation of the fibre orientation and laminate structure [31]. A FEA model with layered shell elements was developed from the optimised geometry. The layered FE model is parameterised according to constant component thickness and constant layer structures [30]. The prepregs used in the build-up of the rim are unidirectional HT carbon fibre and woven fabric prepreg. The high precision Schürmann/Puck criterion was used in the analysis of fibre failure and inter-fibre failure [31]. The criterion indicates layers exposed to high magnitude loads, which could lead to fibre failures [31]. The highly stressed region is the transition between the spoke and rim bed and hub [31]. The numerical fatigue testing of metal and composite wheels is illustrated in this section, but research papers evaluating carbon fibre rims for passenger vehicles are limited. Previous work on composites is highlighted in section 3.3.

3.3 Previous Work on Composites

Composite material design assists in determining the limits of applicability of the material itself. This is work done with respect to the design, development and manufacture of composites [32]. Rim technology has evolved with material, due to the need for lighter rims. Giek et al. [33] examined and quantified fuel economy and energy incentives for the use of light-weight wheels on passenger cars [30]. The article evaluates the use of glass reinforcement plastic wheels and a laminated, form-filled wheel. Similar work has been done in improving the fundamental properties of line-based carbon fibre for transport applications by Compere et al. [4]. The research was done to evaluate the use of carbon fibre in automobiles in order to decrease fuel consumption and the overall weight of the vehicle.

Composites are being explored in the ultimate aim to replace steel and aluminium rims. Fatigue life prediction, experimental and FEA methods have assisted in the advancement of material selection with regards to rims. Fleischhauer et al. [31] evaluated the non-linear simulation of a lightweight composite rim. This paper evaluates a carbon fibre replacement rim for aluminium rim for a Formula Student racing car. The carbon fibre rim is validated through finite element analysis. BlackStone Tek has also done extensive development into composite motorcycle rims. The objectives of the research are highlighted in chapter 4.

Chapter 4: Objectives

4.1 Research Scope

The research report investigates the feasibility of a passenger car carbon fibre rim. The feasibility is to be validated through experimental and numerical cornering fatigue test data. In addition, the passenger car carbon fibre rim will be compared to its aluminium counterpart to quantify the weight saving.

Since the moulds required to manufacture the rim are expensive, the passenger car rim will be adapted to the 1098 Ducati rim mould for manufacturing purposes. The finite element model of the composite passenger car rim will be based on the correlation between the experimental and the FEA strain results of the 1098 Ducati BST rim, during the cornering fatigue test. The correlation accuracy between the two evaluation methods will be used to optimise the finite element analysis (FEA) of the carbon fibre passenger car. The investigation steps are outlined below:

1. Calculate the numerical strains, through the FEA modelling on the 1098 Ducati rim. This will be done by simulating the dynamic cornering fatigue test conditions experimentally tested by Kienhöfer [8] in order to validate the FEA modelling.
2. Investigate the correlation between the numerical and experimental results, to validate the FEA method. An accurate correlation will affirm the accuracy of assumptions, material inputs of the FEA modelling.
3. Design a carbon fibre rim for a passenger car using the 1098 Ducati rim as the reference design and the validated FEA model.

The research outline is illustrated in section 4.2.

4.2 Research Outline

Chapter 5: In 2010, Kienhöfer [8] performed the cornering fatigue test on the BlackStone Tek Ducati rim; to simulate the strains experienced during the test. This chapter will review the experimental results. Equipment such as National Instruments SCXI-1000 chassis, SCXI-1600 control card, SCXI-1520 universal card, SCXI-1314 module and strain gauges were used [8].

Chapter 6: The 1098 Ducati rim was evaluated using ANSYS. The model was created using accurate carbon fibre layups of the rim. The strain results of the FEA were correlated to the strain gauge results obtained experimentally.

Chapter 7: Design a carbon fibre rim to fit an automobile rim using the same 1098 Ducati mould and the validated rim FEA results from chapter six. The rim was adjusted to handle higher loads and moments that would have been experienced in the automobile. The rim design was validated through ANSYS.

Chapter 8: This chapter outlines the discussion, conclusions and the recommendations.

Chapter 5: Experimental Analysis: 1098 Ducati Rim

The experiment was conducted in 2010 by Kienhöfer at BlackStone Tek. The experiment results are referenced from the strain gauge results of the 1098 Ducati rim compiled by Kienhöfer [8]. The strain gauging by Kienhöfer was performed using four channels, single 120 Ohm gauge in a quarter-bridge as illustrated in Figure 9. The gauges were placed 80 mm from the inner circumference of the hub on the respective spokes. The gauges were placed on the front face and the back face of the respective spokes. One gauge was placed at 0 degrees (aligned to fiber direction along spokes) and the other at 45 degrees (45 degrees to fiber direction along spokes) [8]. The gauges were connected to an amplifier for data acquisition.



Figure 9: Strain Gauged Ducati Rim and Experimental Setup [edited 8]

The Ducati rim was subjected to CFT conditions highlighted in section 2.1. The German TÜV test specification requires a bending moment of 540 Nm to be applied [5]. The rim was subjected to a bending moment of 700 Nm, which is higher than the specification. Six static zero load readings were taken for each strain channel in Kienhöfer's experiment, three before testing and three after to verify that the reading did not drift. The readings were taken at a sample rate of 4000 Hz using a low pass

filter of 1000 Hz. The results of Kienhöfer's investigation illustrate a sinusoidal relation between the strain and the time (s) in Figure 10. Table 1 illustrate the voltage results at zero loads during testing. The gauges were extremely stable and the zero did not wander significantly [8].

Table 1: Voltage Results at Zero Load of the 1098 Ducati Rim [8]

	Channel 0 Front 0	Channel 1 Front 45	Channel 2 Back 0	Channel 3 Back 45
Static 1	0.0012 V	8.8578e-004 V	7.4628e-004 V	0.0012 V
Static 2	0.0012 V	8.8634e-004 V	7.6688e-004 V	0.0013 V
Static 3	0.0012 V	8.6590e-004 V	7.4182e-004 V	0.0013 V
Static 4	0.0012 V	8.7271e-004 V	7.4017e-004 V	0.0012 V
Static 5	0.0012 V	8.7280e-004 V	7.3760e-004 V	0.0013 V
Static 6	0.0012 V	8.7154e-004 V	7.2639e-004 V	0.0012 V

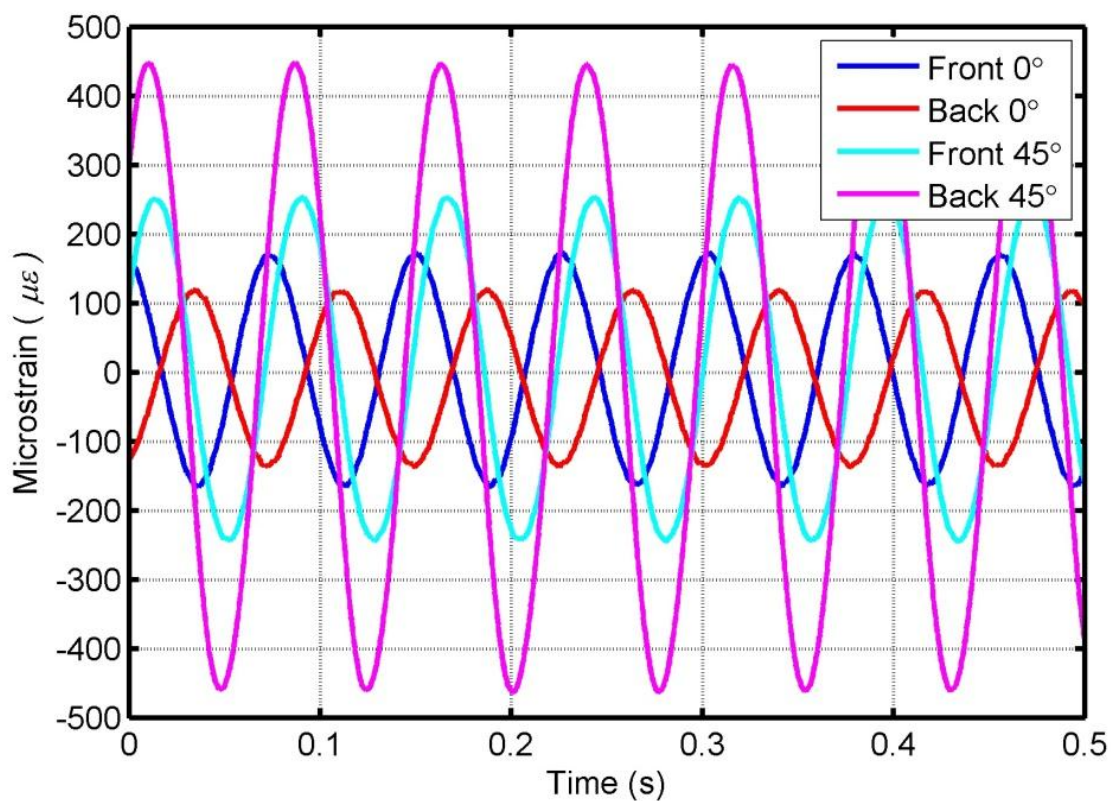


Figure 10: Strain Gauge Results of 1098 Ducati Rim during One Test Run [8]

Figure 10 illustrates that the strain gauges experience two peaks per revolution. The peaks illustrate compression and tensile phases during the rotation of the rim. The average tensile and compression strains are illustrated in Table 2.

Table 2: Average Compression and Tensile Strain

Strains	Channel 0 Front 0 ($\mu\epsilon$)	Channel 1 Front 45 ($\mu\epsilon$)	Channel 2 Back 0 ($\mu\epsilon$)	Channel 3 Back 45 ($\mu\epsilon$)
Average Tensile	173.8	254.2	120.4	448.9
Average Compression	-165.2	-245.8	-137.6	-465.1

A sinusoidal relationship was visible between the strain and time as the wheel was rotated. These findings were similar to the findings of Wang et al. [12], with respect to the strain, time and the rotation of the wheel. In an ideal situation, the longitudinal directional strains would be utilised to calculate the longitudinal, transverse, in plane shear strains equivalent strains. The absence of a third longitudinal strain on the front and back surface does limit the strain calculation (longitudinal, transverse and the in plane shear strains). Therefore the longitudinal directional strains were compared to the FEA longitudinal directional strains. The longitudinal, transverse and the in plane shear strains obtained in the FEA were utilised to calculate the longitudinal directional strains using equation 2.4. The FEA model of the Ducati rim is evaluated in chapter 6.

Chapter 6: FEA: 1098 Ducati Rim

This section aligns with the research report scope to investigate the numerical strains of the Ducati rim. The FEA model of the current 1098 Ducati BST rim simulated the cornering fatigue test. Please note that the experimental testing was done with the aluminium hub attached to the rim, but the FEA analysis will only be done with the rim. The detailed methodology followed during the FEA modelling is outlined in section 6.1. Section 6.2 outlines the results of the current 1098 Ducati rim. The sections are discussed in further detail below.

6.1 Methodology

The FEA methodology is outlined below, which entails model preparation, material design and the loading for the rim. These aspects are discussed in further detail below.

6.1.1 Model preparation

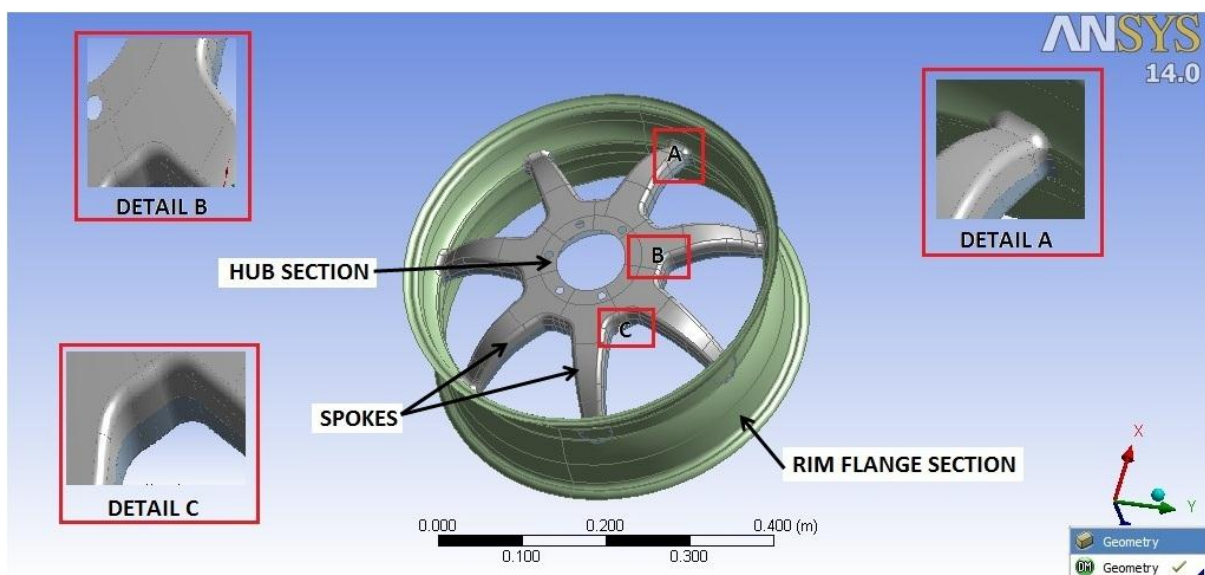


Figure 11: Surface Model of the 1098 Ducati Rim

The existing 1098 Ducati CAD model was imported into Solid Edge. The faces were deleted on the model in order to convert it into a surface model as illustrated in Figure 11. The conversion of the rim into a surface model allows for the definition of

the rim thickness, through material design in the FEA software platform. The material design was done by setting the material properties, stacking sequence and orientation of the plies. The rim was separated into three main components, which is the hub section, spokes and rim section. The transition between these components is crucial. It must be noted that the rim is manufactured in dies that are ultimately joined during the autoclave process as illustrated in Figure 12. The rim consists of an inner and outer section.

The transitions between the components are illustrated in detail A, B and C in Figure 11. These are the areas that require re-enforcement and the details are discussed below:

- Detail A illustrates the transition from the spokes to the rim flange (bed). Re-enforcement was required in this region to ensure proper dissipation of the forces into the rim section from the spokes.
- Detail B illustrates the transition from the hub to the spokes. Since the hub was highly stressed, it was essential to have re-enforcement in this area to ensure no fatigue failures occur. Stress concentrations around the attachment section (bolt holes) are expected.
- Detail C illustrates the transition from the inner spokes and outer spokes. Reinforcement in this area was essential in joining both sections of the rim; thereby ensuring the rim structural integrity.



Figure 12: Illustration of 1098 Ducati Rim Inner and Outer Sections

Therefore the understanding of this geometry and stress plots was essential before moving into the FEA (ANSYS) phase. Details A to C are illustrated in more detail in section 6.1.3.2. This section illustrates the segmentation of the Ducati rim. The surface model was an input into the ANSYS geometry section as illustrated in Figure 13.

6.1.2 Project schematic

The project schematic of the FEA analysis is illustrated in Figure 13. The process flow is outlined in the project schematic. Static Structural is interfaced with ACP (Ansys Composite Pre-Post) in order to clearly define composite properties. The functional blocks of the project schematic are outlined below:

- Geometry: The parasolid of the rim surface model was exported from Solid Edge as an input into this section. This section allows the user to define and evaluate if the CAD model was within the required FEA specification.
- ACP (pre): This interface was utilised in the material design when setting material properties, stacking sequence and orientation of the plies.

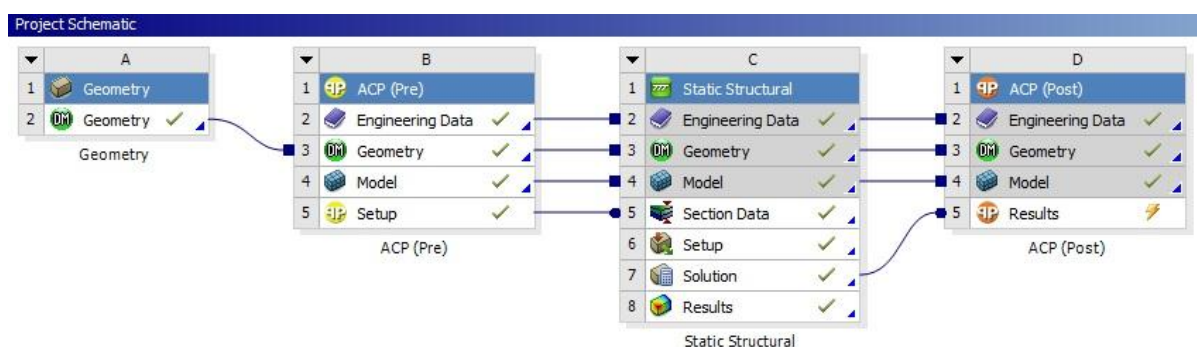


Figure 13: Project Schematic of the FEA Analysis

- Static structural: This interface was used in defining load cases, constraints and the solution generation. This was essential in setting static conditions of the cornering fatigue test.
- ACP (post): This Interface was utilised to evaluate the results, which in this case will be the evaluation of strains experienced by the 1098 Ducati Rim.

6.1.3 Material design

Material design was important to the structural integrity of the rim. The essential three factors in material (laminate) design of composites are:

- Material Properties: The macro/micromechanics and thickness of the material, which are defined in the engineering data.
- Segmentation: The rim was segmented into components that make up the rim. Material flows from segment to segment to form the entire rim as illustrated in section 6.1.3.3. These components are unique and have their own stacking sequence and ply orientation. Each component has a co-ordinate system, which was used in the stacking sequences.
- Stacking Sequence: The orientation and placement of the plies was dependent on the components co-ordinate system.

6.1.3.1 Material properties

The image shows two windows from the Engineering Data software. The top window, titled 'Outline of Schematic B2, C2, D2: Engineering Data', displays a tree view of material definitions. The bottom window, titled 'Properties of Outline Row 3: T300 Epoxy-Carbon, Woven, 230Gpa Prepeg', shows the detailed properties for the selected material.

Outline of Schematic B2, C2, D2: Engineering Data				
	A	B	C	D
1	Contents of Engineering Data		source	Description
2	Material			
3	T300 Epoxy-Carbon, Woven, 230Gpa Prepeg			
4	T700 Epoxy-Carbon, Undirectional, 230 Gpa Prepeg			
5	T700 Epoxy-Carbon, Woven, 230 Gpa Prepeg			
*	Click here to add a new material			

Properties of Outline Row 3: T300 Epoxy-Carbon, Woven, 230Gpa Prepeg					
	A	B	C	D	E
1	Property	Value	Unit		
2	Density	1.8	g cm ⁻³		
3	Orthotropic Secant Coefficient of Thermal Expansion				
9	Orthotropic Elasticity				
19	Orthotropic Stress Limits				
29	Orthotropic Strain Limits				
39	Ply Type				

Figure 14: Definition of Material Properties in Engineering Data

The material properties are defined in ACP (pre) engineering data as illustrated in Figure 14. The materials that are defined in engineering data are **T300** epoxy-

carbon, woven, 230 GPa Prepreg; **T700** epoxy-carbon, woven, 230 GPa Prepreg; and **T700** epoxy-carbon, unidirectional, 230 GPa Prepreg. T300 was used for aesthetics, but also plays a structural role in conjunction with T700 woven and unidirectional. The properties listed in Figure 14 were extracted from Hexcel Prepreg Technology and Torayca catalogue [34].

The properties of the respective materials are illustrated in Table 3. Unidirectional materials are stronger in the longitudinal direction and weaker in the transverse direction. Woven material is weaker than unidirectional material in the longitudinal directional. The material is weakened by the fibre twisting (bending) during the weaving process, but the woven material is stronger in the transverse direction in comparison to unidirectional material.

Table 3: Properties of the Carbon Fibre Plies [34]

	T300 Epoxy-Carbon, Woven, 230 GPa Prepreg	T700 Epoxy-Carbon, Unidirectional, 230 GPa Prepreg	T700 Epoxy-Carbon, Woven, 230 GPa Prepreg
Density (kg/m³)	1.8	1.8	1.8
E₁ (GPa)	70	170	90
E₂ (GPa)	70	10	90
G₁₂ (GPa)	10	5	10
v₁₂	0.1	0.3	0.1
Thickness	0.2	0.5	0.2

6.1.3.2 Segmentation

Segmentation of the rim was essential in the build-up of the 1098 Ducati rim. The rim was segmented using named selections. This allows for geometric definition of the parts on the rim. Part definition gives the user the freedom to define the co-ordinate system for each part as illustrated in Figure 19 and Figure 20. The main components of the rim are illustrated in Figure 15 and Figure 16. The main components are re-enforced with re-enforcement components illustrated in Figure 17 and Figure 18. The re-enforcement components assist in ensuring structural integrity in the transition zones as discussed in section 6.1.1.

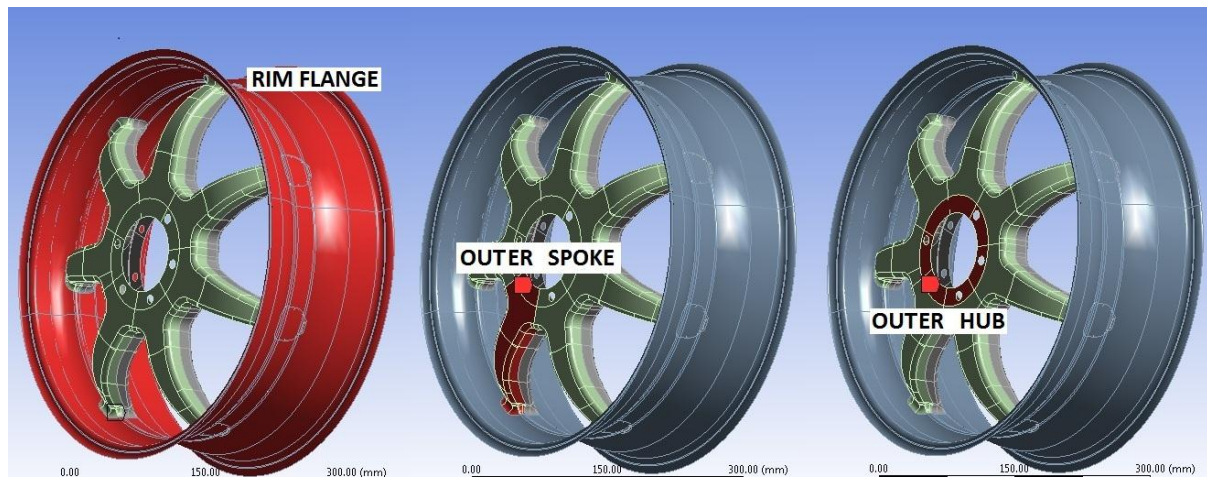


Figure 15: Rim Flange, Outer Spoke and Outer Hub of the 1098 Ducati Rim

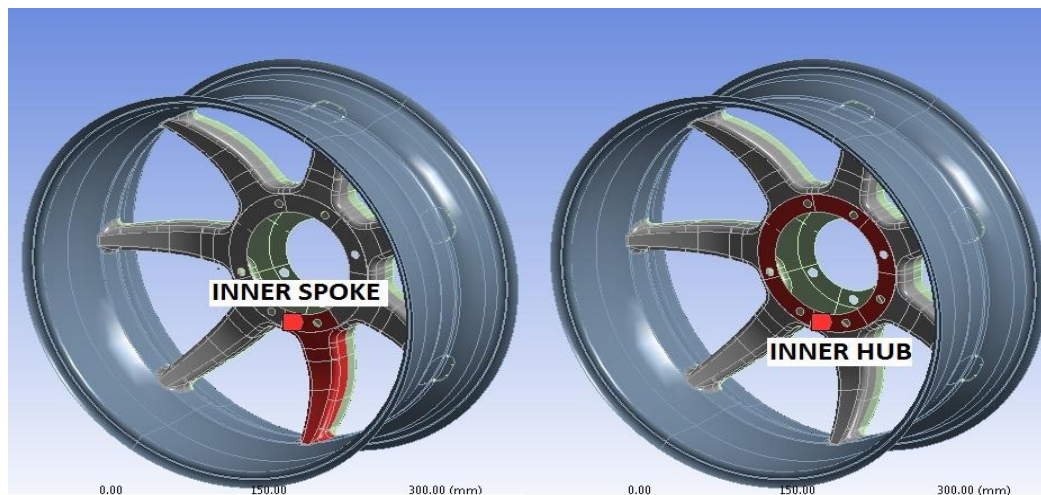


Figure 16: Inner Spoke and Inner Hub of the 1098 Ducati Rim

The main components are the inner spoke, inner hub, outer hub, outer spoke and rim flange section. The re-enforcement components are the rim flange cosmetic, spoke to spoke re-enforcement, inner spoke to outer spoke re-enforcement (intensifiers), outer spoke to rim re-enforcement and inner spoke to rim re-enforcement. The stacking sequence of all the above mentioned will be defined in section 6.1.3.3. The stacking sequence defined the properties of the main components and transition (re-enforcement) zones.

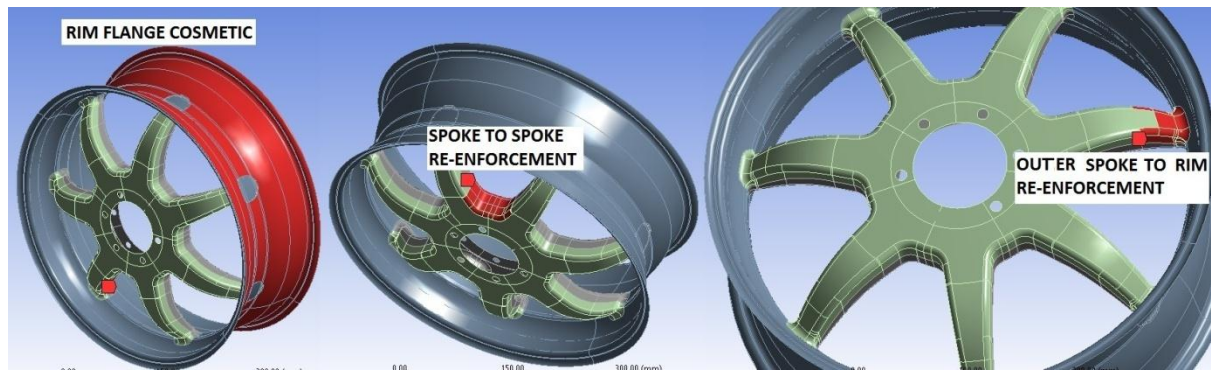


Figure 17: Rim Flange Cosmetic, Spoke to Spoke Re-enforcement, Outer Spoke to Rim Re-enforcement of the 1098 Ducati Rim

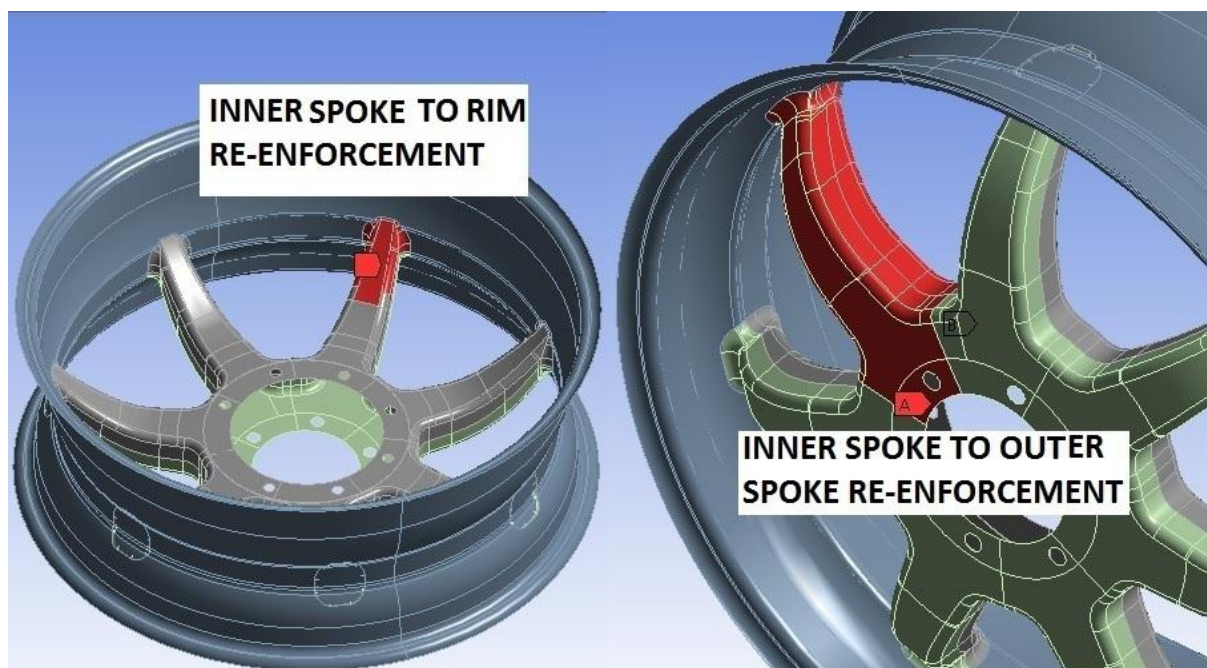


Figure 18: Inner Spoke to Rim Re-Enforcement and Inner Spoke to Outer Spoke Re-Enforcement

Each part has a co-ordinate system, which assists in setting the reference fibre direction as illustrated in Figure 24 . Co-ordinate system 01 was utilised for the rim flange and rim flange cosmetics. The co-ordinate system was a cylindrical co-ordinate system. Co-ordinate system 02 was utilised for the inner spokes, outer spokes, inner spoke to rim-enforcement, outer spoke to rim enforcement and inner spoke to outer spoke re-enforcement. The x-direction was along the length of the spoke to ensure the fibres, align with load paths. A similar co-ordinate system was duplicated along each spoke to match the orientation of each spoke.

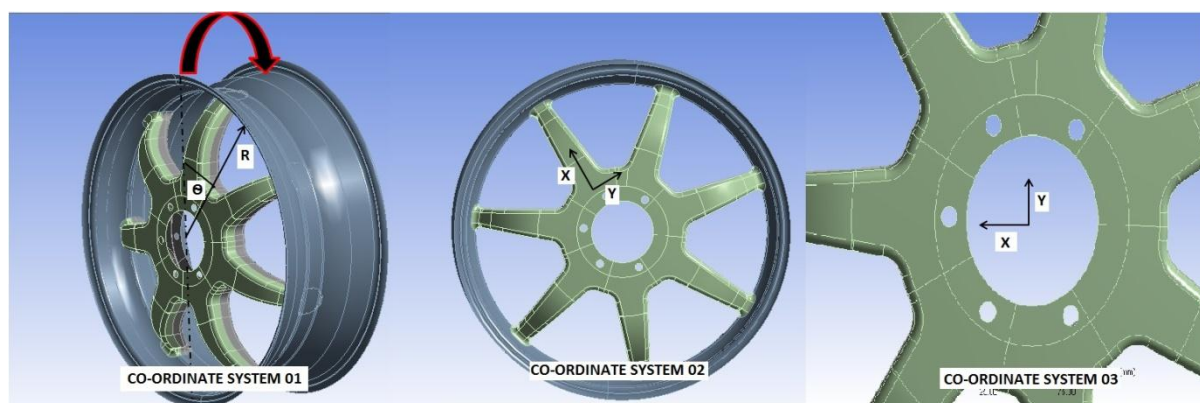


Figure 19: Example of Co-ordinate Systems of Components

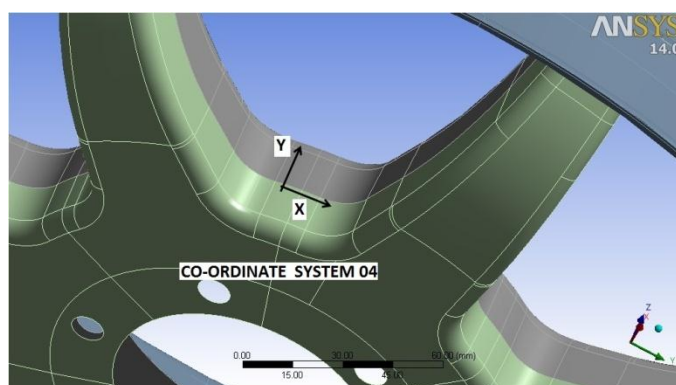


Figure 20: Example of Co-ordinate System for Spoke to Spoke Re-enforcements

Coordinate system 03 was used for the inner and outer hub. Coordinate system 04 was used for the spoke to spoke reinforcement. A similar co-ordinate system was duplicated along each re-enforcement to match the orientation of each. Therefore it was essential to have a co-ordinate system for each component (element set) as discussed. The co-ordinate system was defined using rosettes in the ACP setup which will be discussed in more detail in section 6.1.3.3. The components are formed through named selections, which essentially lead to the formation of element sets in the ACP setup. The stacking sequence of the components is outlined in section 6.1.3.3.

6.1.3.3 Stacking sequence

The stacking sequence was defined in the ACP Pre setup and this will be clarified in this section. The actual layup of the rim will not be dealt with so as to protect the proprietary knowledge of BlackStone Tek. The stacking sequence is illustrated in Figure 22 in the modelling ply groups. The stacking sequence of the main

components and re-enforcement are illustrated in Figure 22 in the order they are inserted into the layup. This is illustrated under the modelling ply groups. The orientation and number of plies will not be dealt with.

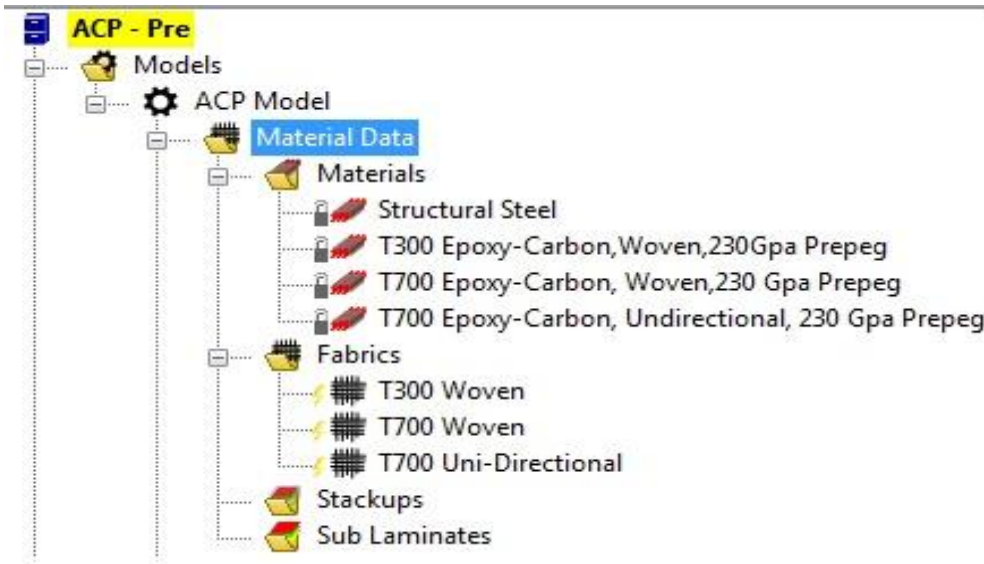


Figure 21: Material of 1098 Ducati Setup in ACP Pre Setup

The material properties are extracted from engineering data, which lead to the formation of fabrics. The fabric allows the user to enter the material thickness and they can be used in the formation of stack-ups and sub laminates as illustrated in Figure 21.

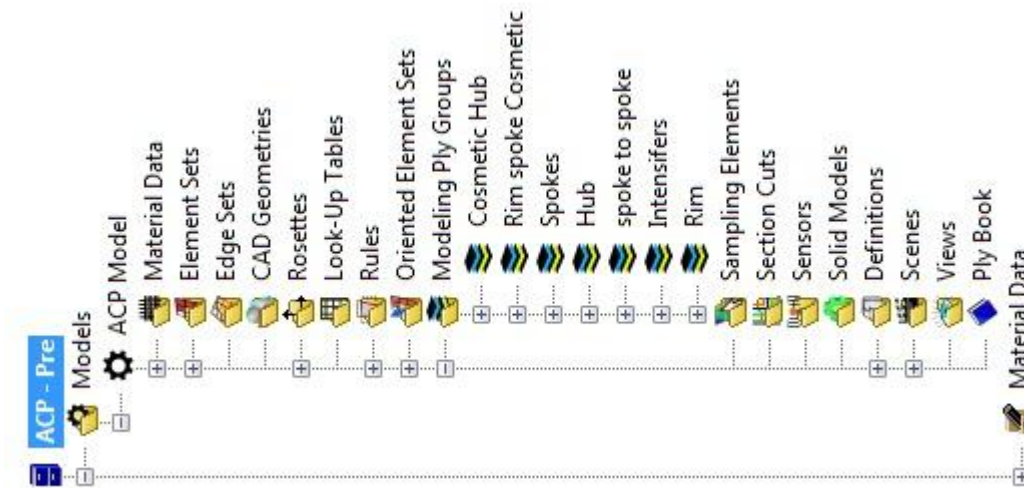


Figure 22: ACP Pre Process: Modelling Ply Groups

The named selections are illustrated as elements sets in ACP. This assists in defining the components as discussed in section 6.1.3.2. The co-ordinate systems for the components are defined using rosettes as illustrated in Figure 22 . The combination of the co-ordinate system and the element sets result in the formation of orientated element sets as illustrated in Figure 24. The yellow vectors indicate the reference fibre direction in the element sets. Orientated element sets were created for all the components using the relevant co-ordinate system in section 6.1.3.2. It was essential to ensure that the reference fibre directions for all the elements sets are correctly defined, for accurate structural characterisation.

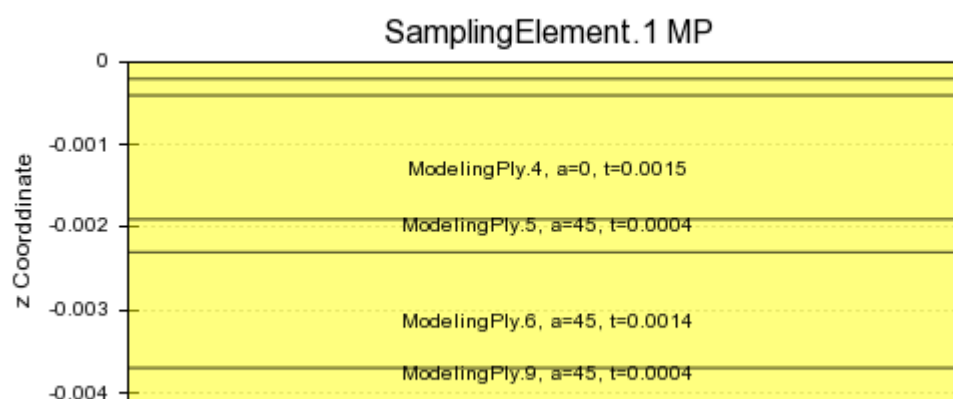


Figure 23: Sampling Element in the Hub Section

As an example, a sampling element was taken in the hub region as illustrated in Figure 23. The sampling element was utilised to view the stacking sequence in the hub region. The modelling ply is formed through a combination of material orientated in different directions. The a (Figure 23) illustrates the angle of orientation of the ply and the t (Figure 23) illustrates the ply thickness as illustrated in Figure 23.

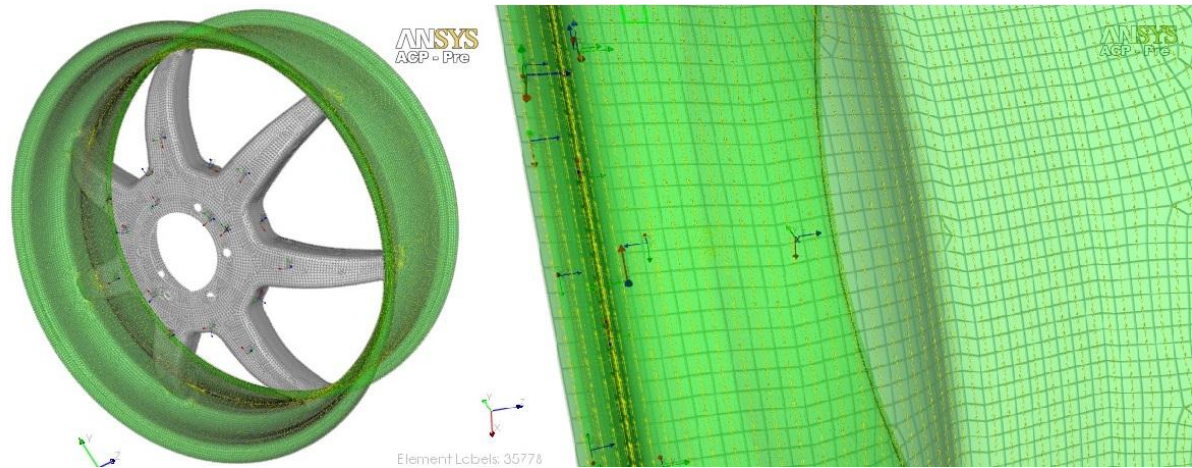


Figure 24: Illustration of Orientated Element Sets of Rim Flange

The orientated element sets stacking sequence was modelled using modelling ply groups, which allows the user to define the orientation and the quantity of stack-ups, sub laminates and fabrics as illustrated in Figure 25.

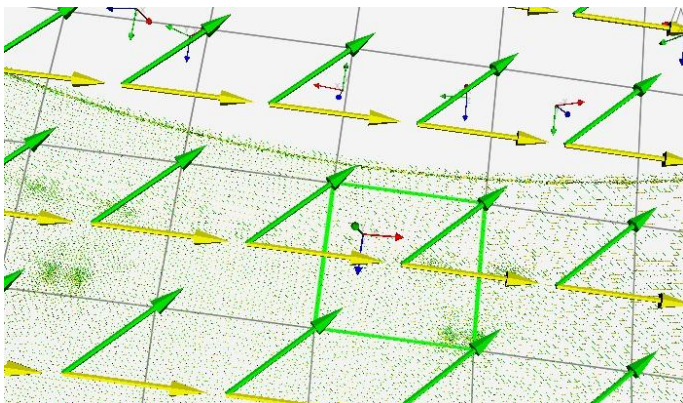


Figure 25: Illustration of Reference Fibre Direction (Yellow Arrow) and Fibre Direction (Green Arrow)

The ACP-Pre setup allows the user to define the stacking sequence in relation to BlackStone Tek 9004 Layup. The completed defined product was imported into the static structural section data. The stacking sequence gave the rim thickness and geometric characteristics as illustrated in Figure 26 and Figure 27 . The rim varies from a 4.1 mm hub, to 2.5 mm spokes and a rim section of 1.8 mm thickness (beads excluded). The imported layered section of the 1098 Ducati rim is illustrated in Figure 28.



Figure 26: Thickness Variation: Ducati Rim

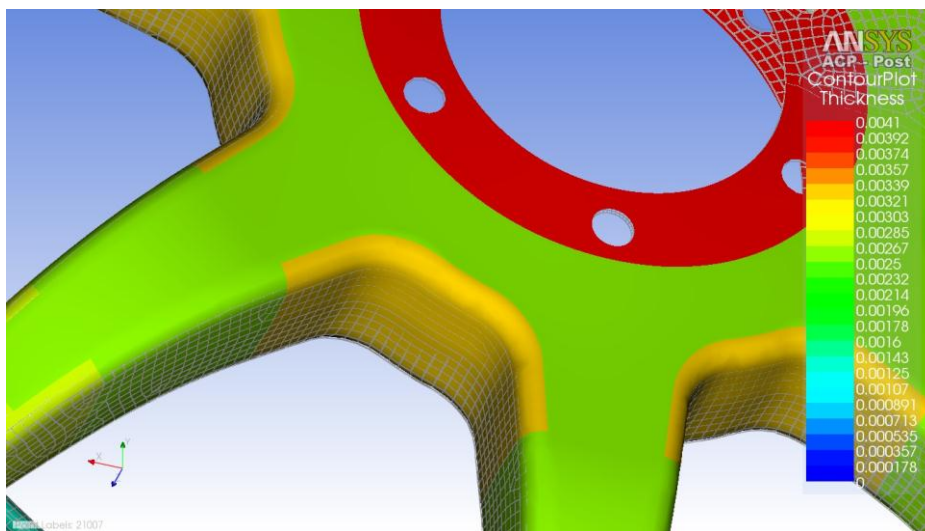


Figure 27: Thickness Variation: Outer Section-Ducati Rim

6.1.4 Meshing

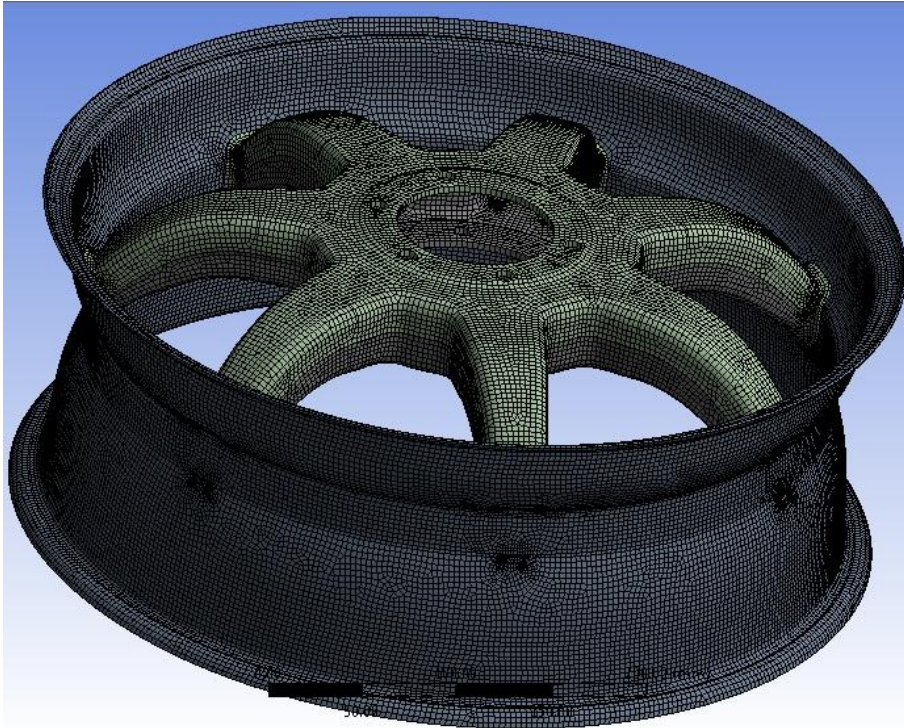


Figure 28: Meshed Imported Layered Section of 1098 Ducati Rim (Coarse Mesh)

Shell 181 elements were utilised in analysing the layers of the composite Ducati rim. The shell elements are suitable for analysing thin to moderately thick shell structures [35]. The element has 4 nodes with three translational and three rotational degrees of freedom [35]. The rim was meshed using the uniform quad element form. The use of this element in its triangular form is not recommended especially in high stress gradient areas [35]. The assumptions and restrictions of the shell 181 element in accordance to Ansys are outlined below:

- ❖ Zero thickness elements are prohibited [35].
- ❖ No slippage is assumed between the element layers [35]
- ❖ Zero through thickness stress [35]
- ❖ Shell 181 elements are well suited for linear, creep, elastic and hyper-elastic material properties [35].



Figure 29: Refinement of the Ducati Rim Mesh

The refinement of the mesh was crucial with respect to the accuracy of the results. The spoke in line with the force application was the interest point as illustrated in Figure 31. This spoke should experience the highest stress and strains. The mesh on the spoke as illustrated in Figure 29 was refined to a finer mesh in comparison to the rest of the rim geometry. The mesh sizing relevance centre and smoothing was set to medium and the minimum element size was 0.5795 mm. The mesh used 69091 nodes and 69069 elements. The refinement of the illustrated sections in Figure 29 is such that the mesh is two times smaller than the rest of the rim geometry mesh. The refinement of the mesh caused a small change in the results as illustrated in Table 4.

Table 4: Evaluation of Mesh Sizing

Strain	Medium Size Mesh	Refined Mesh	Difference
Longitudinal- 1Axis ($\mu\epsilon$)	929.18	929.57	0.04%
Transverse- 2 Axis ($\mu\epsilon$)	567.33	567.64	0.05%
In Plane Shear -12 Axis ($\mu\epsilon$)	-471.39	-471.61	0.05%

The discretization error and element size analysis was conducted on the refined spoke region as illustrated in Figure 29. A strain probe was placed in the vicinity to evaluate convergence of the results. The mesh was initially of medium size and later refined, in order to compare the two stages. The refinement of the mesh caused a small change in the results, thereby indicating that the sizing of the mesh is appropriate. This illustrates that the results have converged and further mesh

refinements would only prolong the analysis without any benefit. The load cases are illustrated in section 6.1.5.

6.1.5 Load cases

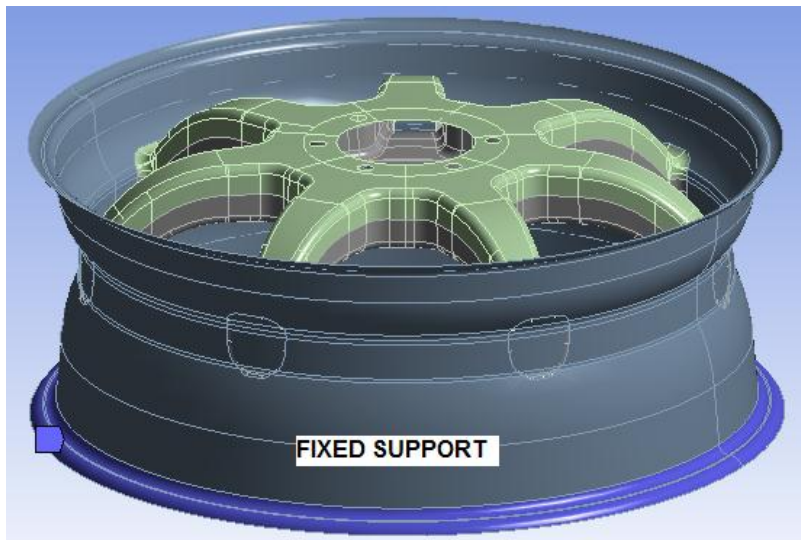


Figure 30: Illustration of Fixed Support on the Ducati Rim

The aim was to simulate the conditions the rim was exposed to during the experimental testing. This allowed for the comparison of the dynamic cornering fatigue experimental data with the static cornering fatigue FEA data. The static conditions of the cornering fatigue test are illustrated in Figure 30 and Figure 31. The rim was constrained on the rim flange as illustrated in Figure 30. The constrained area is highlighted in blue in Figure 30. A 700 N remote force was applied 1 m away from hub as illustrated in Figure 31. The force was attached to the bolt holes on the inner and outer hub.

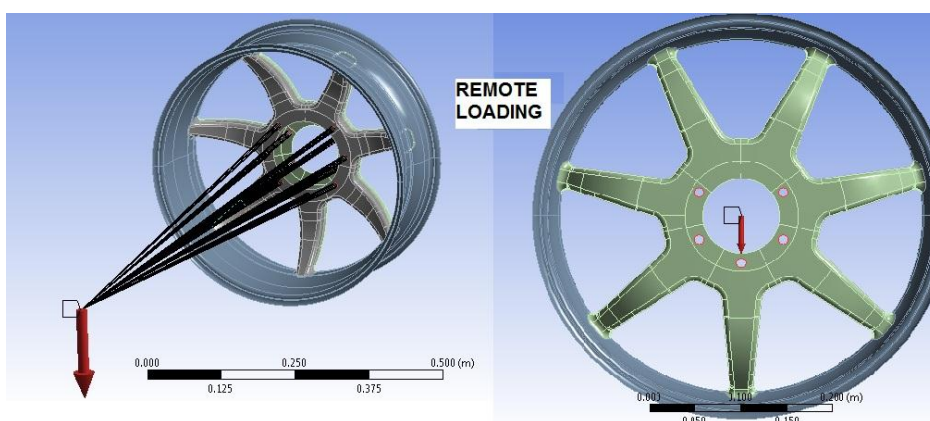


Figure 31: Remote Loading of the Ducati Rim

The load conditions assisted in obtaining the results and the FEA analysis of the Ducati rim are illustrated in section 6.2.

6.2 Result Evaluation: Current 1098 Ducati Rim

In this section the FEA results of the current Ducati rim are highlighted. The longitudinal, transverse and in-plane shear strain are highlighted. The maximum strain failure criterion was also evaluated. The main focus was on the strains experienced on the spokes. The general strain pattern was also evaluated. The results are presented below.

6.2.1 Strains

The strains from the hub are transmitted to the rim flange through the spokes. The strains on the curvature of the spokes illustrate that the spokes are load bearing sections. The strains around the spoke to rim flange transition illustrate that there is a load transition from the spoke to the rim. The strain flow patterns assisted in understanding the rim geometry and design. The following section evaluates the longitudinal, transverse and the in-plane strains experienced during the static analysis of the Ducati rim. The focus point was the spoke in line with the force application as illustrated in Figure 31. The interest point was the same as the strain gauge points during the experimental testing.

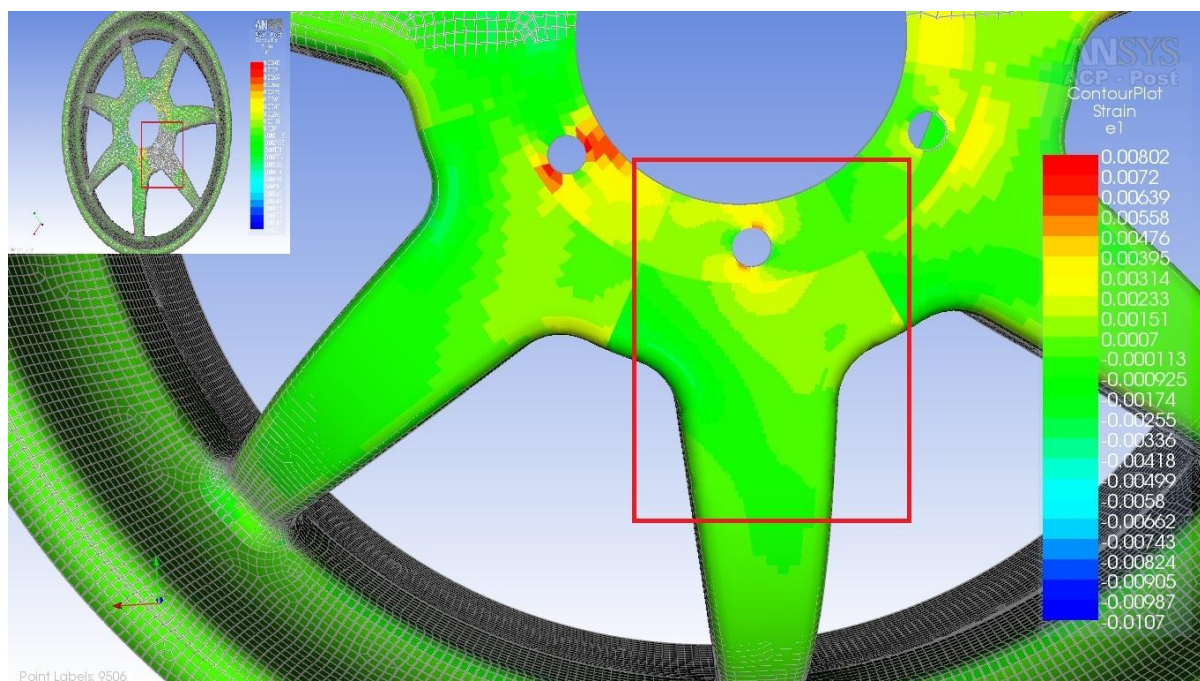


Figure 32: Longitudinal Strains: Outer Section - Ducati Rim

The points of interest were evaluated using sampling elements as highlighted in Figure 22 .The sampling elements assisted in zoning into the strain gauged zones. The general trend with respect to the longitudinal and transverse strains on the spoke is highlighted in Figure 32 to Figure 35. The outer section of the spoke was in tension, while the inner section was in compression. The strains are higher in the hub region at the bolt attachment holes in line with the force application. The strains in the hub region are expected to be high, due to the absence of the aluminium hub in the FEA analysis. The results in the hub region were overlooked as they are not modelled accurately. The hub results do not need to be accurate as the focus point is on the spoke. The reason the results in the spokes are still valid was that the overall constraints are still the same.

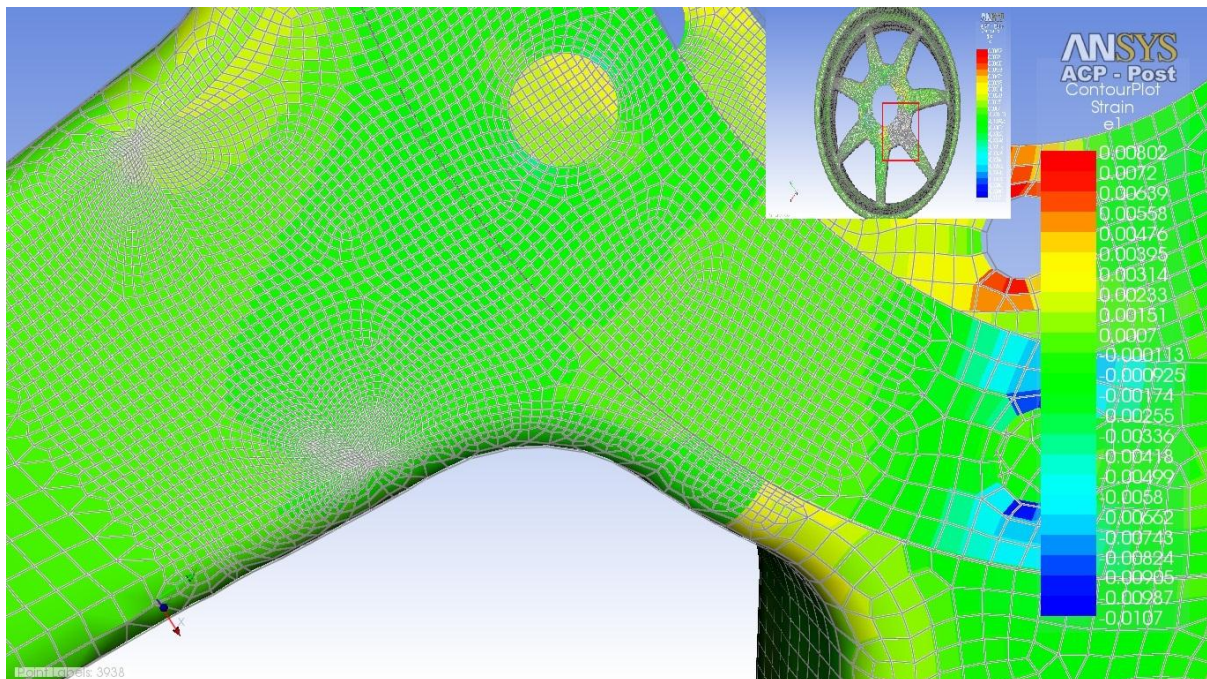


Figure 33: Longitudinal Strains: Inner Section - Ducati Rim

Figure 32 and Figure 33 illustrate the longitudinal strains on the Ducati rim. The longitudinal strains on the outer and inner spoke are $164 \mu\epsilon$ and $-113 \mu\epsilon$ respectively. This illustrates that the outer spoke experiences the largest strain in the fibre direction.

The transverse strain of the Ducati rim is illustrated in Figure 34 and Figure 35. The transverse strains of the outer and inner spoke are $-582 \mu\epsilon$ and $454 \mu\epsilon$ respectively. The transverse strains are smaller than the longitudinal strains. The in-plane shear strains of the Ducati rim are illustrated in Figure 36 and Figure 37. The in-plane shear strains for the outer and inner spoke are $328 \mu\epsilon$ and $-662 \mu\epsilon$ respectively. The strains obtained were used to calculate the longitudinal directional strains that can be compared to the experimental data. The strains were obtained using equation 2.4. The results are illustrated in Table 5.

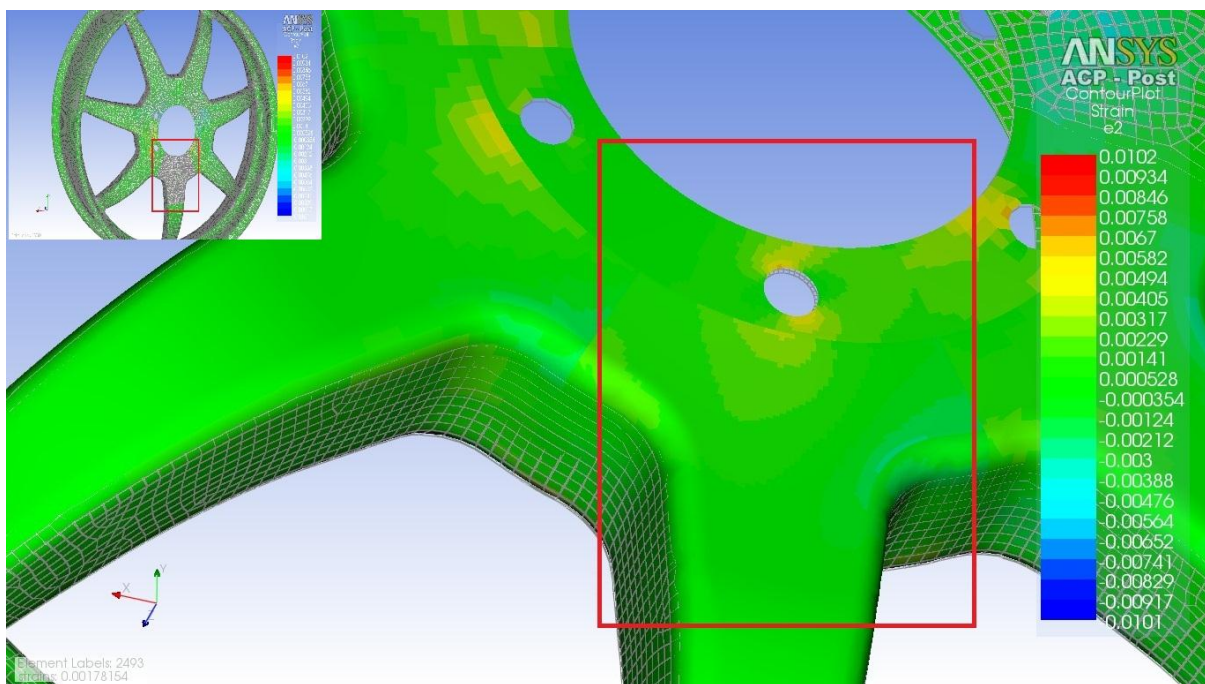


Figure 34: Transverse Strain: Outer Section - Ducati Rim

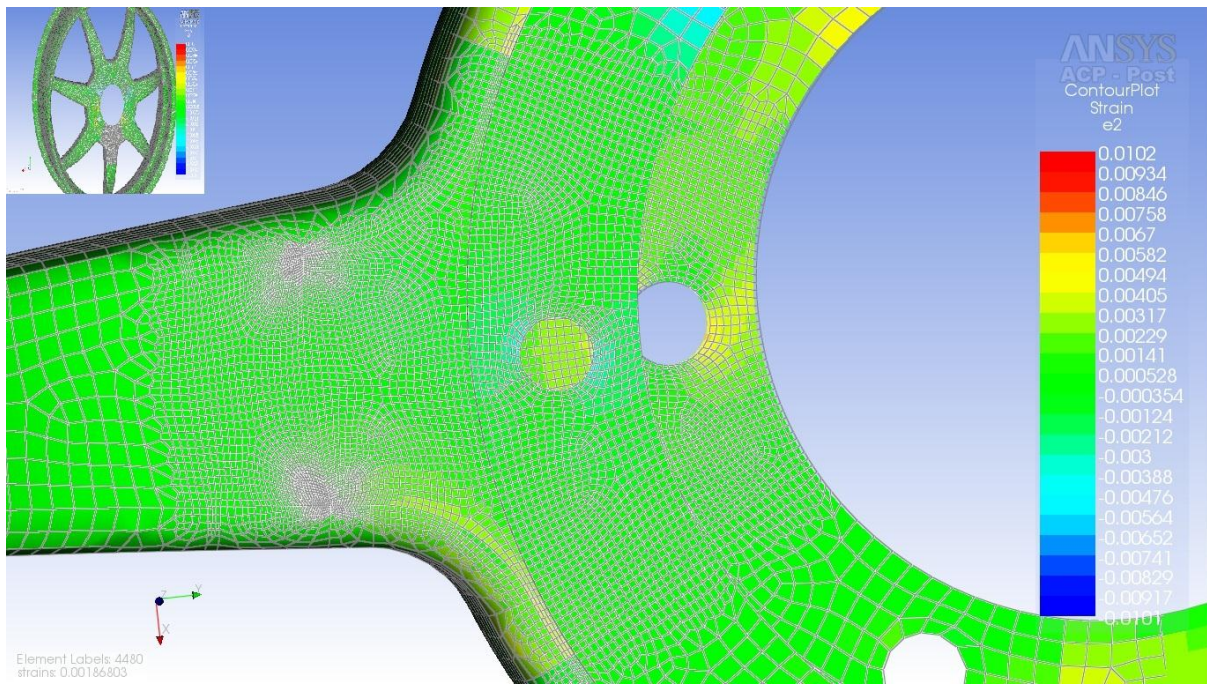


Figure 35: Transverse Strains: Inner Section- Ducati Rim

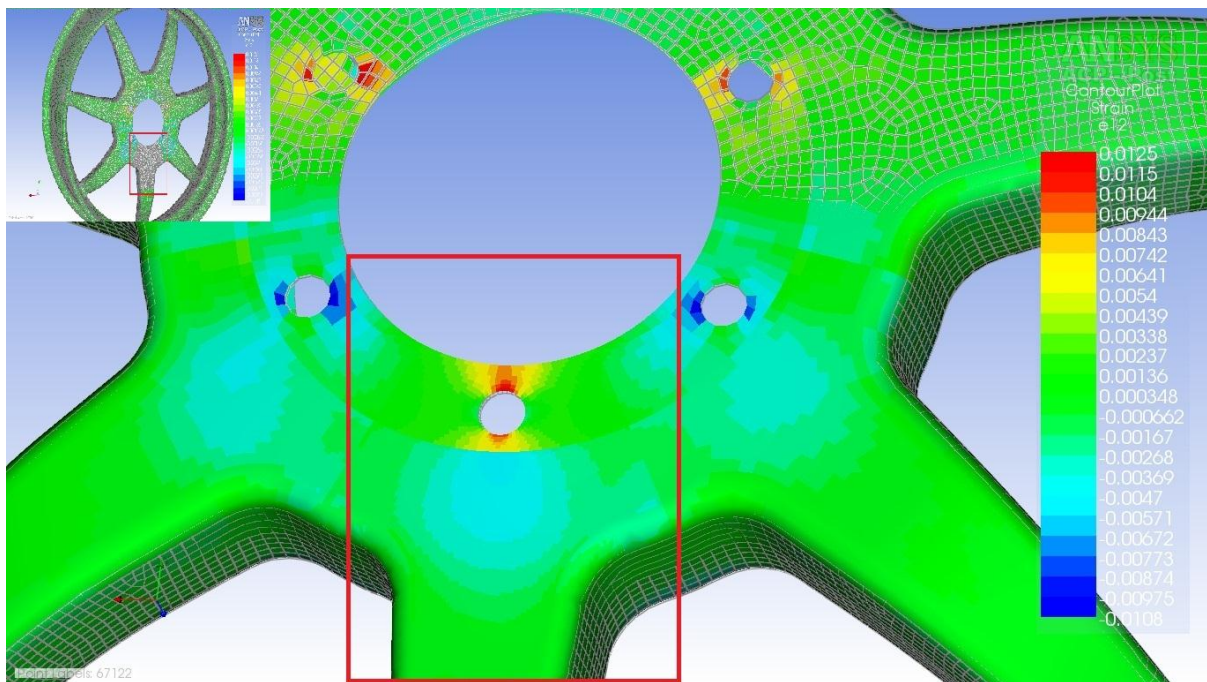


Figure 36: In Plane Shear Strain: Outer Section - Ducati Rim

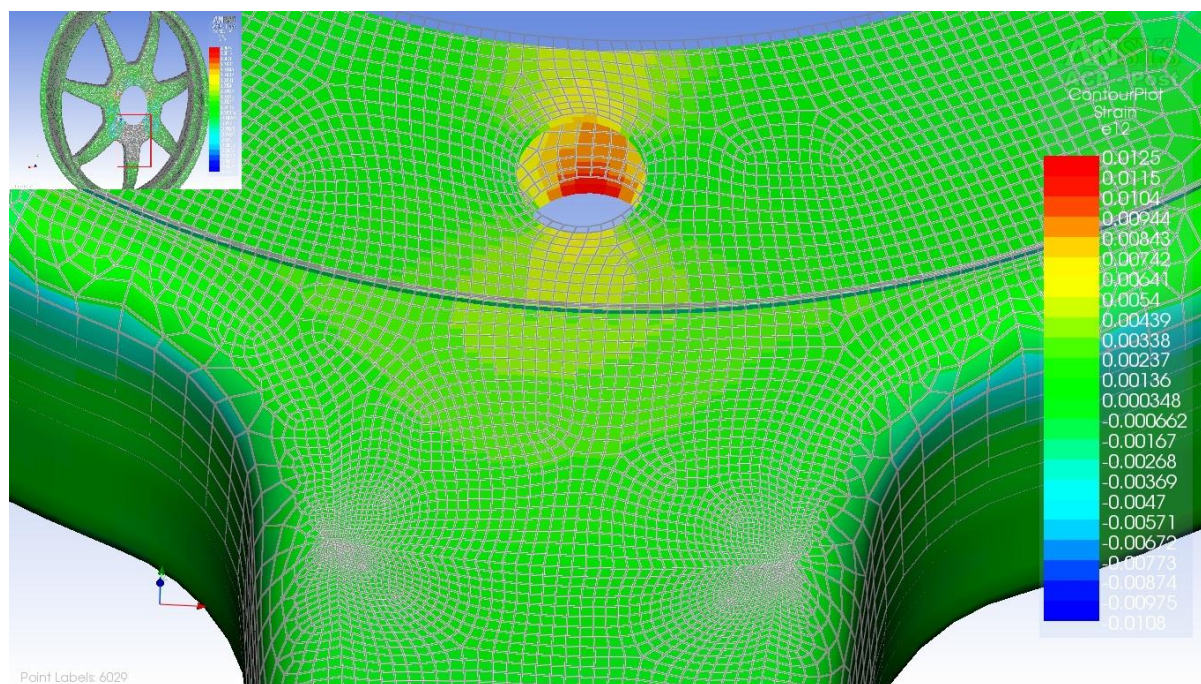


Figure 37: In Plane Shear Strain: Inner Section - Ducati Rim

The first step was to extract the relevant strain data (longitudinal, transverse and in-plane shear strain) from the FEA model. The outputs from the FEA model were utilised to calculate the longitudinal directional strains using eq. 2.4. The equation was utilised by setting a local coordinate system for the strains experienced on the inner and outer spoke. This was similar to the setup in Figure 7. The FEA results were utilised in step 3 to perform the comparison with the experimental results as illustrated in Table 5.

The FEA strains in the 45° - direction have an error of 6.64% and 13.78% for the inner spoke and the outer spoke respectively. The FEA strains in the 0° - direction have an error of -22.12% and -6.10% for the inner spoke and the outer spoke respectively. Therefore the results are within a 25% accuracy range, thereby indicating a reasonable correlation of the FEA and experimental data. Similar results were obtained in the research report by Smith, B. which evaluates a carbon fibre swingarm design [35]. The difference between the FEA and experimental results was mainly due to the modelling difficulty of the structure, with reference to ply overlay [35].

Table 5: Comparison of FEA and Experimental Strains

STEP 1	FEA INPUTS						
		Outer (Front) Spoke			Inner (Back) Spoke		
	ϵ_{1}	164 $\mu\epsilon$			-113 $\mu\epsilon$		
	ϵ_{2}	-582 $\mu\epsilon$			454 $\mu\epsilon$		
ϵ_{12}	328 $\mu\epsilon$			-662 $\mu\epsilon$			
STEP 2	STRAIN OUTPUTS (EQ. 2.4)						
		Outer (Front) Spoke			Inner (Back) Spoke		
	ϵ_{0}	164 $\mu\epsilon$			-113 $\mu\epsilon$		
	ϵ_{45}	295 $\mu\epsilon$			-489 $\mu\epsilon$		
STEP 3	CORRELATION OF RESULTS						
		Inner Spoke (FEA)	Inner Spoke (Exp)	Error (%)	Outer Spoke (FEA)	Outer Spoke (Exp)	Error (%)
	ϵ_{0}	-113 $\mu\epsilon$	-138 $\mu\epsilon$	-22.12%	164 $\mu\epsilon$	174 $\mu\epsilon$	-6.10%
	ϵ_{45}	-489 $\mu\epsilon$	-465 $\mu\epsilon$	6.64%	295 $\mu\epsilon$	254 $\mu\epsilon$	13.78%

6.2.2 Maximum strain: failure criterion

The maximum strain failure criterion in the ACP platform was used to predict whether fibre, matrix or in-plane shear failure will probably occur first [37]. The reserve factor (RF) is a measure of the margin of failure or factor of safety [37]. The equation of the reserve factor is indicated in equation 6.1. Therefore a RF, which is greater than one indicates a low probability of failure.

$$RF \times F_{applied} = F_f \dots\dots\dots (Eq. 6.1)$$

Where:

RF Reserve Factor

$F_{applied}$ Applied load

F_f Failure load

In this report the inverse reserve factor (IRF) or inverse factor of safety was used to evaluate the failure margin as illustrated in equation 6.2. This approach was more practical in that the non-failure values of the IRF range from zero to one and the failure values are above one [37].

$$IRF = \frac{1}{RF} \dots \dots \dots \text{(Eq. 6.2)}$$

The longitudinal, transverse and in-plane shear strains were analysed. In ACP the maximum failure criterion is a ratio between the actual strains to the failure strains that are compared in the ply principal coordinate system [37]. The maximum failure criterion is illustrated in equation 6.3.

$$f_{max} = \max\left(\left|W_1 \frac{\epsilon_1}{\epsilon_{1\ max}}\right|, \left|W_2 \frac{\epsilon_2}{\epsilon_{2\ max}}\right|, \left|W_{12} \frac{\epsilon_{12}}{\epsilon_{12\ max}}\right|\right) \dots \dots \dots \text{(Eq. 6.3)}$$

Where:

f_{max}	Maximum failure criterion
ϵ_1	Longitudinal strain
ϵ_2	Transverse strain
ϵ_{12}	In-plane shear strain
$\epsilon_{1\ max}$	Longitudinal failure strain
$\epsilon_{2\ max}$	Transverse failure strain
$\epsilon_{12\ max}$	In-plane shear failure strain
W_1, W_2, W_{12}	Weighting factors

In ACP, the failure criterion was defined as outlined in Figure 38. The longitudinal, transverse and in-plane shear strains were analysed in conjunction with weighting factors. The weighting (safety) factors were set at the value one for all the failure mode criteria to ensure no bias is created for a failure mode. The advantage of the weighting factors is that they can assist in creating focus on a specific failure mode e.g. If the design may require a higher safety against fibre failure than delamination, then the weighting factor of fibre failure is increased [37]. The results for the failure

Design of a Carbon Fibre Passenger Car Rim

modes are outlined in Figure 39 to Figure 47. It should be noted that the maximum strain failure criterion (all modes) in the hub section would have failure regions (values above one). This is due to the missing aluminium hub section. The results in this section can be considered inaccurate; because the Ducati rim has a proven service record. Rim Technology, Eurotype Test Centre and German TÜV have tested the BST wheel and it has met all requirements with regards to road certification [5].

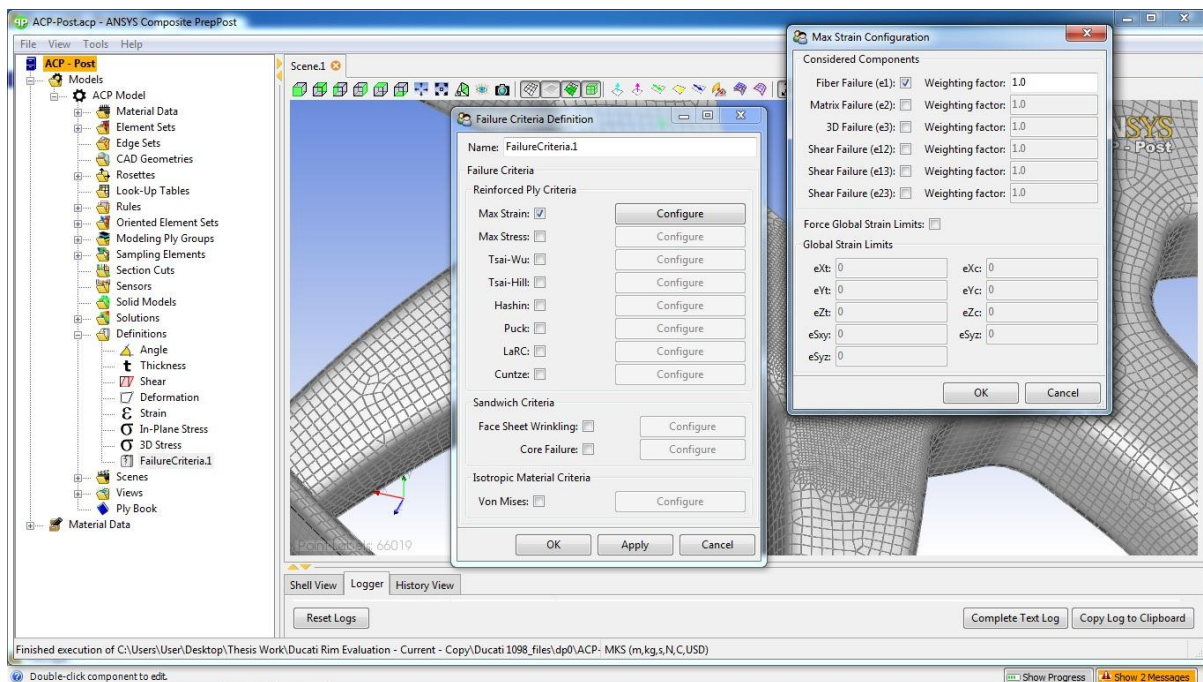


Figure 38 : Defining the Maximum Failure Criterion

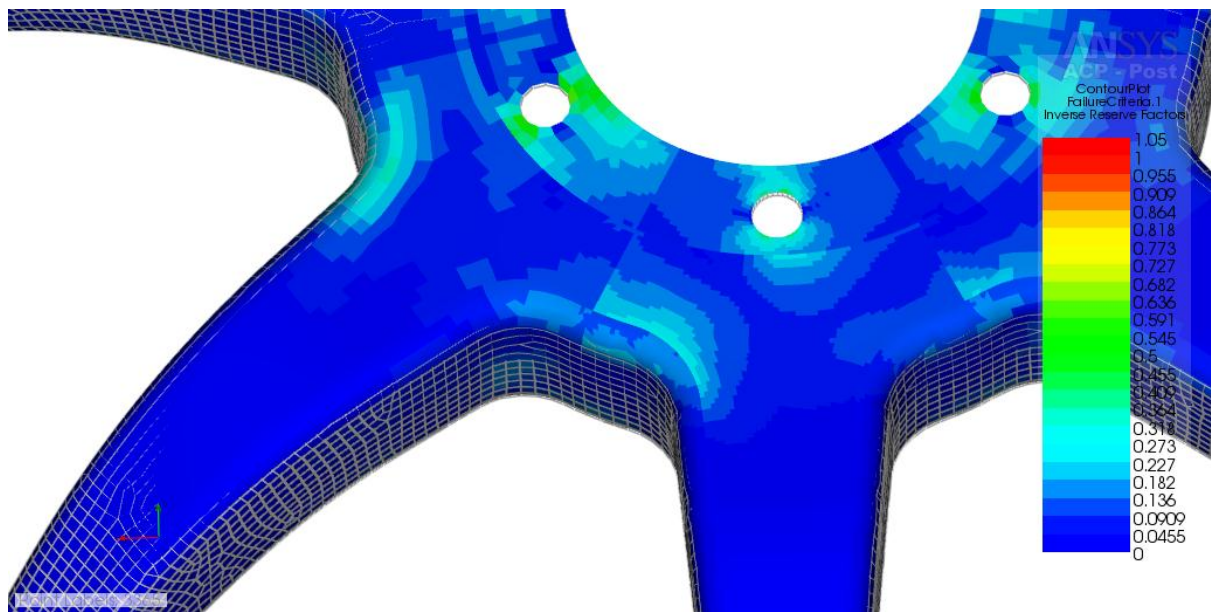


Figure 39: IRF - Longitudinal Strain Mode: Outer Section - Ducati Rim

The IRF in the longitudinal strain mode is illustrated in Figure 39 to Figure 41. The IRF (Figure 39) in the spokes was 0.0909 on the outer section. The IRF (Figure 40, Figure 41) in the spokes was 0.136 on the inner section.

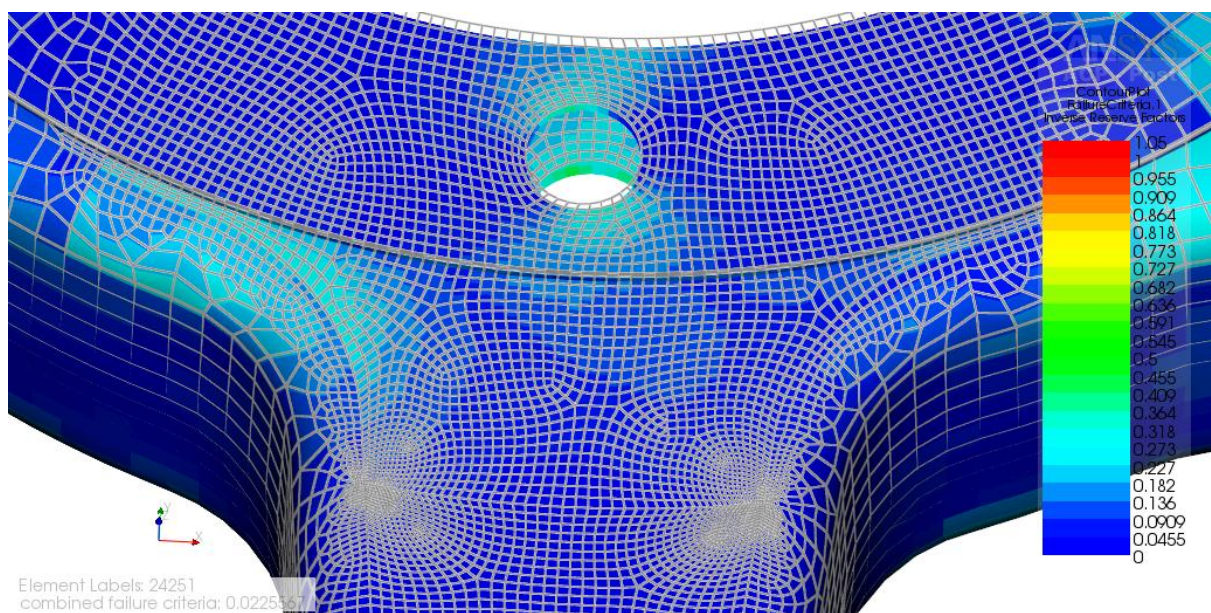


Figure 40: IRF - Longitudinal Strain Mode: Inner Section - Ducati Rim

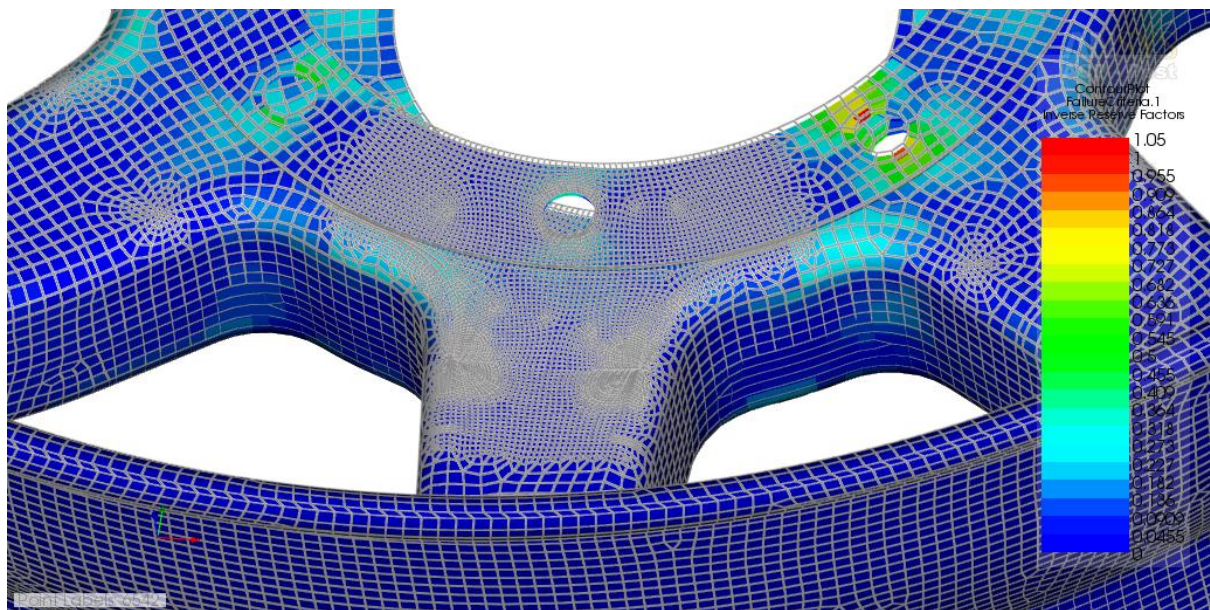


Figure 41: IRF - Longitudinal Strain Mode: Inner Section - Ducati Rim

The IRF in the transverse strain mode is illustrated in Figure 42 to Figure 44. The IRF (Figure 42) in the spokes was 0.136 on the outer section. The IRF (Figure 43, Figure 44) in the spokes was 0.0909 on the inner section.

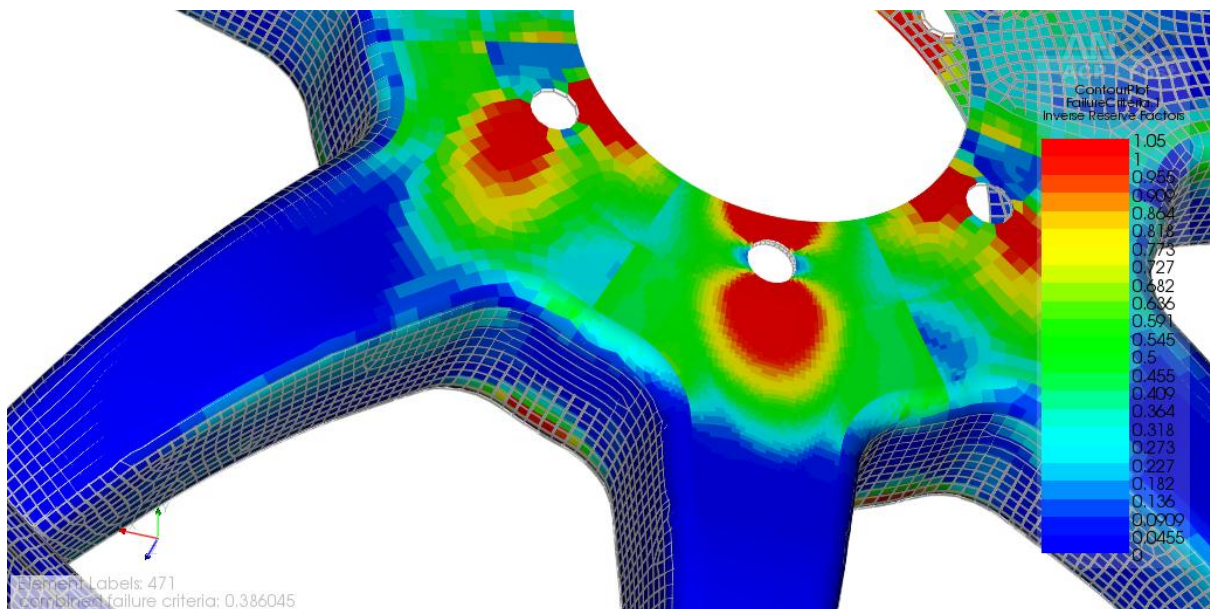


Figure 42: IRF - Transverse Strain Mode: Outer Section - Ducati Rim

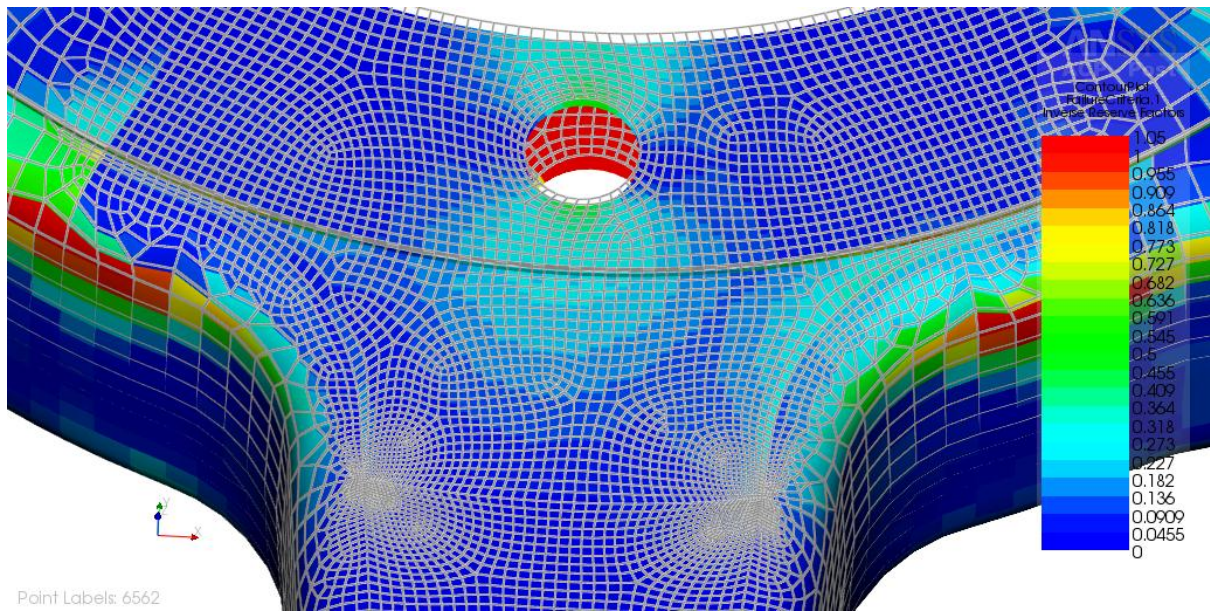


Figure 43: IRF - Transverse Strain Mode: Inner Section - Ducati Rim

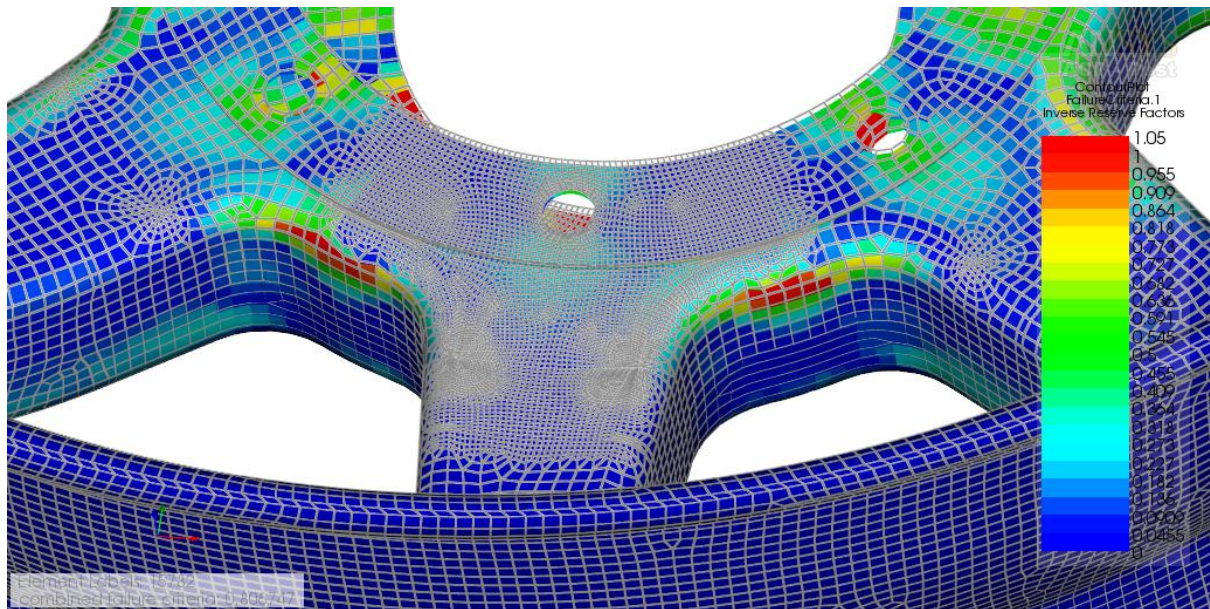


Figure 44: IRF - Transverse Strain Mode: Inner Section - Ducati Rim

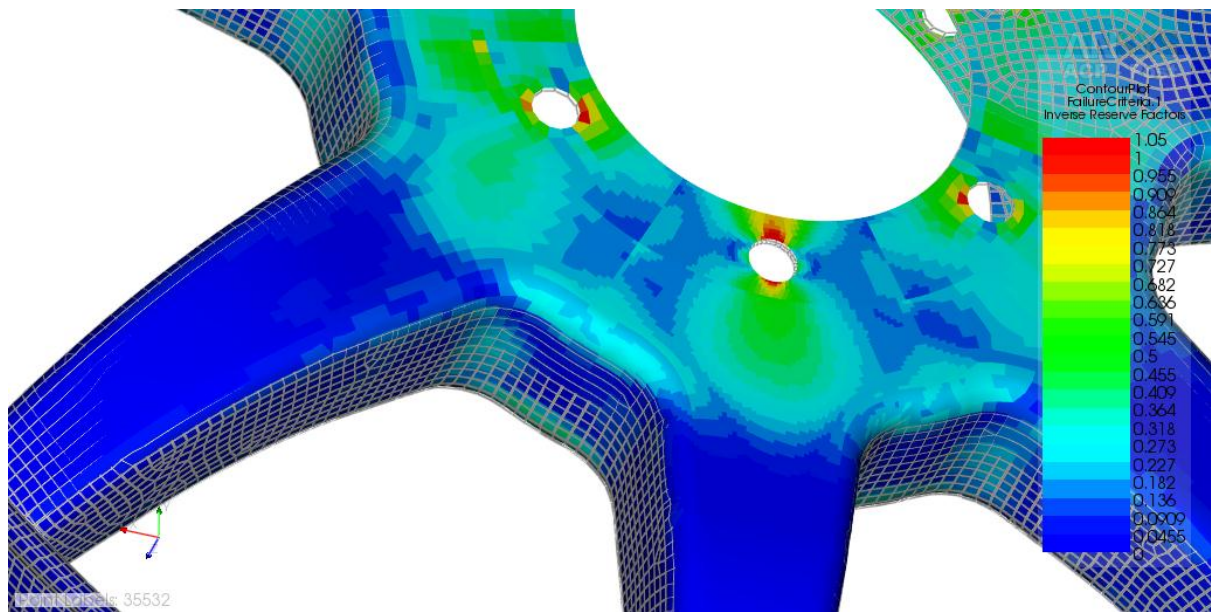


Figure 45: IRF- In Plane Shear Strain Mode: Outer Section - Ducati Rim

The IRF in the in-plane shear strain mode is illustrated in Figure 45 to Figure 47 . The IRF (Figure 45) in the spokes was 0.0909 on the outer section. The IRF (Figure 46, Figure 47) in the spokes was 0.182 on the inner section.

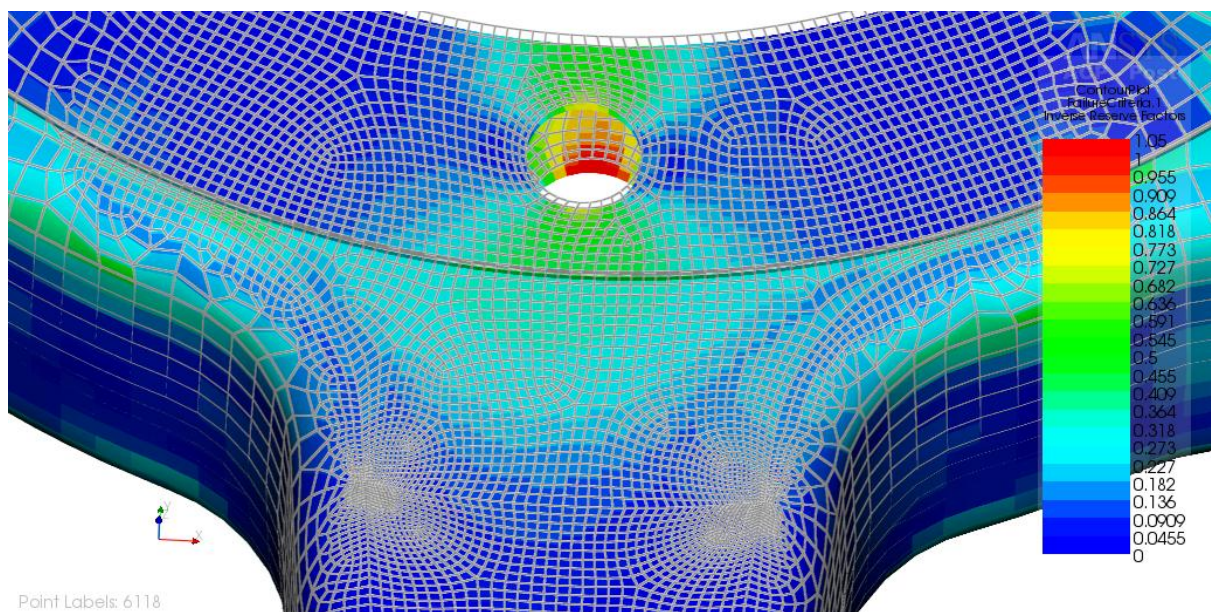


Figure 46: Maximum Strain - In Plane Shear Strain Mode: Inner Section - Ducati Rim

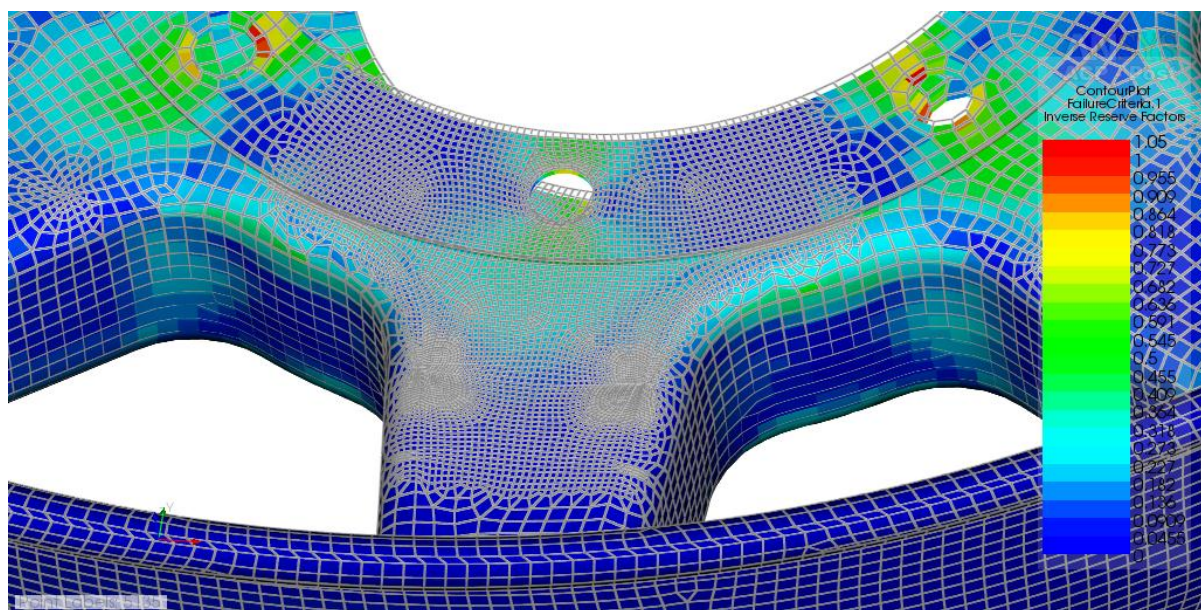


Figure 47: IRF - In Plane Shear Strain Mode: Outer Section - Ducati Rim

In summary, the failure criterion or IRF indicates regions where the strain has exceeded the failure strain of the material. The IRF in the hub section was above 1, which was expected because the hub region was not modelled accurately. The hub region was modelled without the aluminium hub. The IRF from the spoke to the rim section was below 1. This indicates that the rim was structurally durable for its function and the field performance of the rim has proven that. Section 6.2.2 indicated that the spoke section had a higher probability of failure in the shearing (in plane shear) mode, than matrix (transverse strain) and fibre (longitudinal strain) mode in accordance with the maximum strain failure criterion. In chapter 7 the design of the rim was evaluated to accommodate vehicle loads.

Chapter 7: FEA – Passenger Car Rim

In accordance with the German TÜV wheel standard, the bending moment ranges from 2 KNm to 70 KNm for the cornering fatigue test [38]. This standard ranges from light vehicles to heavy vehicles. For the purpose of the research paper the analysis was performed on a passenger car rim that experiences a 2000 Nm during the dynamic cornering fatigue test. The test essentially caters for rims that will be utilised for Category M₁ motor vehicles as classified by Government Gazette 30917. The gazette defines M₁ motor vehicles as a carriage of passengers that has at least four wheels, which can accommodate not more than 8 passengers including the driver [38].

Table 6: Example of Bending Moment Calculation for the Vehicle

Bending Moment			
Vehicle (kg)	2331	d (m)	0
4 passengers (kg)	400	μ	0.7
Luggage load (kg)	100	F	1.5
Total Mass (kg)	2831	r_dyn (m)	0.2286
F_r (N) 30 % load of total load on worst loaded rim	8332	M_max (Nm)	2000

The 2000 Nm bending moment caters for vehicle mass limit of 2331 kg as illustrated in Table 6. This was calculated using equation 2.1, in order to confirm that the common sedan, hatch and SUV can utilise this rim design. The bending moment was chosen because it structurally caters for rims of vehicles such as the Polo Vivo, Ford Focus, Ford Kuga, Toyota Yaris, and Golf Gti etc.

The passenger car rim was constrained on the rim flange as illustrated in Figure 48. A 2000 N remote force was applied 1 m away from hub as illustrated in Figure 48. The force was attached to the bolt holes on the inner and outer hub. The results outlining the design of a passenger car carbon fibre rim are illustrated below.

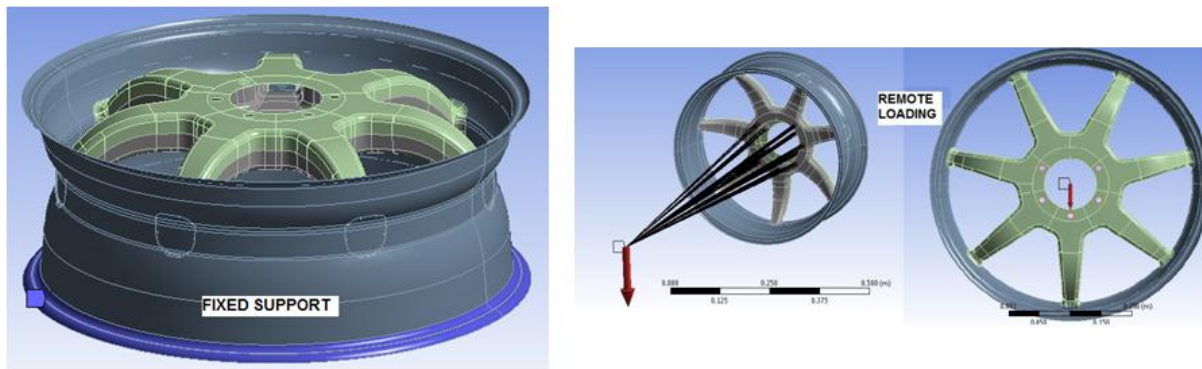


Figure 48: Load Case of Passenger Vehicle Carbon Fibre Rim

The first step was to expose the Ducati rim to vehicle loads, in order to evaluate the strain patterns the wheel experiences before any modifications were done. The cornering fatigue test setup was similar to the Ducati rim in chapter 6, but the remote force applied was 2000 N instead of 700 N. The results are illustrated in section 7.1.

7.1 Ducati Rim Exposed to Passenger Vehicle Loads

7.1.1 Strains

The longitudinal strains of the Ducati rim are illustrated in Figure 49 and Figure 50. The longitudinal strains in the spoke region were $2000 \mu\epsilon$ and $-2640 \mu\epsilon$ for the outer and inner spoke respectively.

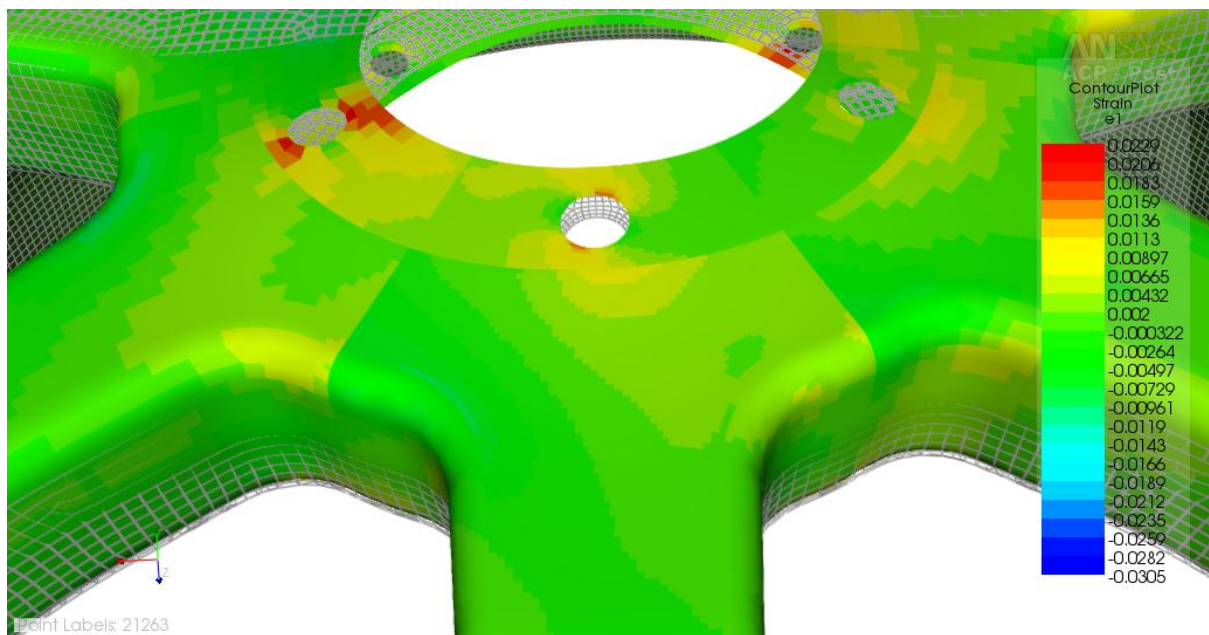


Figure 49: Longitudinal Strains: Outer Section - Ducati Rim (2000 Nm)

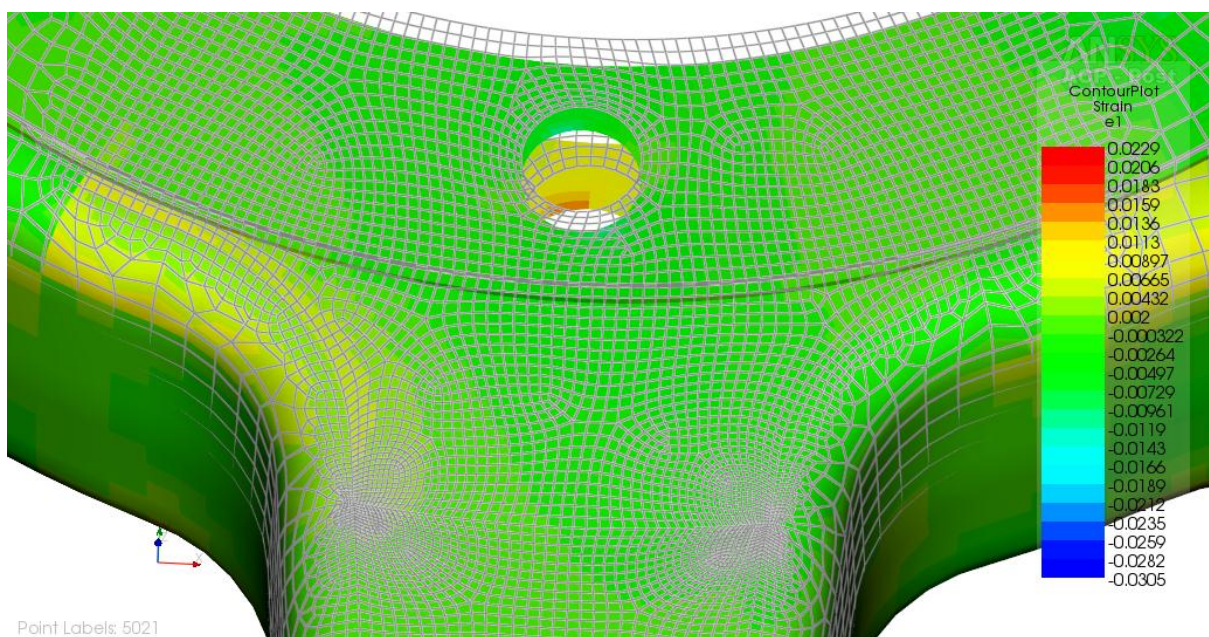


Figure 50: Longitudinal Strains: Inner Section - Ducati Rim (2000 Nm)

The transverse strains of the Ducati rim are illustrated in Figure 51 and Figure 52. The transverse strains in the spoke region were $1210 \mu\epsilon$ and $-3530 \mu\epsilon$ for the outer and inner spoke respectively.

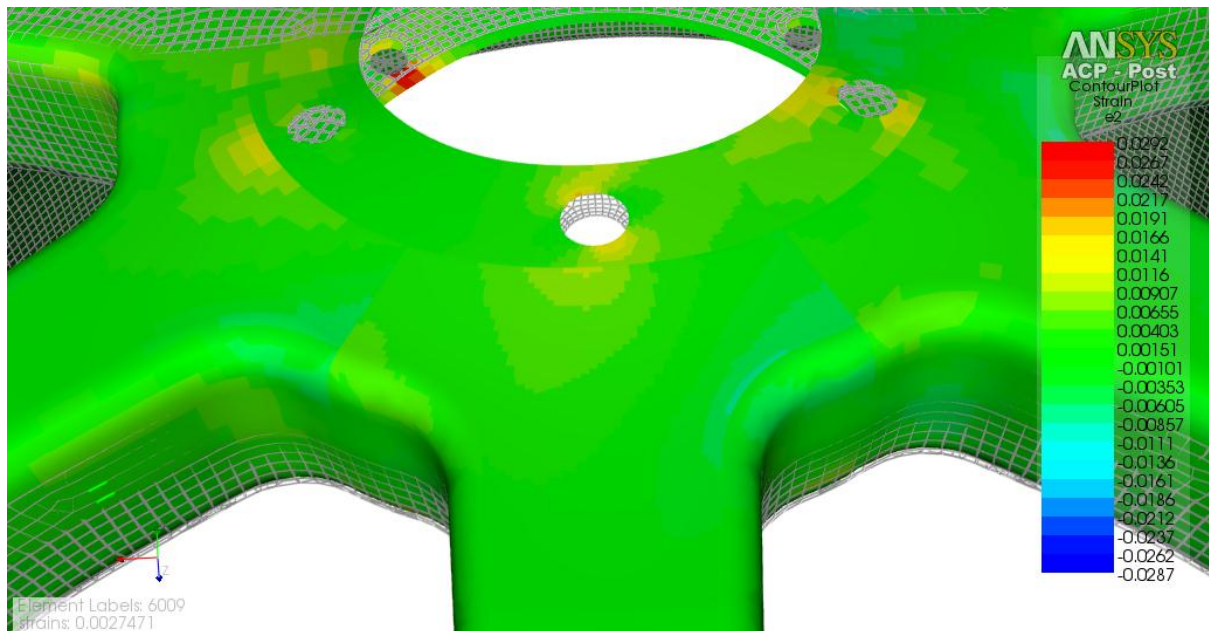


Figure 51: Transverse Strains: Outer Section - Ducati Rim (2000 Nm)

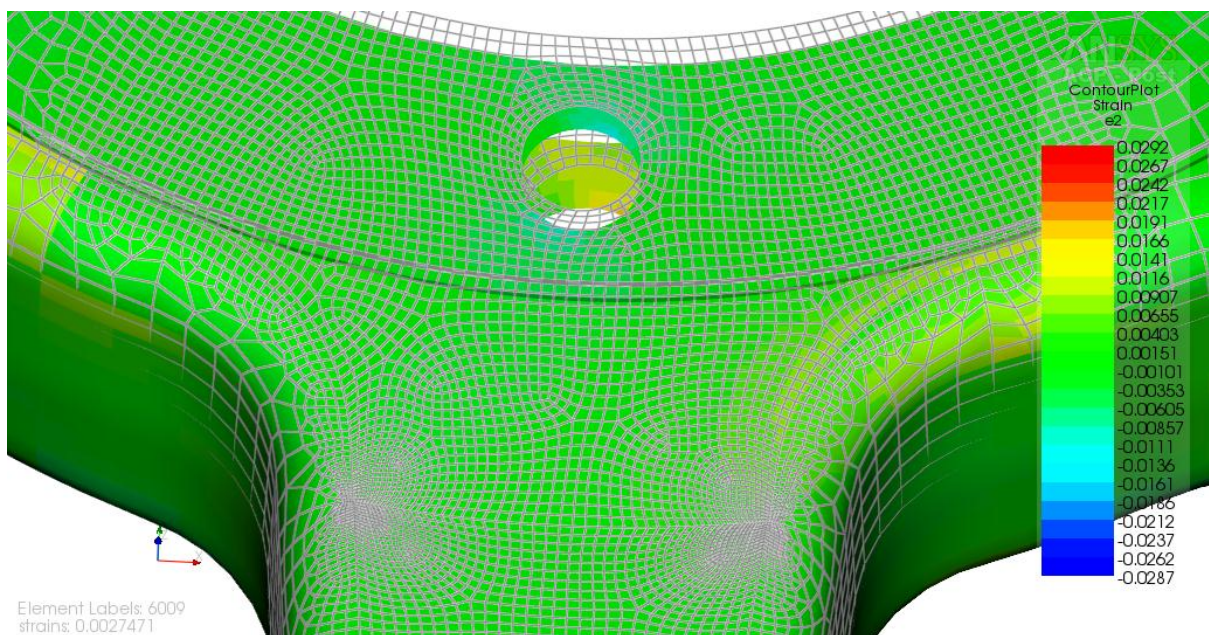


Figure 52: Transverse Strains: Inner Section - Ducati Rim (2000 Nm)

The in planes shear strains of the Ducati rim are illustrated in Figure 53 and Figure 54. The in planes shear strains in the spoke region were $3880 \mu\epsilon$ and $-4780 \mu\epsilon$ for the outer and inner spoke respectively.

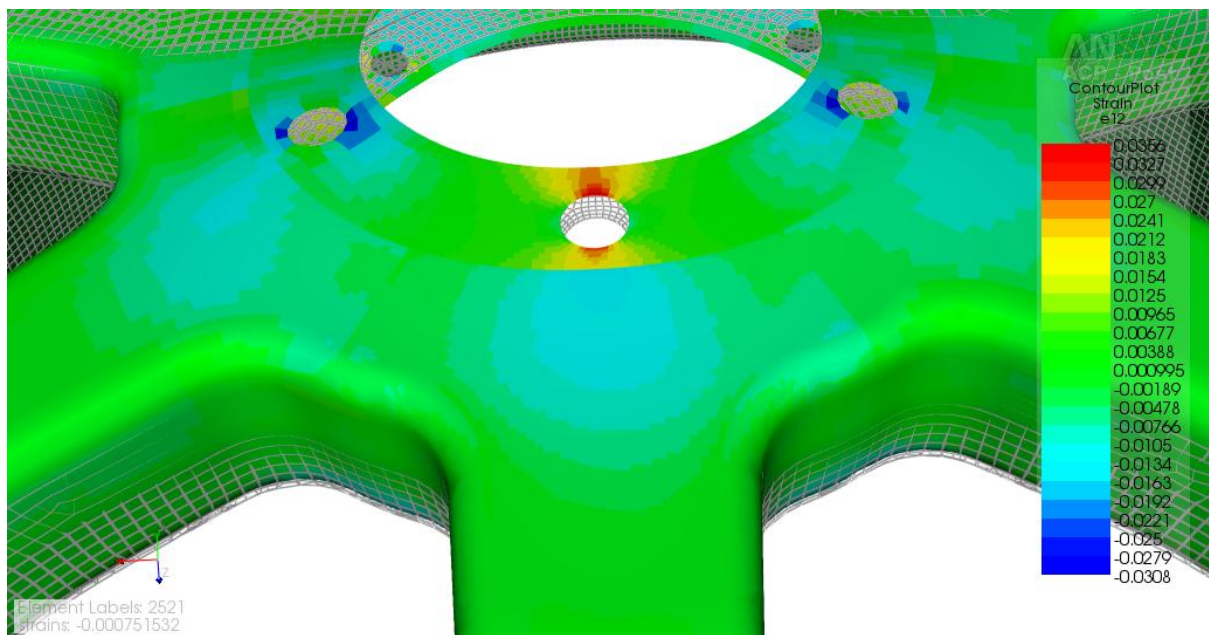


Figure 53: In Plane Shear Strain: Outer Section - Ducati Rim (2000 Nm)

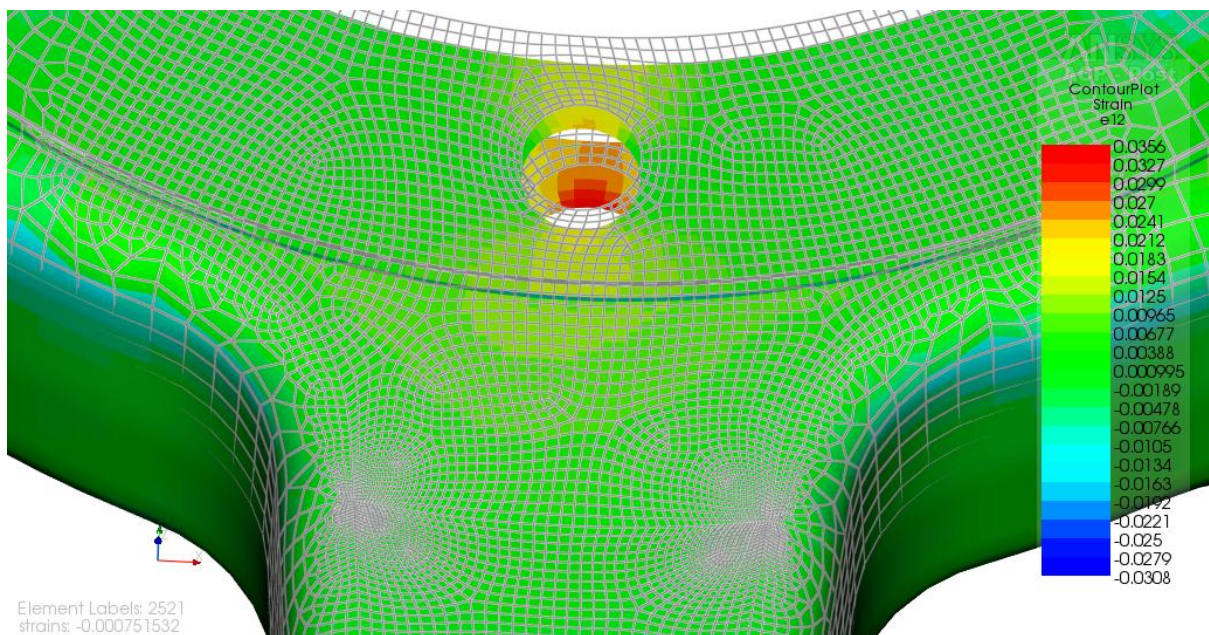


Figure 54: In Plane Shear Strain: Inner Section - Ducati Rim (2000 Nm)

The strain patterns were similar to those described in section 6.2.1, but higher in comparison, due to the larger bending moment. The strains were generally higher in the transition zones between the hub, spokes and the rim. The strain patterns indicate that strain reduction was required in the hub, spokes, and rim. Strain reduction was especially required in the interface zone between the components.

The design of the passenger vehicle carbon fibre rim was iterative to obtain a feasible design. The design of the passenger vehicle is outlined in section 7.2 and 7.3. In these sections the FEA methodology is outlined, which entailed model preparation, material design and the loading for the rim. These aspects are similar to the Ducati rim setup and the differences will be highlighted to avoid duplication.

The strain results were crucial and assisted in understanding the Ducati rim at higher loads. The results illustrate the strain patterns for the longitudinal, transverse and in plane shear strains. The results can be utilised to compare the passenger rim to the Ducati rim at lower (700 Nm) and higher (2000 Nm) loads. This assisted in quantifying the improvement in the design of the passenger rim.

7.1.2 Maximum strain failure criterion

The IRF in the longitudinal strain mode is illustrated in Figure 55 and Figure 56. The IRF (Figure 55) in the spokes was 0.409 on the outer section. The IRF (Figure 56) in the spokes was 0.409 on the inner section.

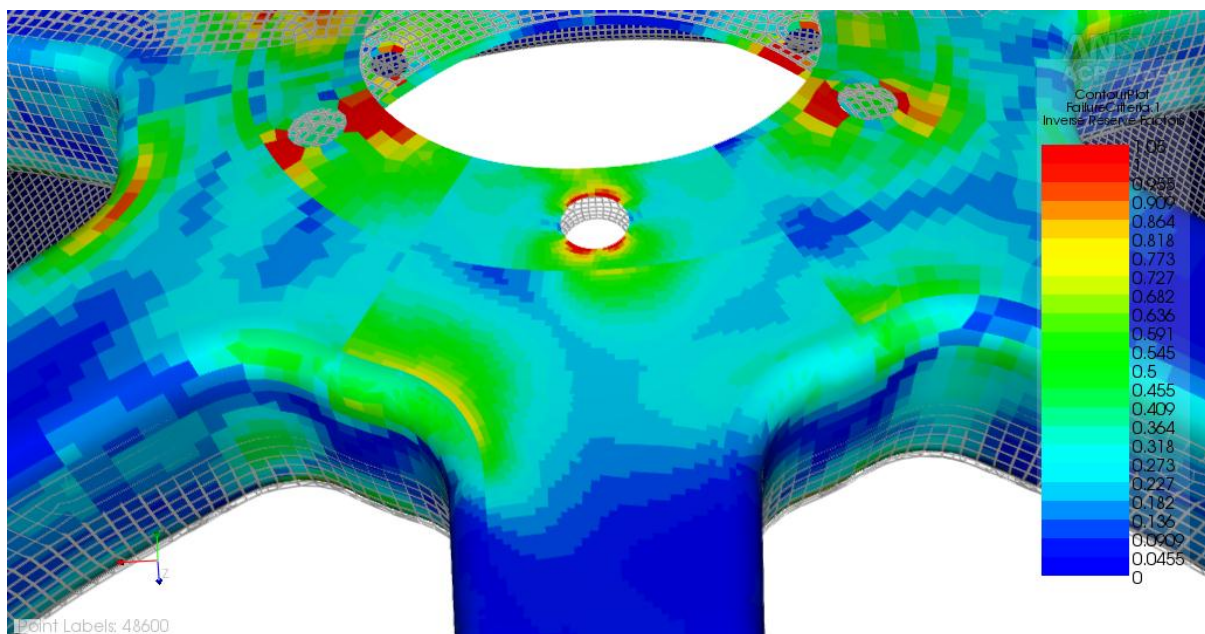


Figure 55: IRF- Longitudinal Strain Mode: Outer Section - Ducati Rim (2000 Nm)

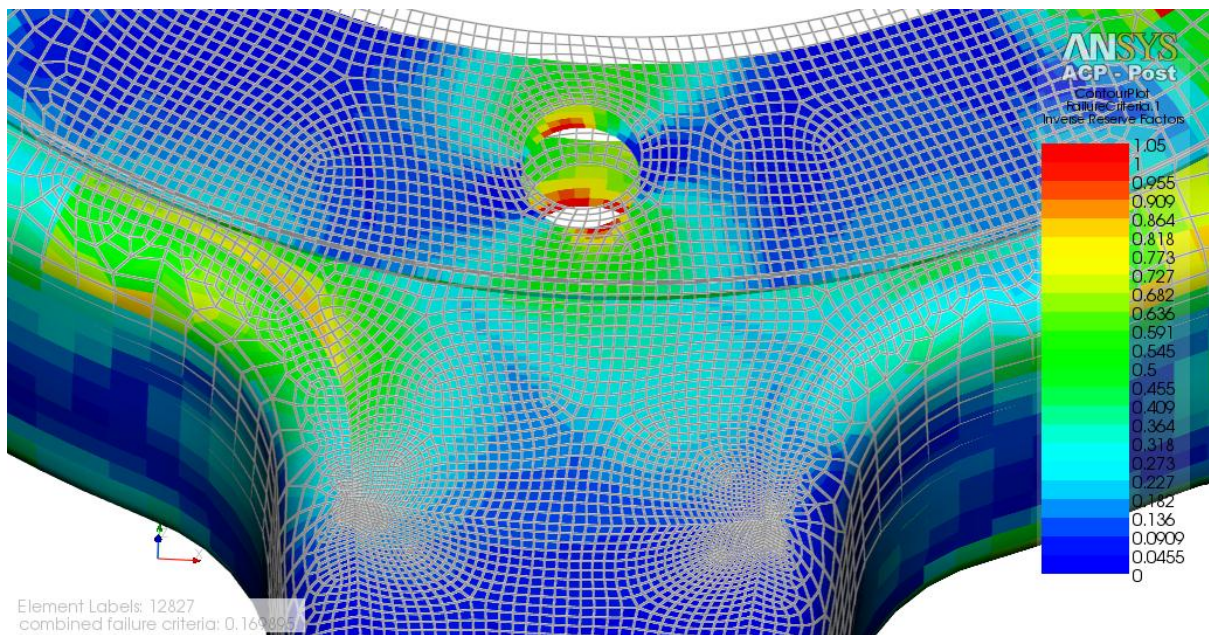


Figure 56: IRF - Longitudinal Strain Mode: Inner Section - Ducati Rim (2000 Nm)

The IRF in the transverse strain mode is illustrated in Figure 57 and Figure 58. The IRF (Figure 57) in the spokes was 0.636 on the outer section. The IRF (Figure 58) in the spokes was 0.409 on the inner section.

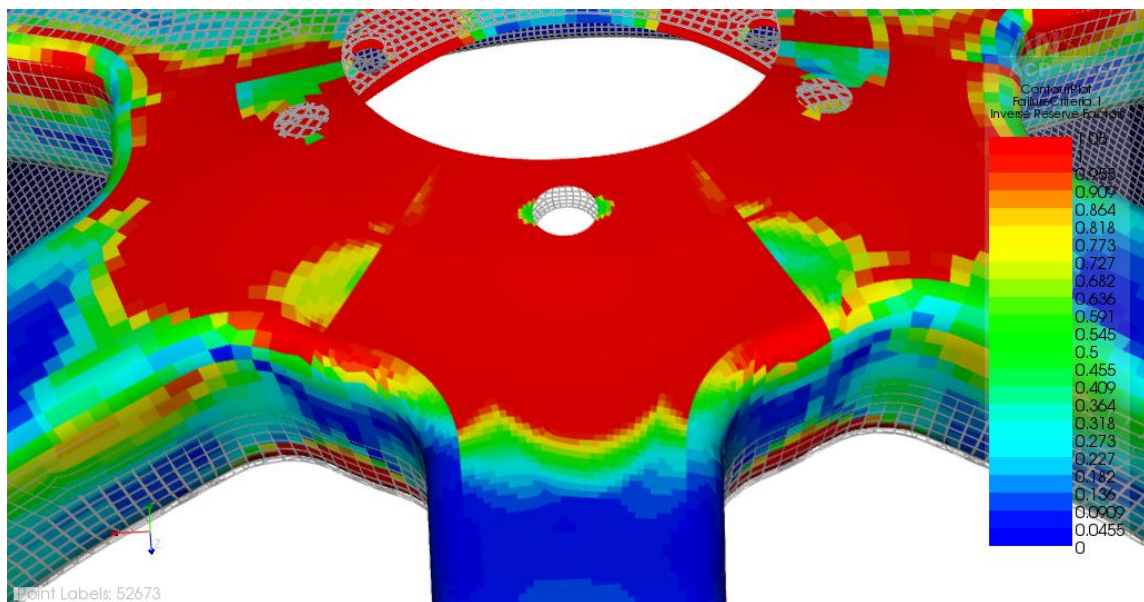


Figure 57: IRF - Transverse Strain Mode: Outer Section - Ducati Rim (2000 Nm)

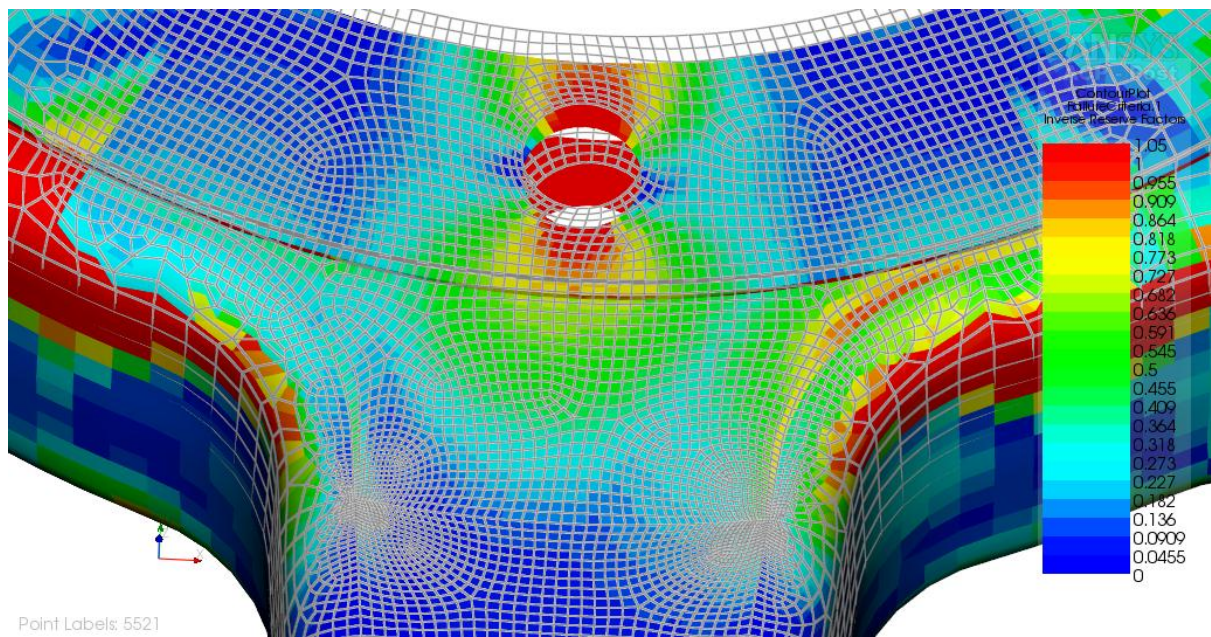


Figure 58: IRF- Transverse Strain Mode: Inner Section - Ducati Rim (2000 Nm)

The IRF in the in plane shear strain mode is illustrated in Figure 59 and Figure 60. The IRF (Figure 59) in the spokes was 0.636 on the outer section. The IRF (Figure 60) in the spokes was 0.682 on the inner section.

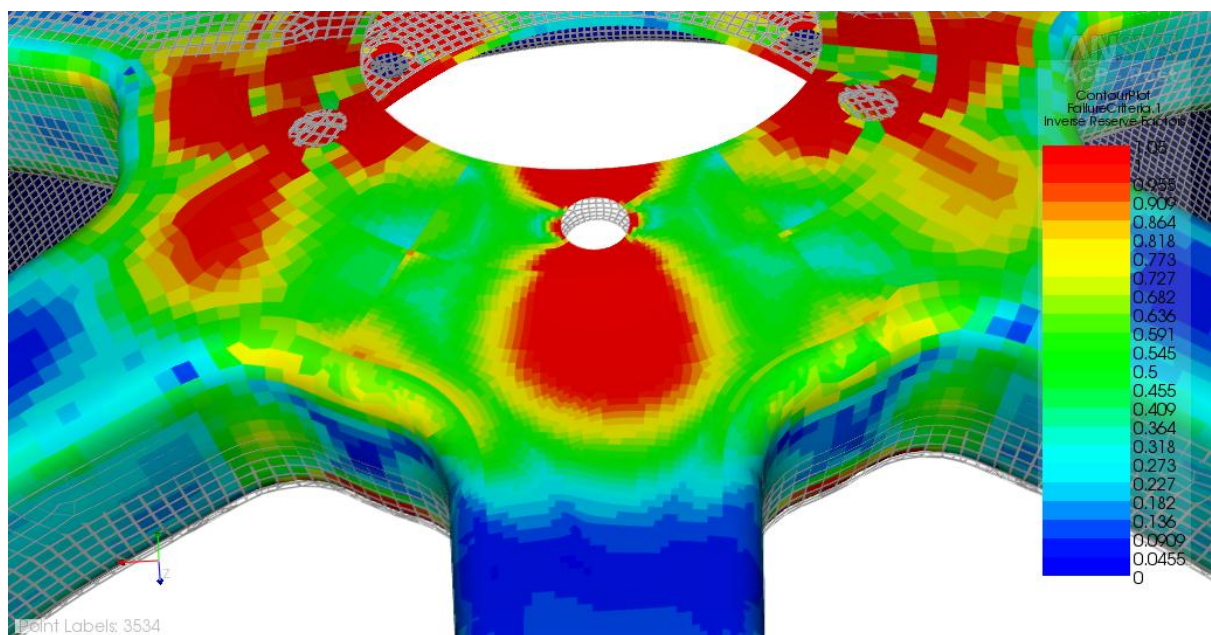


Figure 59: IRF - In Plane Shear Strain Mode: Outer Section - Ducati Rim (2000 Nm)

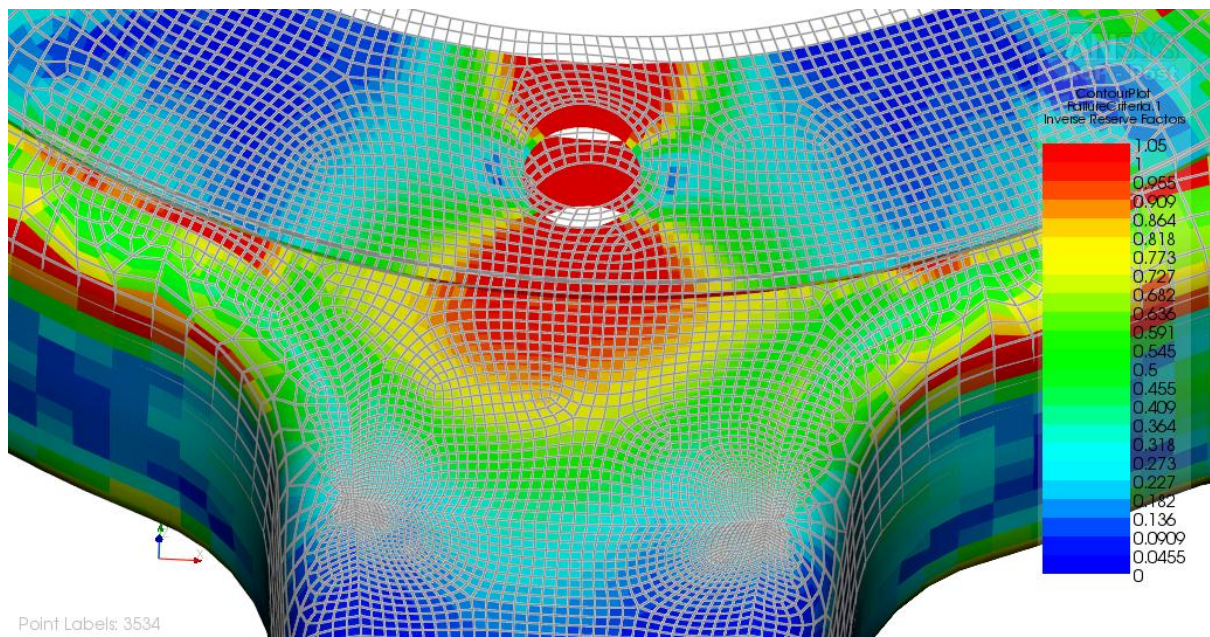


Figure 60: IRF - In Plane Shear Strain Mode: Inner Section - Ducati Rim (2000 Nm)

The IRF in the hub section was above 1, which was expected because the hub region was not modelled accurately. Section 7.1.2 indicated that the spoke section had a higher probability of failure in the shearing (in plane shear) mode, than matrix (transverse strain) and fibre (longitudinal strain) mode in accordance with the maximum strain failure criterion. The IRF will be compared to passenger rim results in section 7.3.

7.2 Model Preparation

The existing 1098 Ducati surface CAD model was the reference point for the vehicle rim design. The project schematic as illustrated in Figure 13 was the flow path followed in the design. The existing material as illustrated in Table 3 was used in the new design. The process of the design was iterative, with respect to segmentation, stacking sequence and meshing. These items are discussed further in the report.

7.2.1 Segmentation

Segmentation of the rim was essential in the build-up of the passenger car rim. The rim was segmented using named selections. This allowed for geometric definition of the parts on the rim. The named selections (segments) illustrated in Figure 15 to Figure 18 were still valid for the passenger car rim, except for the inner hub and outer hub. The alterations to the hub segments are illustrated in Figure 61. The hub was extended into the spoke section to ensure that there was reduction of strain in the hub to spoke transition zone. The applicable coordinate systems are illustrated in Figure 19 and Figure 20 for the respective segments as discussed in 6.1.3.2.

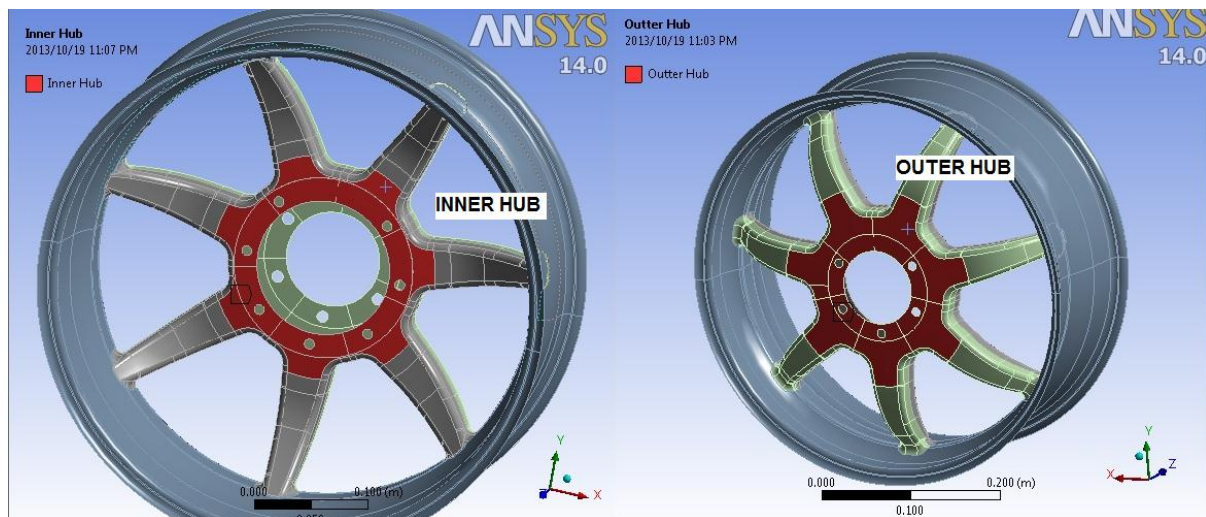


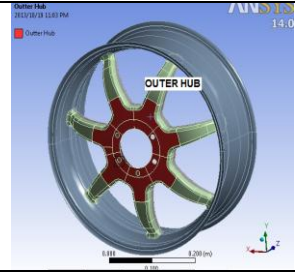
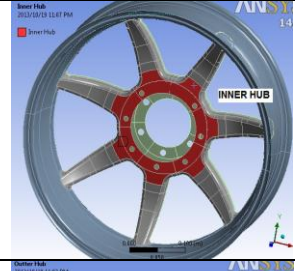
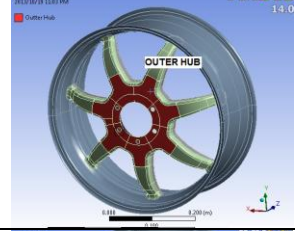

Figure 61: Passenger Car Carbon Fibre Rim Hub Segments

7.2.2 Stacking sequence

The stacking sequence is illustrated in Table 7 and was very similar to the original 1098 Ducati rim layup. The stacking sequence was modelled in the modelling plys of Pre ACP. The stacking sequence resulted in a thickness variation as illustrated in Figure 62 and Figure 63. The increased thickness in the transition zones between the hubs, spokes and the rim ensured the passenger rim had the required structural integrity. The thickness variation of the laminate; varies from 6.2 mm thick at the hub to 4.04 mm thick at the spokes, to 2.16 mm thick at the rim section (beads excluded).

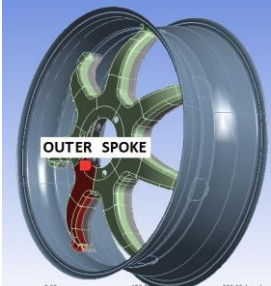
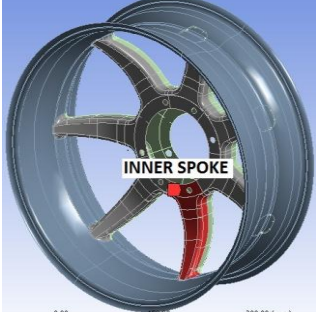

Design of a Carbon Fibre Passenger Car Rim

Table 7: Stacking Sequence of the Passenger Car Carbon Fibre Rim: Hub Section

Segment Name	Ply Type	Ply Orientation	Phase 1 : Quantity
	1.T300 woven	0° & $\pm 45^\circ$	Three
	1.T300 woven	0° & $\pm 45^\circ$	Three
	1.T700 Woven	$1. 0^\circ$ & $\pm 45^\circ$	1. Nine per hub
	1.T700 Woven	$1. 0^\circ$ & $\pm 45^\circ$	1. Nine per hub


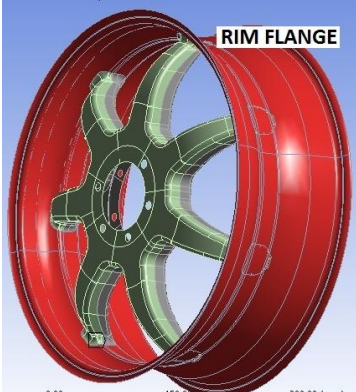
Design of a Carbon Fibre Passenger Car Rim

Table 8: Stacking Sequence of the Passenger Car Carbon Fibre Rim: Spoke Section

Segment Name	Ply Type	Ply Orientation	Phase 1 : Quantity
	1. T300 woven 2. T700 unidirectional 3. T300 woven	1. $\pm 45^\circ$ 2. UD 3. $\pm 45^\circ$	1. Three per spoke 2. Four per spoke 3. Three per spoke
	1. T300 woven 2. T700 unidirectional 3. T300 woven	1. $\pm 45^\circ$ 2. UD 3. $\pm 45^\circ$	1. Three per spoke 2. Four per spoke 3. Three per spoke
	1. T300 Woven	1. $\pm 45^\circ$	1. Rolled three times around intensifiers


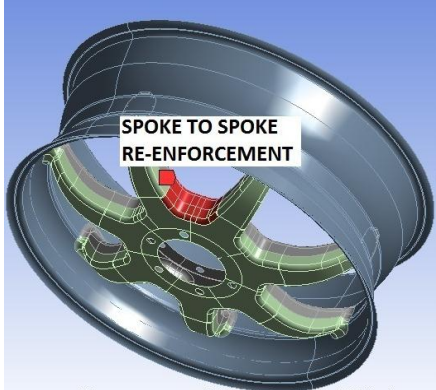
Design of a Carbon Fibre Passenger Car Rim

Table 9: Stacking Sequence of the Passenger Car Carbon Fibre Rim: Rim Section

Segment Name	Ply Type	Ply Orientation	Phase 1 : Quantity
	2.T300 woven	$\pm 45^\circ$	Three arc between spokes on the inner and outer section of the rim
	1.T700 woven	1. $\pm 45^\circ$	1. Rolled nine times around the rim.
<p>Plies for bead formation excluded in layup, please refer to original 1098 Ducati rim design.</p>			

Design of a Carbon Fibre Passenger Car Rim

Table 10: Stacking Sequence of the Passenger Car Carbon Fibre Rim: Rim Re-enforcement

Segment Name	Ply Type	Ply Orientation	Phase 1 : Quantity
	1.T300 woven	0/90°	Three per spoke on inner and outer section of the rim
	1.T300 woven	1. ±45°	1. Five layers between spokes.

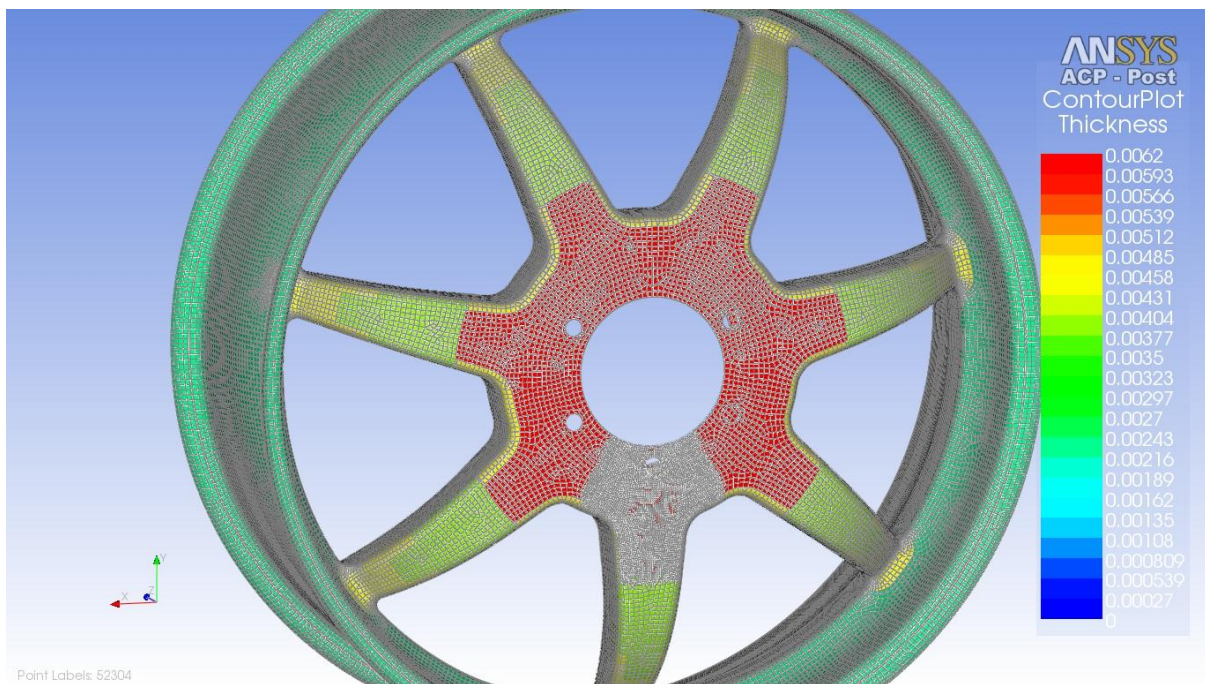


Figure 62: Thickness Variation: Passenger Car Rim

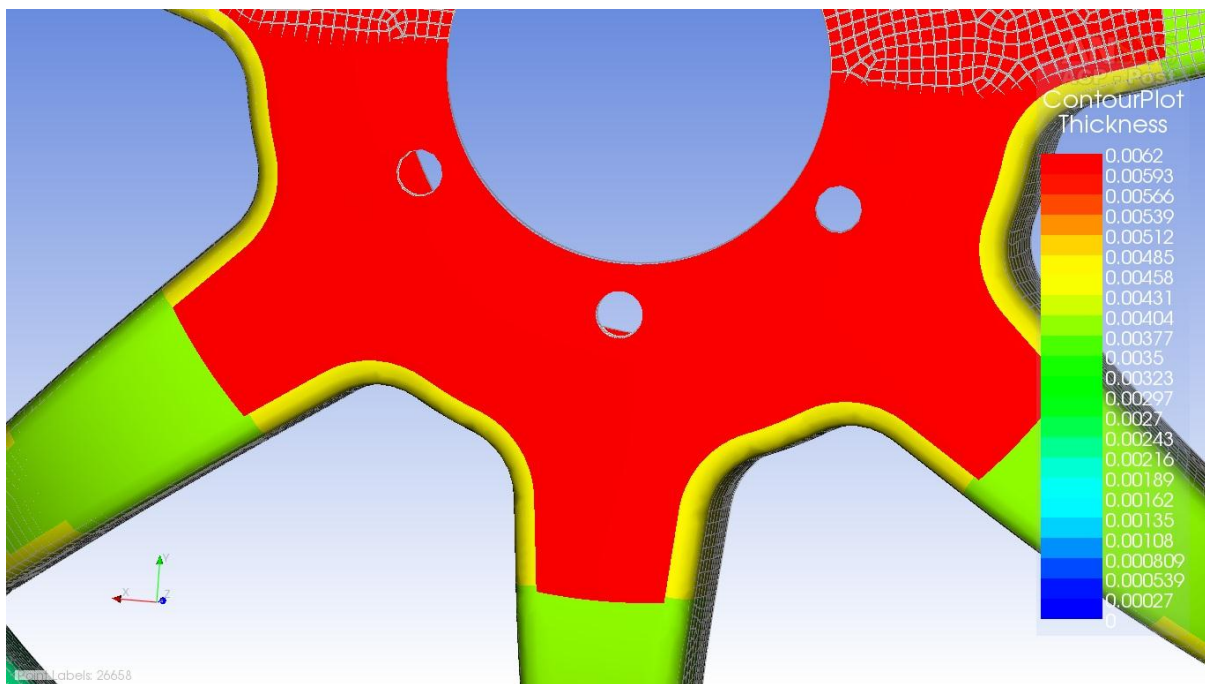


Figure 63: Thickness Variation: Outer Section- Passenger Car Rim

7.2.3 Meshing

Shell 181 elements were utilised in analysing the layers of the composite passenger car rim. The mesh was refined as illustrated in Figure 64 in order to evaluate the mesh sizing. The refined spoke was in line with the force application and the strain results extracted from the spoke were compared to the Ducati rim strain gauge results.

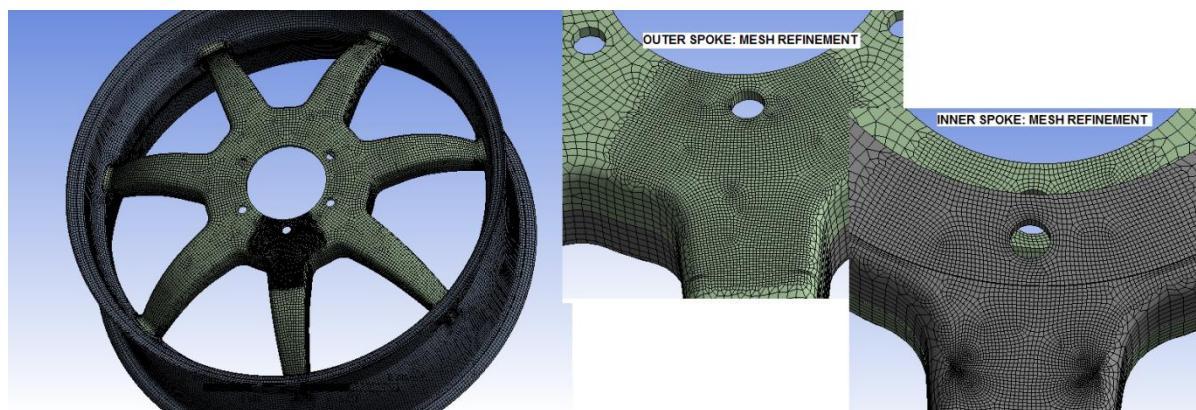


Figure 64: Refinement of the Passenger Car Mesh

The mesh sizing relevance centre and smoothing was set to a medium and the minimum size was 0.5795 mm. There were 69091 nodes and 69069 elements. The refinement of the illustrated sections in Figure 64 was such that the mesh was two times smaller than the rest of the rim geometry mesh. The refinement of the mesh caused a small change in the results as illustrated in Table 4.

Table 11: Evaluation of Mesh Sizing (Passenger Car Rim)

Strain	Medium Size Mesh	Refined Mesh	Difference
Longitudinal- 1 Axis ($\mu\epsilon$)	688.11	688.39	0.04%
Transverse- 2 Axis ($\mu\epsilon$)	16.057	16.065	0.05%
In Plane Shear -12 Axis ($\mu\epsilon$)	-126.45	-126.501	0.04%

The discretization error and element size analysis was conducted on the refined spoke region. A strain probe was placed to evaluate convergence of the results. The mesh was initially medium size and it was later refined, in order to compare the two

stages. It was evident that the refinement of the mesh caused a small change in the results; indicating that the sizing of the mesh was appropriate. The FEA results of the passenger car carbon fibre rim are illustrated in section 7.3.

7.3 Result Evaluation: Passenger Vehicle Rim

The strain flow patterns for the passenger car rim are similar to the Ducati rim when exposed to the motorcycle loads. The strain results were considerably reduced due to the new layup in comparison to the Ducati rim exposed to vehicle loads. The longitudinal, transverse and in plane shear strain of the spokes are essential to evaluate the structural integrity of the passenger car rim as illustrated in section 7.2.1.

7.3.1 Strains

The longitudinal, transverse and in-plane shear strain patterns are similar to the Ducati rim. The longitudinal strain for the passenger car was illustrated in Figure 65 and Figure 66. The longitudinal strains on the outer and inner spoke were $335 \mu\epsilon$ and $-466 \mu\epsilon$ respectively. This illustrates that the outer spoke experiences the largest strain in the fibre direction.

The transverse strain of the passenger car is illustrated in Figure 67 and Figure 68. The transverse strains of the outer and inner spoke were $189 \mu\epsilon$ and $-532 \mu\epsilon$ respectively. The in-plane shear strain of the Ducati rim is illustrated in Figure 69 and Figure 70. The in-plane shear strains for the outer and inner spoke were $460 \mu\epsilon$ and $-650 \mu\epsilon$ respectively. The strains obtained were used to calculate the longitudinal directional strains that can be compared to the FEA results of the Ducati rim. The strains were obtained using equation 2.4. The results are illustrated in Table 12.

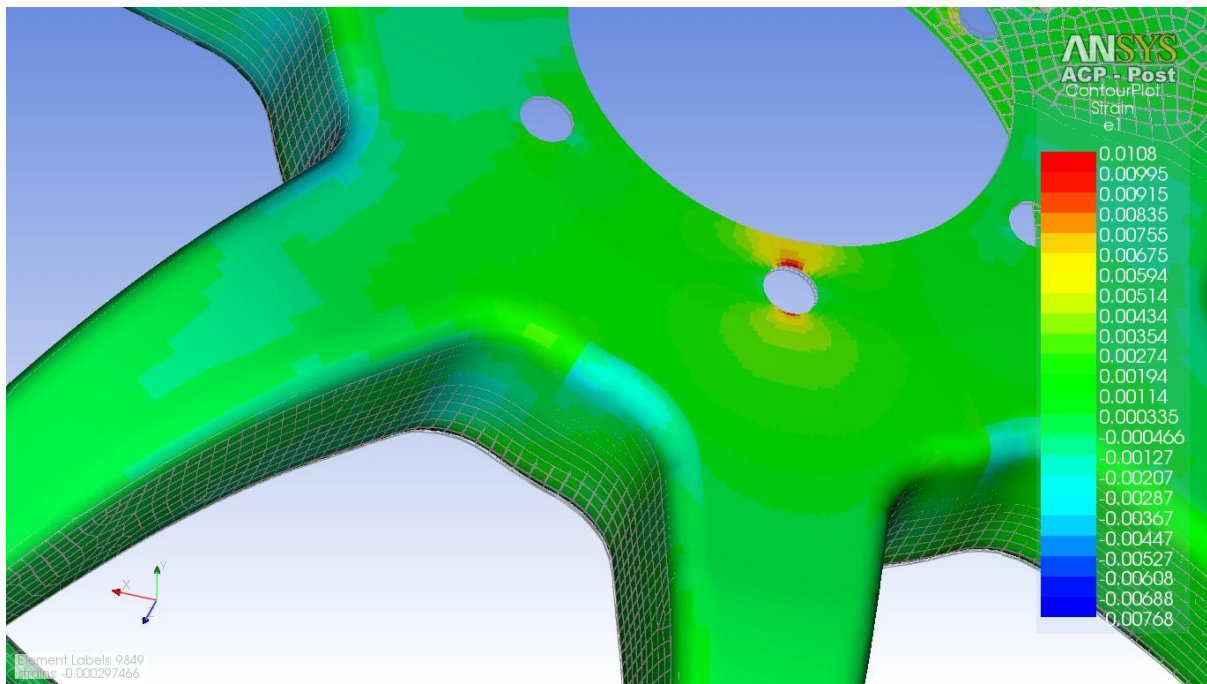


Figure 65: Longitudinal Strain: Outer Section - Passenger Car Rim

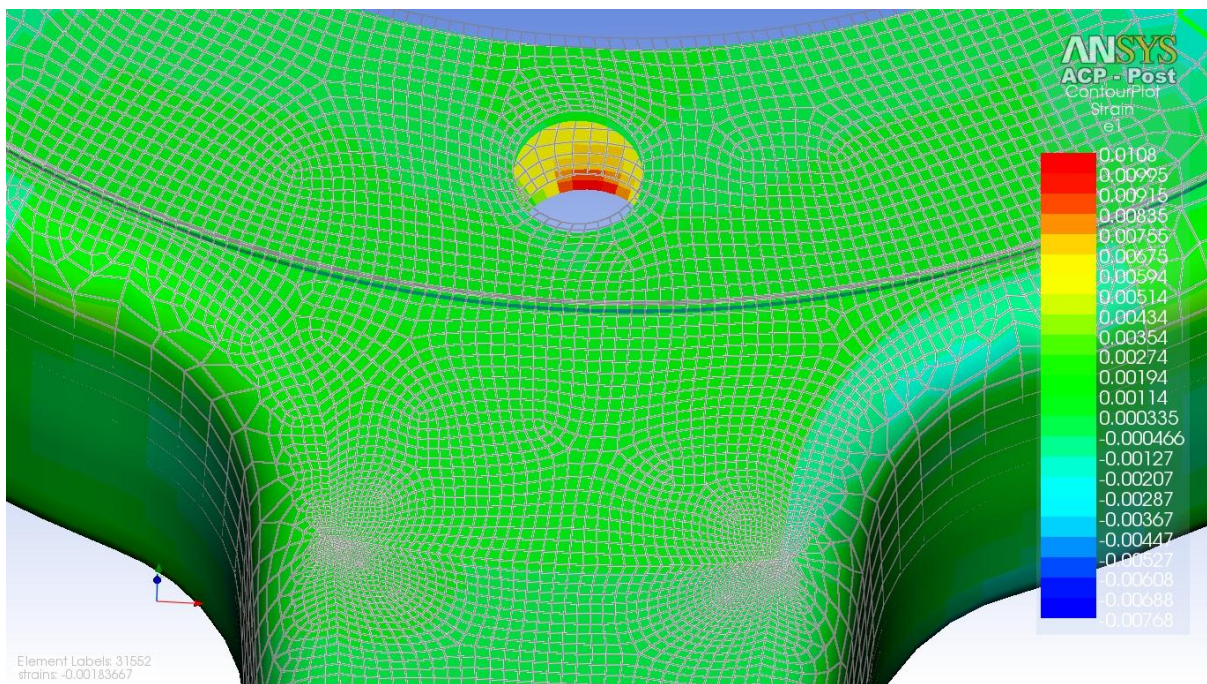


Figure 66: Longitudinal Strain: Inner Section - Passenger Car Rim

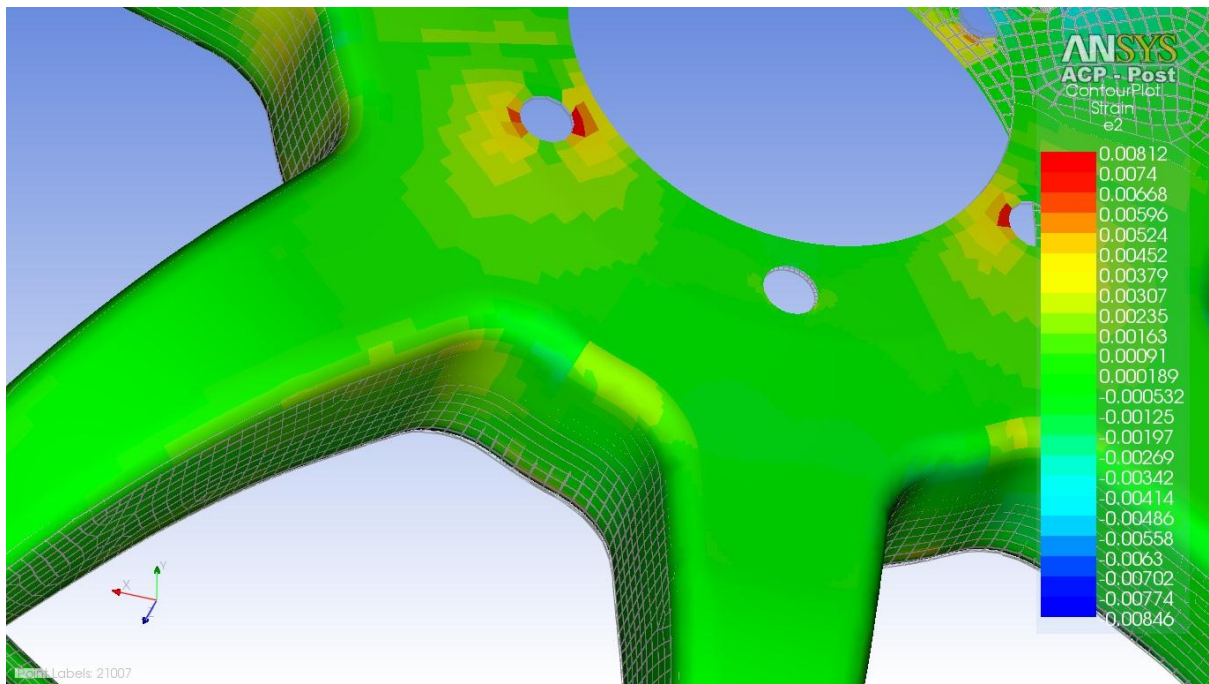


Figure 67: Transverse Strain: Outer Section - Passenger Car Rim

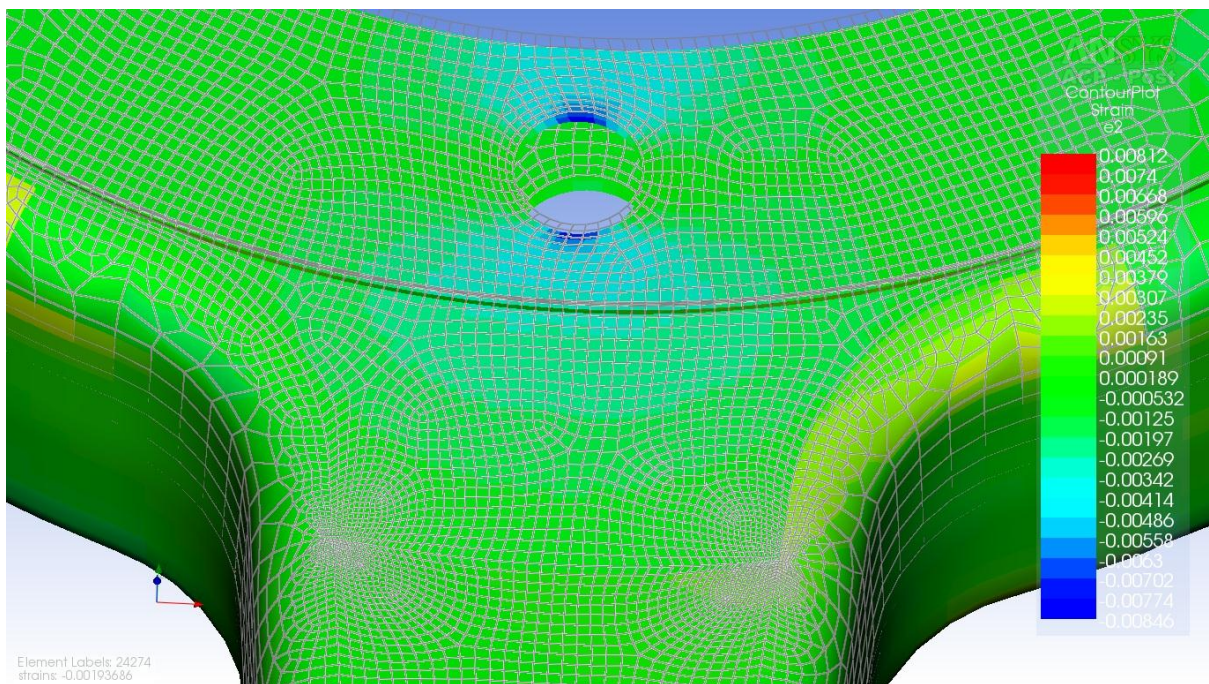


Figure 68: Transverse Strain: Inner Section - Passenger Car Rim

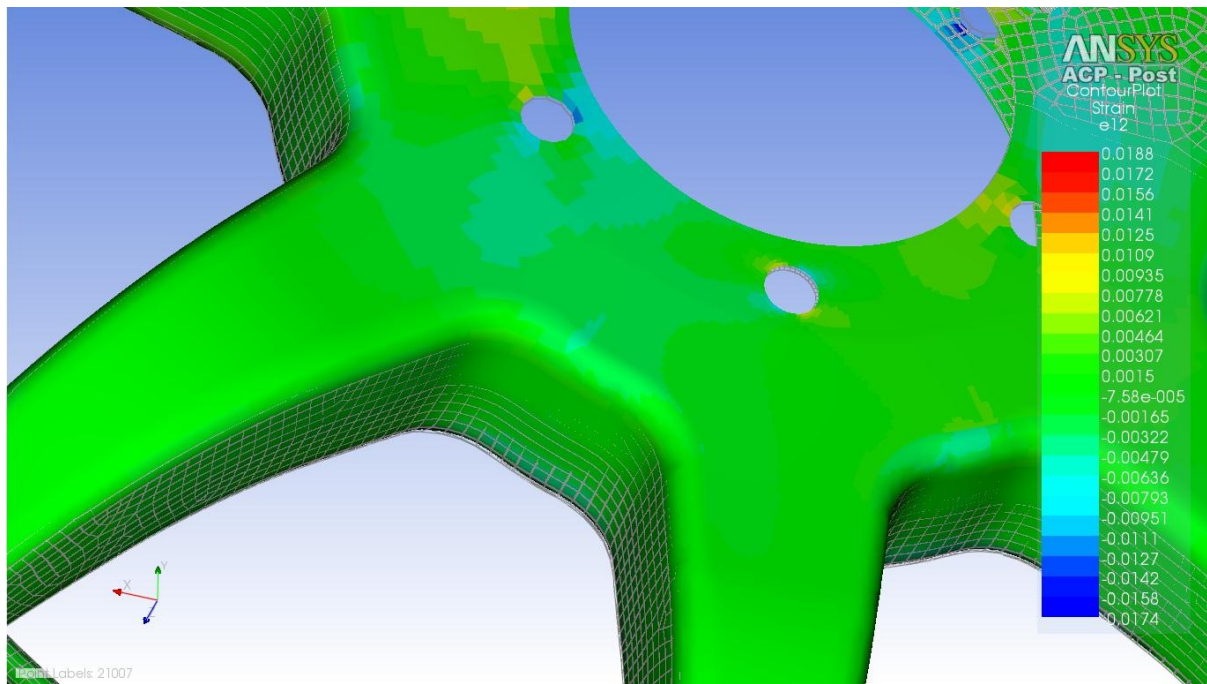


Figure 69: In-Plane Shear Strain: Outer Section - Passenger Car Rim

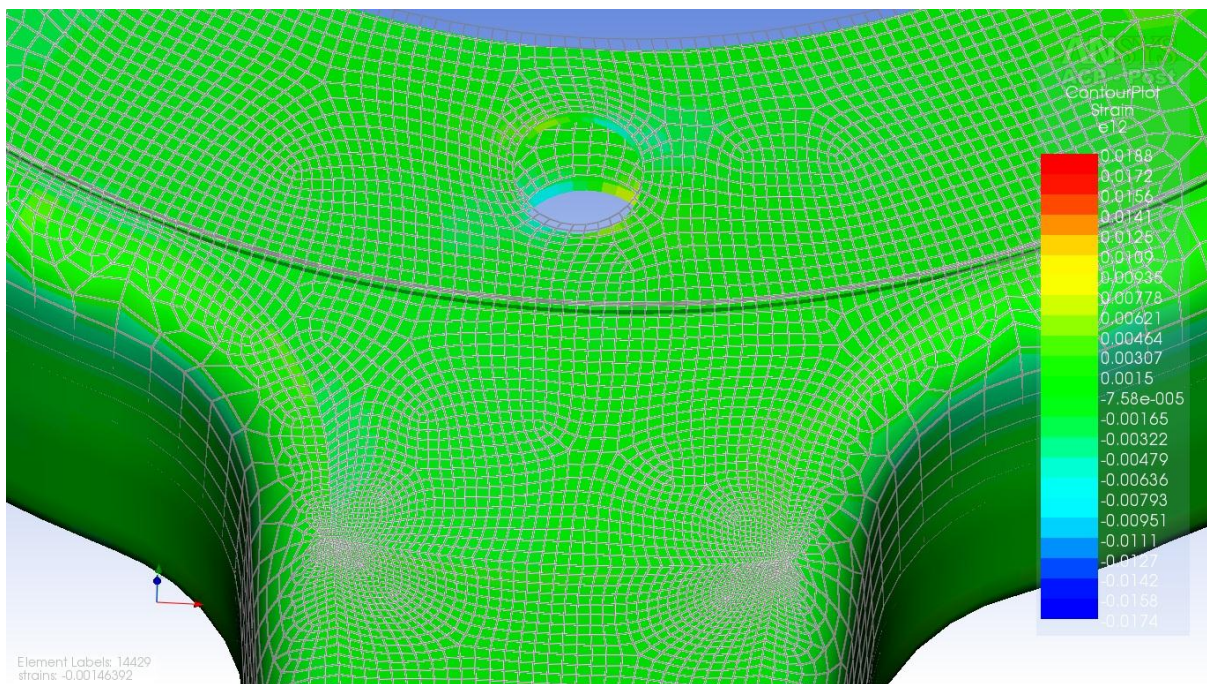


Figure 70: In-Plane Strain: Inner Section - Passenger Car Rim

Table 12: Comparison of the FEA strain of Passenger Car and Ducati Rim

STEP 1	FEA INPUTS						
		Inner (Back) Spoke			Outer (Front) Spoke		
	ϵ_1	-466 $\mu\epsilon$			335 $\mu\epsilon$		
	ϵ_2	-532 $\mu\epsilon$			189 $\mu\epsilon$		
ϵ_{12}	-630 $\mu\epsilon$			460 $\mu\epsilon$			
STEP 2	STRAIN OUTPUTS (EQ. 2.4)						
		Inner Spoke			Outer Spoke		
	ϵ_0	-466 $\mu\epsilon$			335 $\mu\epsilon$		
ϵ_{45}	-935 $\mu\epsilon$			639 $\mu\epsilon$			
STEP 3	COMPARISON OF FEA RESULTS						
		Inner Spoke (Ducati-FEA)	Inner Spoke (Car- FEA)	Diff. (%)	Outer Spoke (Ducati-FEA)	Outer Spoke (Car- FEA)	Diff. (%)
	ϵ_0	-113 $\mu\epsilon$	-466 $\mu\epsilon$	76 %	164 $\mu\epsilon$	335 $\mu\epsilon$	51 %
	ϵ_{45}	-498 $\mu\epsilon$	-935 $\mu\epsilon$	47 %	295 $\mu\epsilon$	638 $\mu\epsilon$	53 %

Table 12 illustrates that the passenger rim generally experienced higher strain in comparison to the Ducati rim exposed to 700 Nm. Table 13 illustrates that the passenger rim resulted in an average 85% improvement in the strains when compared to the Ducati rim when exposed to 2000 Nm. This illustrates that the passenger rim was able to handle the higher vehicle loads, given that the strains are still generally low. This was substantiated by the maximum strain failure criterion evaluation in section 7.3.2.

Table 13: Comparison of the Ducati (2000 Nm) and Passenger Rim Strains

Strains	Ducati Rim (2000Nm)		Passenger Car (2000Nm)		Difference	
	Inner Spoke	Outer Spoke	Inner Spoke	Outer Spoke	Inner Spoke	Outer Spoke
ϵ_1 ($\mu\epsilon$)	-2640	2000	-466	335	82%	83%
ϵ_2 ($\mu\epsilon$)	-3530	1210	-532	189	85%	84%
ϵ_{12} ($\mu\epsilon$)	-4780	3880	-630	460	87%	88%

7.3.2 Maximum strain failure criterion

The maximum strain evaluation process of the passenger rim was similar to the process followed in section 6.2.2. The value for the weighting factor for all the failure modes was one. This was to ensure that the failure modes could be compared fairly. The IRF in the longitudinal strain mode is illustrated in Figure 71 to Figure 73. The IRF (Figure 71) in the spokes was 0.136 on the outer section. The IRF (Figure 72, Figure 73) in the spokes was 0.136 respectively on the inner section.

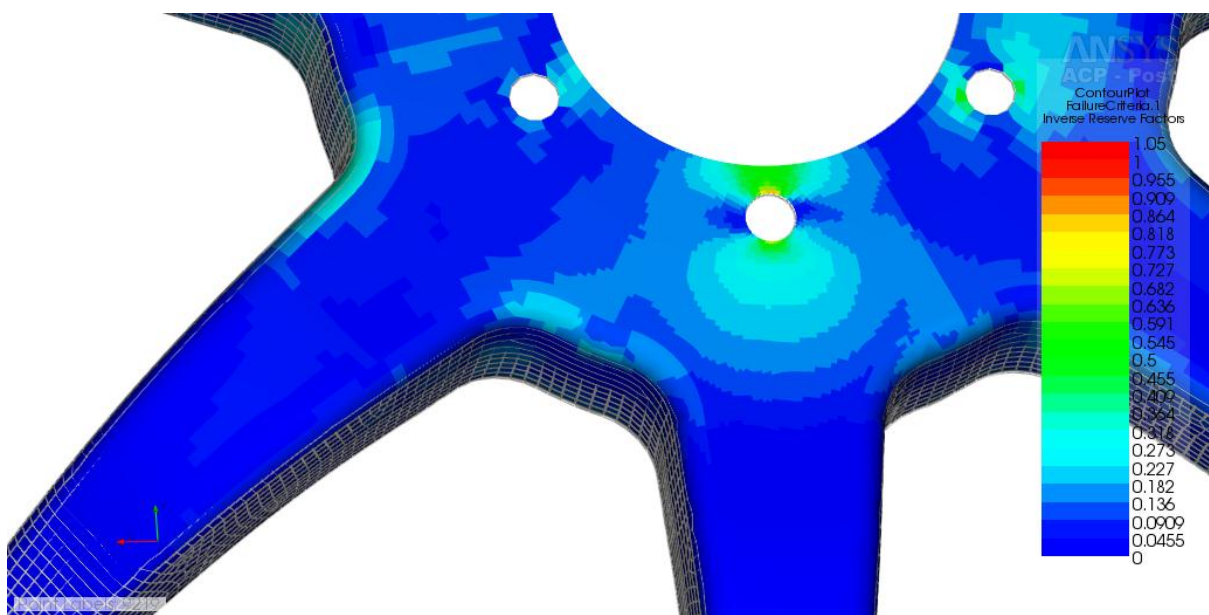


Figure 71: Maximum Strain Failure Criterion - Longitudinal Strain Mode: Outer Section - Passenger Rim

Design of a Carbon Fibre Passenger Car Rim

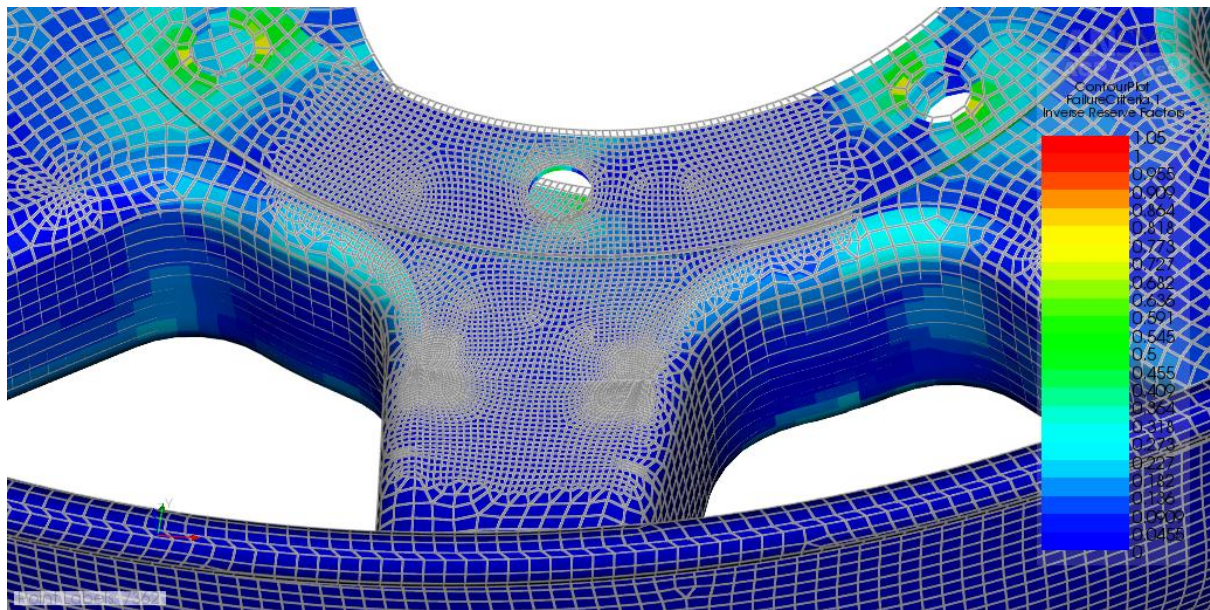


Figure 72: IRF - Longitudinal Strain Mode: Inner Section - Passenger Rim

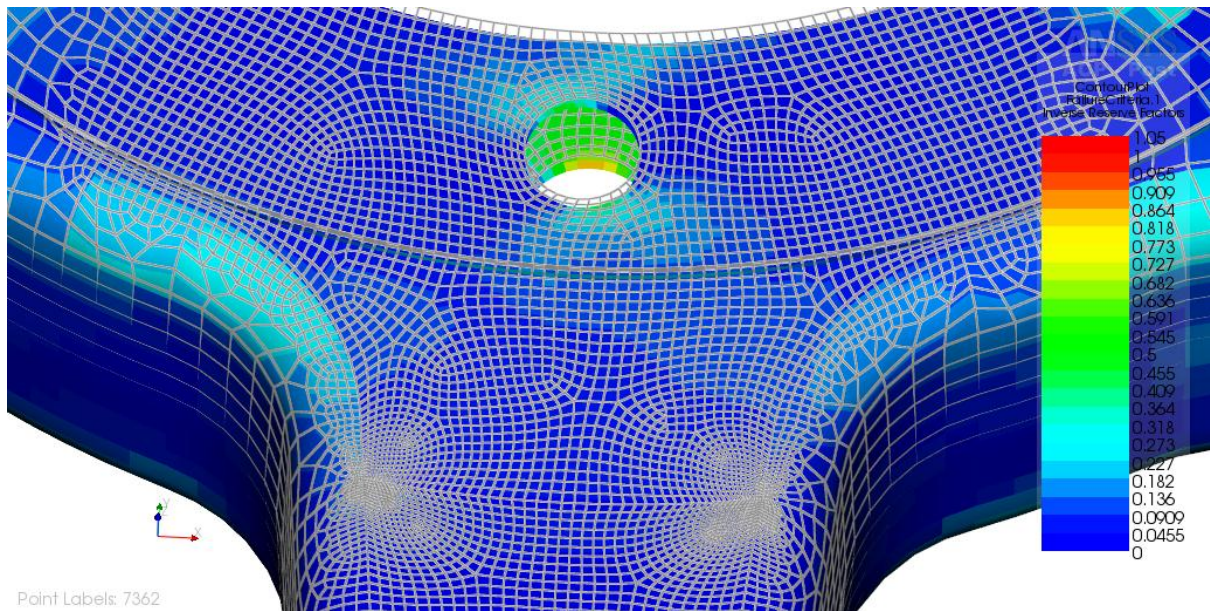


Figure 73: IRF - Longitudinal Strain Mode: Inner Section - Passenger Rim

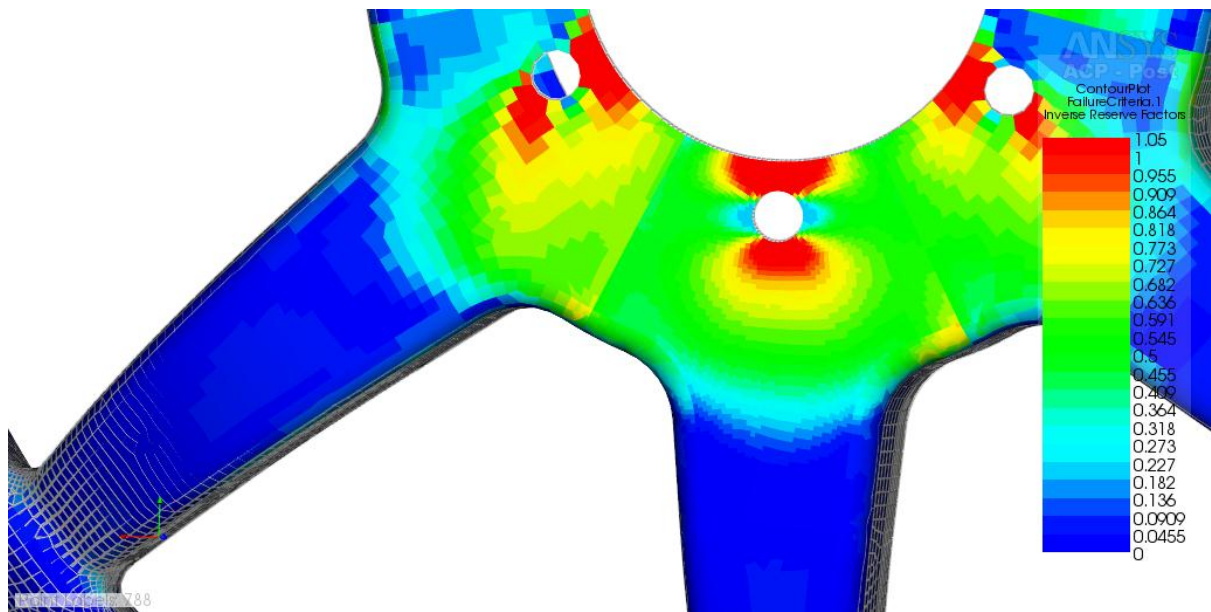


Figure 74: IRF - Transverse Strain Mode: Outer Section - Passenger Rim

The IRF in the transverse strain mode is illustrated in Figure 74 to Figure 76 . The IRF (Figure 74) in the spokes was 0.227 on the outer section. The IRF (Figure 75, Figure 76) in the spokes was 0.136 on the inner section.

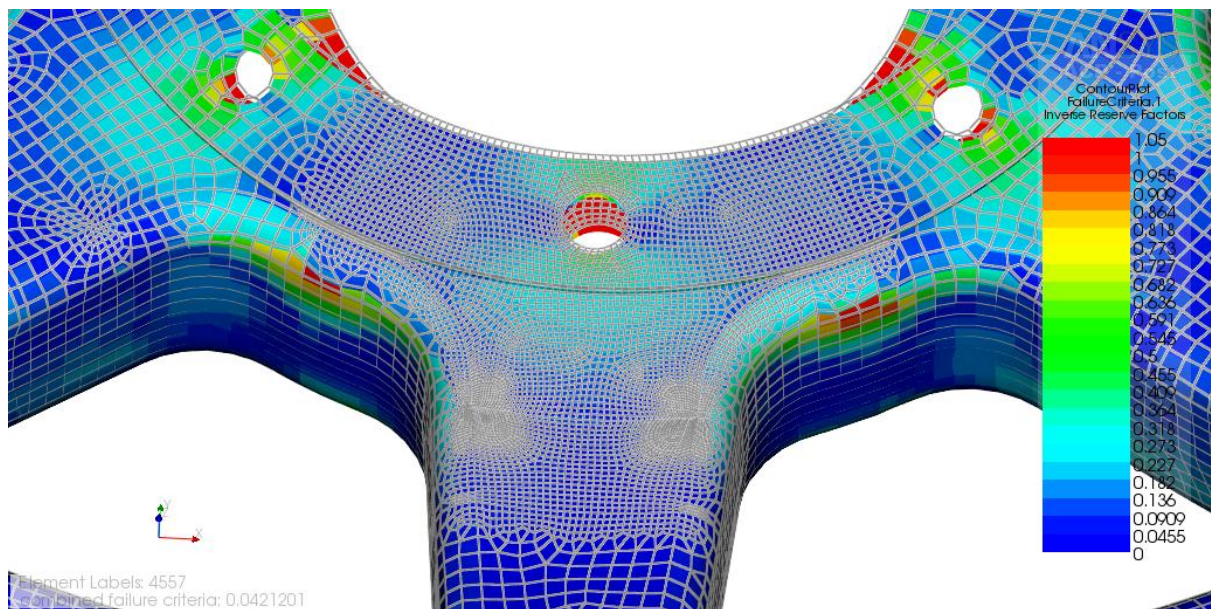


Figure 75: IRF - Transverse Strain Mode: Inner Section - Passenger Rim

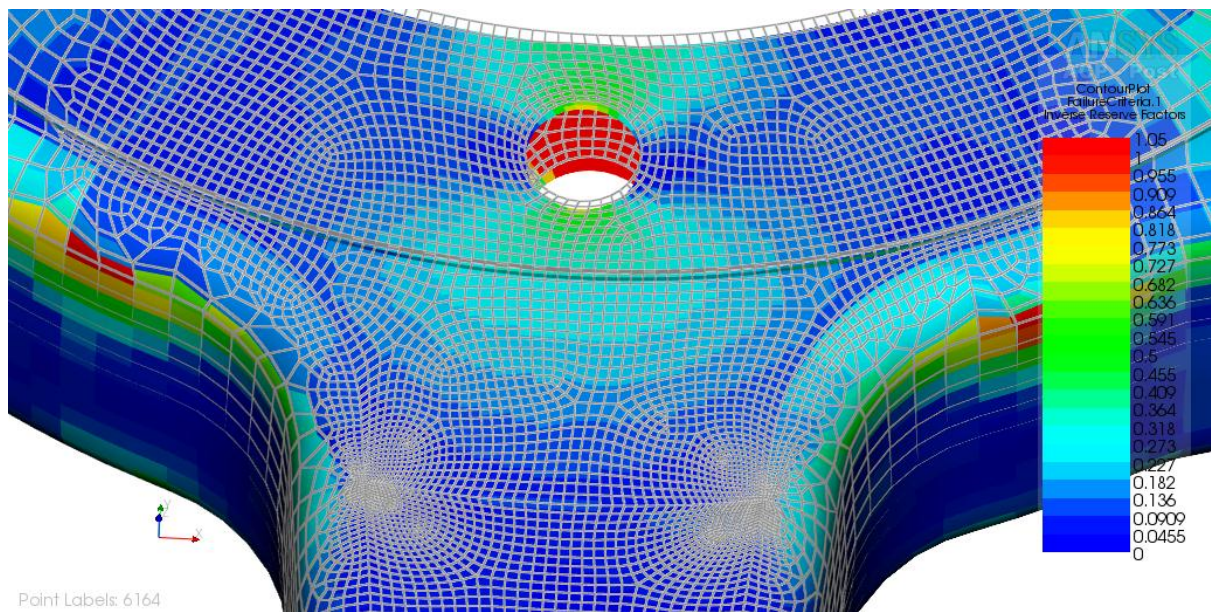


Figure 76: IRF - Transverse Strain Mode: Inner Section - Passenger Rim

The IRF in the in-plane shear strain mode is illustrated in Figure 77 to Figure 79. The IRF (Figure 77) in the spokes was 0.273 on the outer section. The IRF (Figure 78, Figure 79) in the spokes was 0.318 on the inner section.

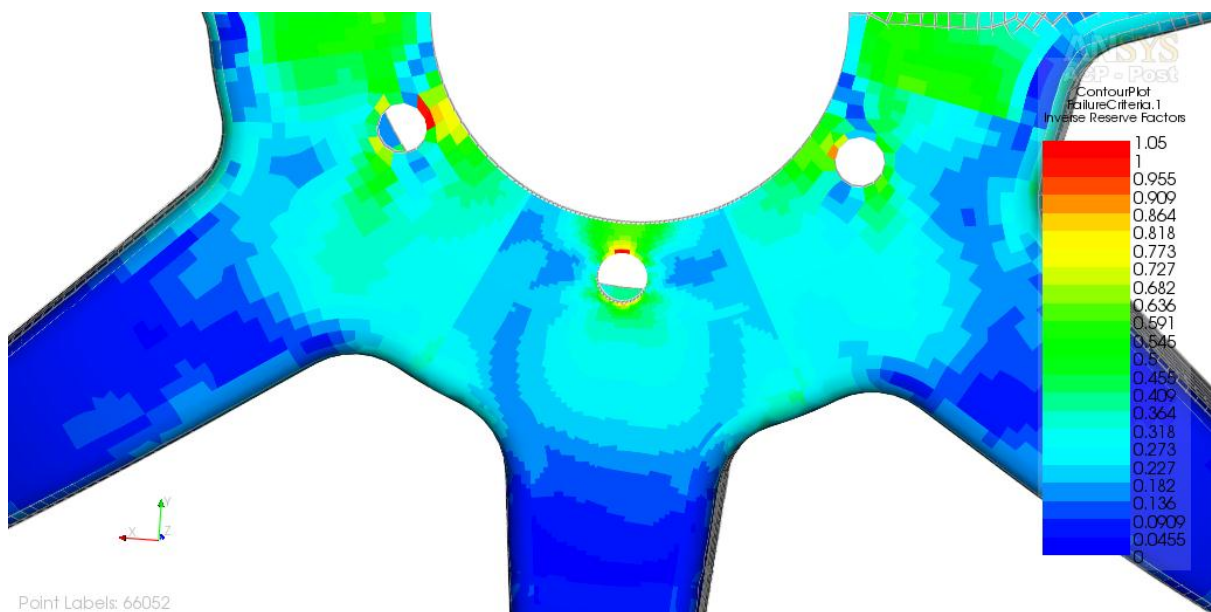


Figure 77: IRF - In Plane Shear Strain Mode: Outer Section - Passenger Rim

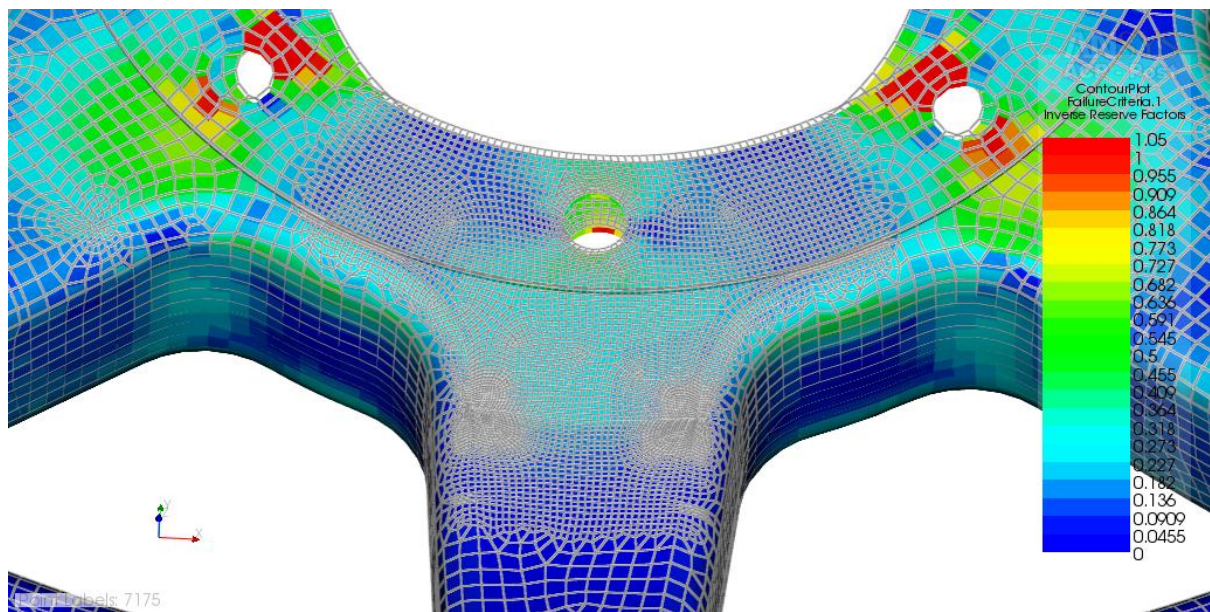


Figure 78: IRF - In Plane Shear Strain Mode: Inner Section - Passenger Rim

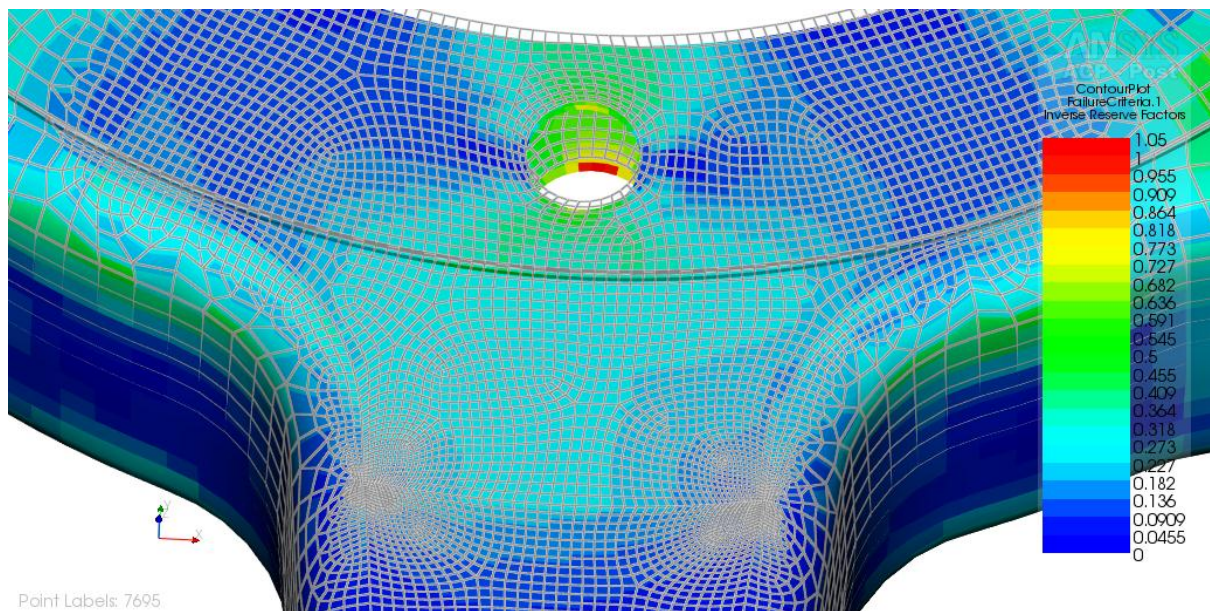


Figure 79: IRF - In Plane Shear Strain Mode: Inner Section - Passenger Rim

In summary the inverse reserve factor in the hub section was above 1, which was expected because the hub region was not modelled accurately. The hub region was modelled without the aluminium hub. The IRF from the spoke to the rim section was below 1 and relatively low. This indicates a low risk of static failure. The maximum strain patterns are similar to the Ducati rim exposed to 700 Nm. Table 14 illustrated an average 60% improvement in the IRF of the passenger car rim in comparison to the Ducati rim exposed to 2000 Nm. Section 7.2.2 indicated that the spoke section had a higher probability of failure in the shearing (in plane shear) mode, than matrix

Design of a Carbon Fibre Passenger Car Rim

(transverse strain) and fibre (longitudinal strain) mode in accordance with the maximum strain failure criterion.

Table 14: Comparison of the Ducati (2000 Nm) and Passenger Rim IRF

IRF	Ducati Rim (2000Nm)		Passenger Car (2000Nm)		Difference	
	Inner Spoke	Outer Spoke	Inner Spoke	Outer Spoke	Inner Spoke	Outer Spoke
ϵ_{1} Mode	0.409	0.409	0.136	0.136	67%	67%
ϵ_{2} Mode	0.409	0.636	0.136	0.227	67%	64%
ϵ_{12} Mode	0.636	0.682	0.318	0.273	50%	60%

Chapter 8: Discussion and Conclusion

8.1 Discussion

In the process of designing a carbon fibre passenger car rim, it was essential to correlate the FEA and the experimental strain results of the 1098 Ducati rim as illustrated in Table 5. This assisted in validating the finite element technique of the carbon fibre passenger car rim. The Ducati rim was used as a benchmark in that it is a proven product and meets all the necessary specifications. The Ducati rim was experimentally tested in accordance with the SAE J328 cornering fatigue test specification. The rim flange was fixed and constrained while a force was applied to the hub. The force was applied 1 m away from the hub, thereby resulting in a bending moment and simulating the cornering fatigue test.

The cornering fatigue test on the Ducati rim was conducted on the 09/06/2010 by Kienhöfer. The results of the experimental analysis illustrate:

- The zero static voltage results obtained were stable, and indicated a low drift.
- Channel 03 (back face of spoke 45 degrees) measured the highest strains of 448.9 $\mu\epsilon$ and - 465.1 $\mu\epsilon$ during tension and compression. Channel 01 (front face of spoke 45 degrees) experienced strains of 254.2 $\mu\epsilon$ and -245.8 $\mu\epsilon$ during tension and compression. The highest strains were along the 45 degrees direction on the spokes.
- Channel 02 (back face of spoke 0 degrees) measured the lowest strains at 120.4 $\mu\epsilon$ and - 137.6 $\mu\epsilon$ respectively during tension and compression. Channel 0 (front face of spoke 0 degrees) experienced strains of 173.8 $\mu\epsilon$ and -165.2 $\mu\epsilon$ respectively during tension and compression. This indicates that the spokes are well re-enforced in the 0 degrees direction along the spoke.
- The strain gauges experienced their highest strains, when the force application direction aligned with the orientation of the strain gauges (instrumented spoke). This was evident in the phase differences between the channels in Figure 10.

- Figure 10 illustrates that the strain gauges experienced two peaks. The peaks illustrate compression and tensile phases during the rotation of the rim. A sinusoidal relationship was visible between the strain and time as the wheel was rotated. These findings are similar to the findings of Wang et al. [6], with respect to the strain, time and rotation of the wheel.
- In an ideal situation, the strain gauge results would be utilised to calculate the longitudinal, transverse, and the in-plane shear strain. The absence of a third strain result on the front and back surface limited the strain calculations (longitudinal, transverse and the in plane shear strains). Therefore the strain gauge results were compared to the FEA strains using equation 2.4.

The experimental strain gauge results were used to validate the FEA model. The FEA model of the 1098 Ducati was developed using ACP. The CAD model was prepared by converting the solid model into a surface model. The surface model allowed for material design of the model in the FEA environment. The material design was done in ACP (pre), which entailed the segmentation, material properties, orientation and the stacking sequence of the plies. The results in this section were instrumental in understanding the strains the rim was exposed to. The aspects are highlighted below:

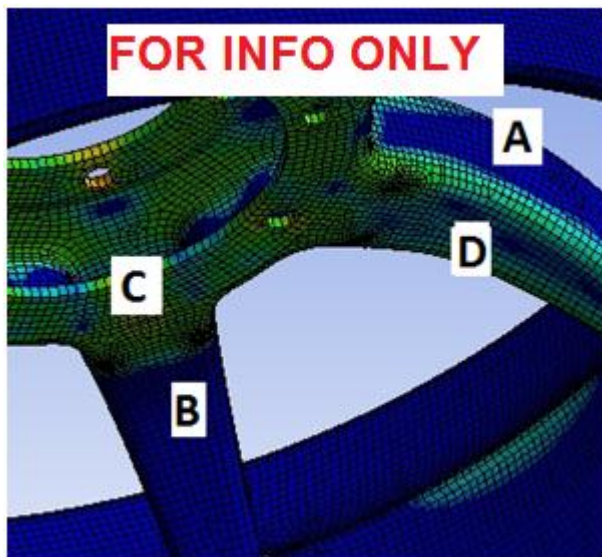


Figure 80: Example of Strain Variation

- The correlation between the experimental and FEA results was within 25%. The longitudinal, transverse, in plane shear strain on spoke were utilised to

calculate the strain in the 0 and 45 degree direction as illustrated Table 5. The 25% correlation was deemed acceptable.

- The hub section experienced the highest strain. This was expected as this was the attachment point for the load application. The high values around the bolt holes, was due to the stress raisers (concentration) created by removed material (attachments holes). The fact that the aluminium hub was not part of the analysis was noted. The results in the hub region were overlooked as they were not modelled accurately. The hub results do not need to be accurate as the focus point was the spoke. The reason the results in the spokes are still valid was that the overall constraints are still the same.
- The spokes experienced higher strain at the transition zone C from the hub to spokes as illustrated in Figure 80. Section C includes the spoke to spokes sections. The load was applied directly above spoke B, but spoke D experienced the highest strains along the spokes, which illustrated the moment due to the force. The strains were higher on the curvature corners of the spokes, and lower on section A of the spokes.
- The strains were generally higher at the point of the force application, transition between segmentations and where there was a change in fibre direction.
- The maximum strain failure criterion indicated that the Ducati rim was durable. The inverse reserve factor were relatively low (below 1) on the spokes and the rim. The inverse reserve factor in the hub section was above 1, which was expected because the hub region was not modelled accurately. The hub region was modelled without the aluminium hub and the results should be overlooked.
- Section 6.2.2 indicated that the spoke section had a higher probability of failure in the shearing (in plane shear) mode, than matrix (transverse strain) and fibre (longitudinal strain) mode in accordance with the maximum strain failure criterion. This indicates the rim is highly unlikely to experience static failure.

The Ducati rim was exposed to 2000 Nm in order to evaluate the strains (longitudinal, transverse and in plane shear). This assisted in quantifying the

improvement in the passenger rim design. The passenger rim was designed for a 2000 Nm bending moment. The design process for the stacking sequence and ply orientation was iterative. The final layup process is detailed in Table 7. The thickness variation (Figure 62 and Figure 63) of the rim; varies from 6.2mm thick hub to a 4.04 mm thick spokes and a rim section of 2.16 mm (beads excluded). The thickness change in comparison to the current rim is illustrated in Table 15. The results are discussed below:

Table 15: Thickness Comparison of the Rims

	Thickness Comparison		
	Ducati Rim	Passenger Car Rim	% Change
Hub (mm)	4.1	6.2	51.22%
Spoke (mm)	2.5	4.04	61.60%
Rim Section (mm)	1.8	2.16	20.00%

- The strains in the 0 and 45 degree direction on the spoke were calculated using equation 2.4. Table 12 illustrates that the passenger rim generally experienced higher strains in comparison to the Ducati rim exposed to 700 Nm. Table 13 illustrates that the passenger rim resulted in an average 85 % improvement in the strains when compared to the Ducati rim when exposed to 2000 Nm.
- The maximum strain failure criterion of the passenger car rim is indicated in section 7.2.2. The inverse reserve factor in the hub section was above 1, which was expected because the hub region was not modelled accurately. The hub region was modelled without the aluminium hub. The passenger car rim experienced higher strains than the Ducati rim exposed to 700 Nm, but the inverse reserve factor from the spoke to the rim section was below 1. This indicates low risk of failure. The inverse reserve factor patterns are similar to the Ducati rim. Since the Ducati rim was the benchmark, this proves that the passenger car rim will not fail in service.
- Section 7.2.2 indicated that the passenger rim spoke section had a higher probability of failure in the shearing (in plane shear) mode, than matrix (transverse strain) and fibre (longitudinal strain) mode in accordance with the

maximum strain failure criterion. Table 14 illustrated an average 60% improvement in the inverse reserve factor of the passenger car rim in comparison to the Ducati rim exposed to 2000 Nm.

The design utilises the available shapes and material from the original design. The designed carbon fibre passenger car rim weighs 3.56 kg in comparison to the average weight of 17" inch aluminium rims of 9.42 kg [39]. This illustrates a weight saving of 62.2%.

8.2 Conclusion and Recommendations

In conclusion a carbon fibre passenger car rim can be designed and manufactured. The main steps that were carried out to substantiate the feasible use of carbon fibre in a passenger car rim are detailed below:

- The correlation between the experimental and FEA was within 25%. This validated the finite element technique of the carbon fibre passenger car rim.
- The Ducati and passenger car rim experienced the highest strains in the hub region. This was expected as this was the attachment point for the load application. The high values around the bolt holes, were due to the stress raisers (concentration) created by the removed material (attachments holes). Since the hub was not modelled accurately, the results in this region were neglected. The passenger car rim spoke experienced higher strains when compared to the Ducati rim.
- The strain patterns in the transition zone and regions where there was a change in fibre direction were generally higher.
- The maximum strain failure criterion indicated that the Ducati and passenger car rim have a low probability of static failure.
- In comparison to aluminium rims of the equivalent size, a weight saving of 62.2% should be expected from the carbon fibre passenger car rim.
- Therefore a passenger car rim is feasible based on the principles listed above.

Further work can be done to:

- Experimentally measure of the strains on the Ducati rim, using 45 degree rosettes to measure all three surface strain components.
- Redesign the aluminium hub attachment for the passenger car carbon fibre rim.
- Evaluate and reduce the probability of the carbon fibre degrading due to high temperatures due to the heating on the brakes.
- Build the designed passenger rim and test it experimentally

References

1. Muthuraj, R., Badrinaryanan, R. and Sundararajan, T. (2011) "Improvement in the Wheel Design Using Realistic Loading Conditions-FEA and Experimental Stress Comparison." SAE International. SAE Papers 2011-28-0106.
2. Jacobs, H. (2002), "The Fatigue and Tensile Properties of A356 Aluminium Alloy Wheel in Various Post Cast Conditions", Department of Mechanical Engineering Rand Afrikaans University, May 2002.
3. Raju, PR., Satyanarayana, B., Ramji, K., and Babu, KS. (2008) "Evaluation of Fatigue Life of Aluminium Alloy Wheels Under Bending Loads." Fatigue and Fracture of Engineering Material and Structures, Department of Mechanical Engineering, SRKR Engineering College, India.
4. Compere, AL., Griffith, WL. and Leitten, CF. (2001) "Improving the Fundamental Properties of Line-Based Carbon Fibre for Transport Applications.", Oak Ridge National Laboratory.
5. BlackStone Tek, www.blackstonetek.com, online, last cited 01/01/13.
6. Sali, A., Turner, G. and Kienhöfer, F. (2010) "The Novel Use of Carbon Fibre in Designing an Automotive Car Rim." Seventh South African Conference on Computational and Applied Mechanics (SACAM 2010).
7. Grech-Cumbo, U.M., (2007) "Feasibility of a Carbon Fibre Racing Car Wheel." University of Witwatersrand
8. Kienhöfer, F.,(2010) "Experimental Results: Strain gauge results of 1098 Ducati Rim.", The University of the Witwatersrand.
9. Radulescu, AV., Cananau, S. and Radulescu, L. (2012) "Mechanical Testing Methods Concerning the Stress Analysis For a Vehicle Rim." Volume 2, pp. 33-39, Romania, University Politehnica Burcharest.
10. Kinstler, J. (2005) "The Science and Methodology of SAE Wheel Fatigue Test Specifications." SAE International. SAE Papers 2005-01-1826.
11. Mohammed, K., Vinothkumar, S., Sabarinathan, S., AnilKumar, N. (2011) "Simulation and Test Correlation of Wheel Impact." SAE International. SAE Papers 2011-28-0129.

12. Wang, X. and Zhang, X. (2010) "Simulation of Dynamic Cornering Fatigue Test of a Steel Passenger Car Wheel." International Journal of Fatigue 32, pp. 434–442, Elsevier.
13. Society of Automotive Engineers. (2001) "Wheels-Passenger Car and Light Truck Performance Requirements and Test Procedures." SAE International, SAE Handbook J328.
14. Karandikar, HM. and Fuchs, W. (1990) "Fatigue Life Prediction For Wheels by Simulation of the Rotating Bending Test." SAE International, SAE Papers 900147.
15. Guo, M., Bhandarkar, R. and Lin, B. (2004) "Prediction of a Cast Aluminium Wheel Using Finite Element Analysis." SAE International, SAE Papers 2004-01-1581.
16. Fischer, G. And Grubisic, VV. (1998) "Design Criteria and Durability Approval of Wheels Hubs." SAE International, SAE Papers 982840.
17. Kocabicak, U. And Firat, U. (2001) "Numerical Analysis of Wheel Cornering Fatigue Tests." Engineering Failure Analysis 8, pp. 339-354.
18. Riesner, M. and DeVries, RI. (1983) "Finite Element Analysis and Structural Optimization of Vehicle Wheels." SAE International. SAE Papers 830133.
19. Wang, L., Chen, Y., Wang, C., and Wang, Q. (2010) "Fatigue Life Analysis of Aluminium Wheels by Simulation of Rotary Fatigue Test." Journal of Mechanical Engineering 57, pp. 31-39, China, School of Mechanical Engineering, Nanjing University of Science and Technology.
20. Statistics South Africa (2010) "Motor Trade Industry, 2009." Statistical Release P6301, <http://www.statssa.gov.za/publications/P6301/P63012009.pdf>.
21. Tsuboi, U. (1998) "Cultural Observations on the History of Wheels." SAE International. SAE Papers 980617.
22. Ashby, MF. (1999) "Material Selection in Material Design." Chapter 6, pp. 119-120.
23. Baffet, G., Charara, A. and Lechner, D. (2009) "Estimation of Vehicle Sideslip, Tire Force and Wheel Cornering Stiffness." Volume 17, Issue 11, pp. 1255-1264, Elsevier Science.

24. Pereira de Carvalho, C., Voorwald, HJ. and Lopes, CE. (2001) "Automotive Wheels- An Approach for Structural Analysis and Fatigue Life Prediction." SAE International. SAE Papers 2001-01-4053.
25. TÜV (1998) "Directives on Testing of Special Wheels for Cars and Motor Cycles." Road Traffic Licensing Regulation, 30 STVZO
26. Euwa Standards (2006) "Test Requirements for truck steel wheels." ES 3.11, EUWA.
27. Kaw, AK. (2005) "Mechanics of Composite Material." Second edition, London, CRC Taylor and Francis.
28. Efunfa, http://www.efunda.com/formulae/solid_mechanics/composites/comp_lamina_principal.cfm, online, last cited 01/09/13.
29. Efunfa, http://www.efunda.com/formulae/solid_mechanics/mat_mechanics/strain_gage_rosette.cfm, online, last cited 01/09/13.
30. Hsu, Y., Wang, S. And Liu, T. (2004) "Prediction of Fatigue Failures of Aluminium Disc Wheels Using the Failure Probability Contour Based on Historical Test Data." Journal of the Chinese Institute of Industrial Engineers, Vol. 21, No. 6, pp. 551-558.
31. Fleischhauer, M. and Koenen, J. (2008) "Non-Linear Simulation of a lightweight Composite Rim." JEC Magazine no. 45, www.jecomposites.com.
32. Potter, K. (1997) "An Introduction to Composite Products." First Edition, pp. 163, London, Chapman and Hall.
33. Giek, JE. And Noll, WD. (1980), "Composite Wheels." SAE International, SAE Papers 800067.
34. Hexcel (2005), "Prepreg Technology." Publication no. FGU 017b.
35. ANSYS, http://ans2.vm.stuba.sk/html/elem_55/chapter4/ES4-181.htm, online, last cited 01/01/13.
36. Smith, B., Kienhöfer, F., (2015) "A Carbon Fibre Swingarm Design." R&D Journal of South African Institution of Mechanical Engineering, pp. 1-11.
37. ANSYS (2013), "ANSYS Composite PrepPost User`s Guide." ANSYS inc.
38. TÜV SÜD. "Wheel Testing." Munich, Germany, www.tuv-sud.com.
39. Wheel Weights, www.wheelweights.net, online, last cited 27/03/13.

40. SABS. "Motor Vehicles of Category M₁." Government Gazette 30917, www.sabs.co.za.
41. Ashby, MF. (2009) "Materials- A Brief History.", Philosophical Magazine Letters, March 2009.
42. Kretschmer, J. (1988) "Composites in Automotive Applications- State of the Art and Prospects.", The Institute of Metals, March 1988.
43. Ashby, MF. Allwood, MJ., Gutowski, GT. and Worrell, E. (2010) "Material Efficiency: A White Paper.", Elsevier B.V, November 2010.
44. Reinforced plastics (2011) "Carbon Fibre Market Poised for Expansion." 0034-3617/11Elsevier, pp 26-31, March 2011, www.reinforcedplastics.com.
45. Barbero, J. (2011) "Introduction to Composite Materials Design." Second Edition, pp 8- 226, New York, CRC Press.
46. Ashby, MF. and Jones, RH. (2002) "Engineering Materials 1: An Introduction to their Properties and Applications." Second Edition, Butterworth Heinemann.
47. Poursartrip, A. and Beaumont, PWR. (1986) "The Fatigue Damage Mechanics of a Carbon Fibre Composite Laminate: II- Life Prediction." Composite Science and Technology 25, pp 283-299.
48. Giger, M. and Ermanni, P. (2012) "Development of CFRP Motorcycle Rims Using Evolutionary Algorithms.", CH-8092 Zurich, Switzerland, <http://www.structures.ethz.ch/>.
49. Hibbeler, RC. (2004) "Engineers Mechanic Dynamics." Third edition, pp 377,378,576, Prentice Hall.
50. Zuo, ZH., Xie, YM. and Huang, X. (2011) "Reinventing the Wheel." Journal of Mechanical Design, Vol. 33, School of civil, Environmental and Chemical, www.asme.org.
51. Rao, K., Rastogi, S., Upadhyaya, H., Sanmani, A., Hakeem, SA. and Narayana, KB. (2011) "Damage Tolerance Analysis of Aero Structural Components.", TATA Consultancy Services..

52. Stearns, C. (2000) "An Investigation of Stress and Displacement Distribution in a Aluminium Alloy Automobile Rim.", The Graduate Faculty of the university of Akron.
53. Garret, TK. (2001) "The Motor Vehicle", Reed educational and Professional Publishing Ltd.
54. Roeseler, W., Sarh, B. and Kismarton, M. (2007) "Composite Structures: The First 100 Years." 16th International Conference on Composite Materials, Kyoto Japan.
55. Hsu, Y. (2006) "Developing an Automated Design Modification System for Aluminium Disk Wheel." 10th International Conference on CSCW, China.
56. Hibbler, RC. (2005) "Mechanics of Material." 6th Edition, pp. 585-642, Prentice Hall

Appendix A

Micromechanics of composite material

In micromechanics a combination of two isotropic materials, is characterised as an equivalent, homogenous, anisotropic material [45]. The stiffness of the indicated material is described by the listed properties in Figure 81.

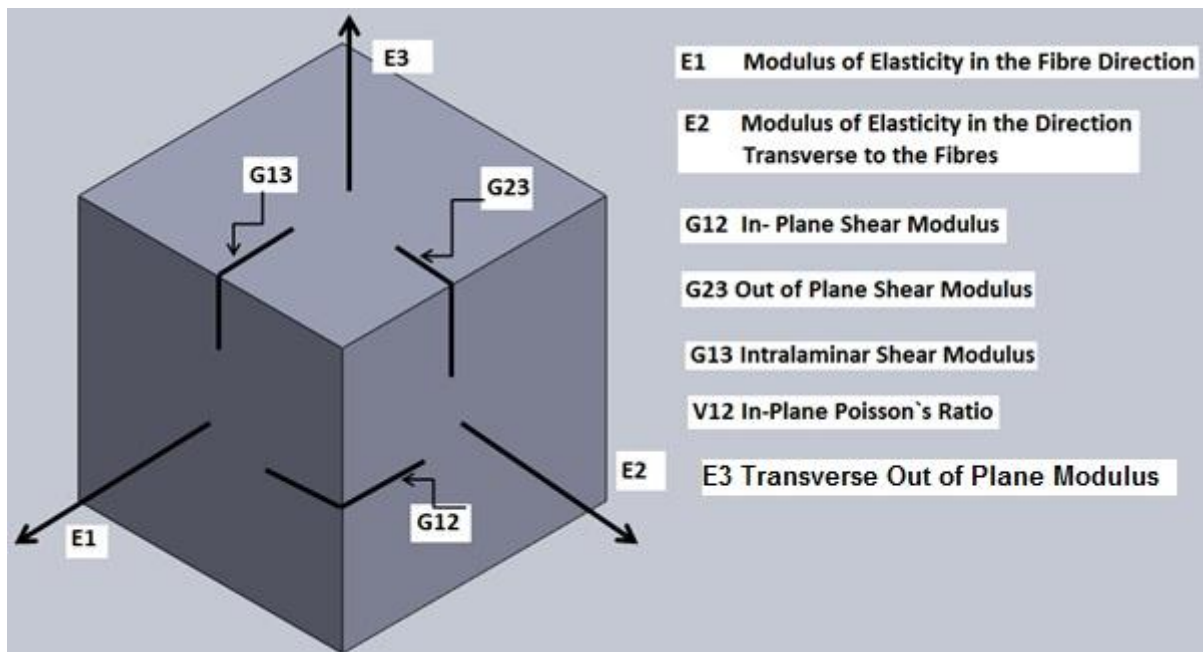


Figure 81: Stress Illustration on Cube [edited 45]

Longitudinal Modulus

The modulus of elasticity in the fibre direction is based on the assumptions [44]:

- Strains in the direction of the fibre are the same in the matrix and the fibre.
- Homogenisation of composite (RVE – representative volume element)

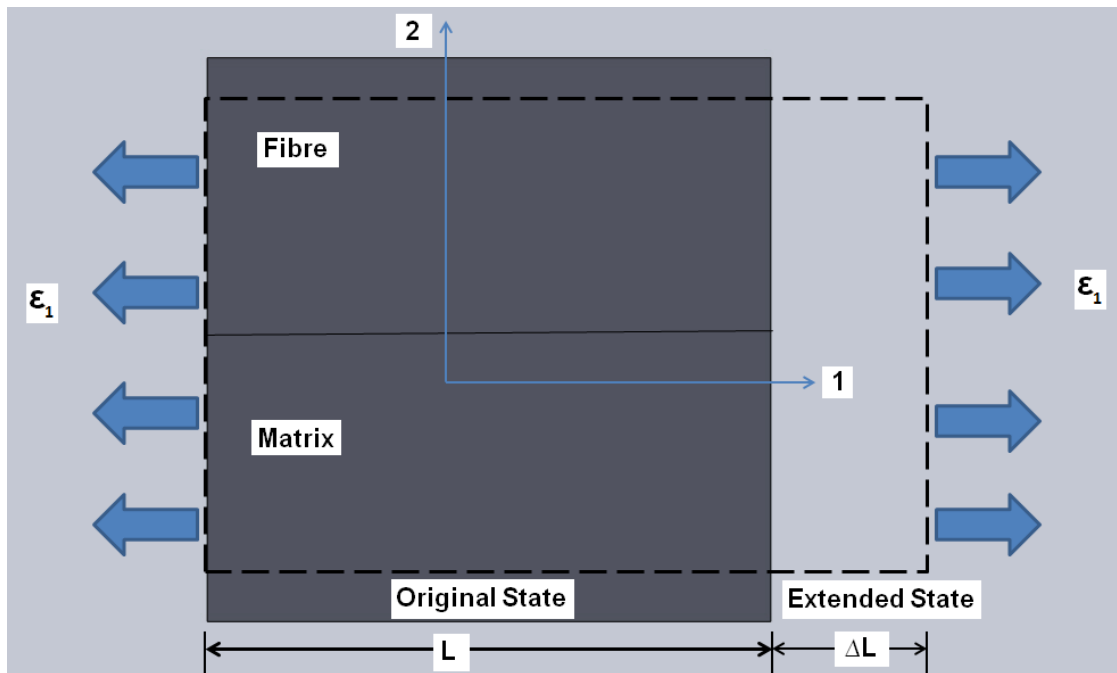


Figure 82: Longitudinal Uniform Strain Loaded on RVE [edited 45]

The area of the RVE is defined by area of the matrix and fibres as illustrated in Figure 82. The total area (A) of the RVE is the addition of the matrix Area (A_m) and fibre area (A_f). A Load (P) applied to the total area will result in the elongation of the RVE from its original state [25]. The strain (ϵ_1) is the ratio of the change in length (ΔL) to the original length (L). The load applied can be characterised by equation below. The stress (σ_1) – strain (ϵ_1) law in relation to matrix stress/elastic modulus (σ_m/E_m) and fibres stress/elastic (σ_f/E_f) are illustrated below [45]:

$$\sigma_f = \epsilon_1 E_f \qquad \sigma_m = \epsilon_1 E_m \qquad P = \sigma_f A_f + \sigma_m A_m$$

The longitudinal modulus is the upper limit estimate modulus [30]. The fibre-reinforced composite modulus cannot exceed the upper limit, since matrix strains are generally greater than fibre strains [45]. Therefore the longitudinal modulus is indicated below [45]:

$$E_1 = E_f V_f + E_m V_m \dots \dots \dots \text{(Eq. A1)}$$

Where:

E_f Fibre modulus

E_1 Longitudinal modulus

$V_f (A_f/A)$	Fibre volume percentage (%)
E_m	Matrix modulus
$V_m (A_m/A)$	Matrix volume percentage (%).
σ_f	Fibre stress
σ_m	Matrix stress

Transverse Modulus

The modulus of elasticity in direction of the transverse fibres is based on assumptions similar to longitudinal fibres. E_3 is generally estimated and assumed to be equivalent to the transverse modulus. In the transverse modulus the fibre strains and matrix strains act over a portion of the RVE width (W) [45]. The fibre strains ($\epsilon_f = \frac{\sigma_2}{E_f}$) and matrix strains ($\epsilon_m = \frac{\sigma_2}{E_m}$) respectively act over $V_f W$ and $V_m W$. The average strain (ϵ_2) is the total elongation of the RVE as represented below:

$$\epsilon_2 W = \epsilon_f W V_f + \epsilon_m W V_m$$

The transverse modulus is the lower limit estimate modulus [45]. Therefore the transverse modulus is indicated below [45]:

$$\frac{1}{E_2} = \frac{V_f}{E_f} + \frac{V_m}{E_m} \dots \dots \dots \text{(Eq. A2)}$$

Where:

E_2	Transverse modulus
σ_2	Transverse stress

In-Plane Poisson`s Ratio

Poissons Ratio is the negative ratio of the transverse strain (ϵ_j) to the axial strain (ϵ_x) [45]. Equation A3 provides an approximation of the Poisson`s ratio and is governed by the rule of mixtures as a function of fibre volume and matrix volume fraction [45].

$$v_{12} = v_f V_f + v_m V_m \dots \dots \dots \text{(Eq.A3)}$$

Where:

ν_{12} In-plane Poisson`s ratio

ν_f Fibre Poisson`s ratio

ν_m Matrix Poisson`s ratio

In-Plane Shear Modulus

Figure 83 illustrates the deformed composite due to in-plane shear. Equation 8 is a matrix dominated property in case of stiff fibres. Shear through the thickness (G_{13}) is assumed to be equal to in-plane shear (G_{12}) [45].

$$\frac{1}{G_{12}} = \frac{1}{G_{13}} = \frac{V_f}{G_f} + \frac{V_m}{G_m} \dots\dots\dots (Eq. A4)$$

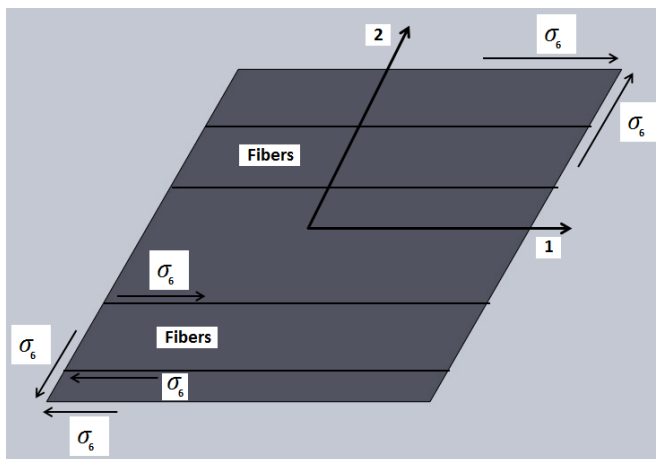


Figure 83: Illustration of In-Plane Shear [edited 45]

Where:

G_f Fibre shear modulus

G_m Matrix shear modulus

G_{12} In-plane shear modulus

Intra-laminar Shear Modulus

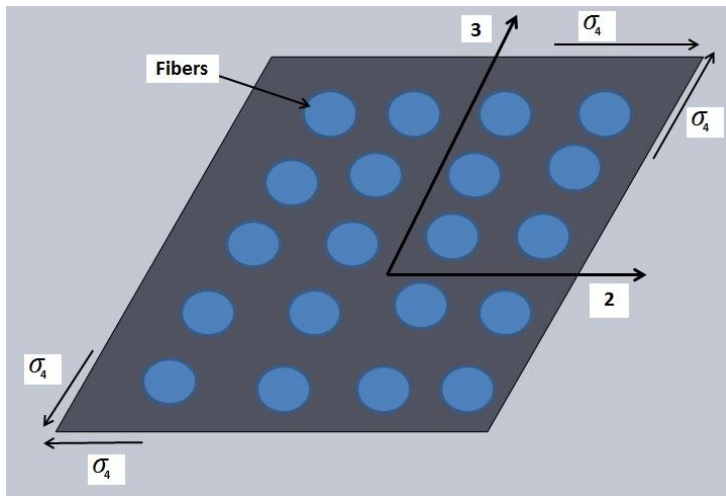


Figure 84: Illustration of Intra-Lamina Shear [edited 45]

Figure 84 illustrates the intra-laminar shear (G_{23}) acting across the thickness of the composite. This acts along the 3-2 plane as illustrated in equation A5. Therefore understanding composite micromechanics is crucial in FEA.

$$G_{23} = G_m \frac{v_f + \eta_4(1 - v_f)}{\eta_4(1 - v_f) + v_f \frac{G_m}{G_f}} \dots \dots \dots \text{(Eq. A5)}$$

Where:

$$\eta_4 = \frac{3 - 4\nu_m + \frac{G_m}{G_f}}{4(1 - \nu_m)}$$

Fatigue Failure

Fatigue analysis is performed to evaluate cyclic loading and the reduction of residual strength of the composite as illustrated in Figure 85 [48]. The cornering fatigue test requires that the composite wheel be evaluated for fatigue failure. The first step in fatigue analysis is to determine whether it is fibre or matrix dominated failure [45]. The composites resistance to failure is dependent on the composite, tensile and in-plane shear strength [32]. Carbon fibre usually experience drastic failure and glass fibres experience a long period in reduction of residual strength before failure [32]. Aramid fibres are the intermediate case between glass and carbon fibres as illustrated in Figure 85 [32].

The Weibull distribution is utilised to describe the variations in fatigue strengths [47]. Miners Rule can be utilised to predict fatigue life of composites under cyclic load, but this approach tends to overestimates fatigue life [47]. The fatigue life (N_f) is a function of the fixed stress ratio (R), initial damage (D_i), change in tensile strength ($\Delta\sigma$) and terminal damage (D_f) as illustrated in equation A6 and A7 [46].

$$\frac{dD}{dN} = f(\Delta\sigma, R, D) \dots \dots \dots \text{(Eq.A6)}$$

$$N_f = \int_{D_i}^{D_f} \frac{dD}{f(\Delta\sigma, R, D)} \dots \dots \dots \text{(Eq. A7)}$$

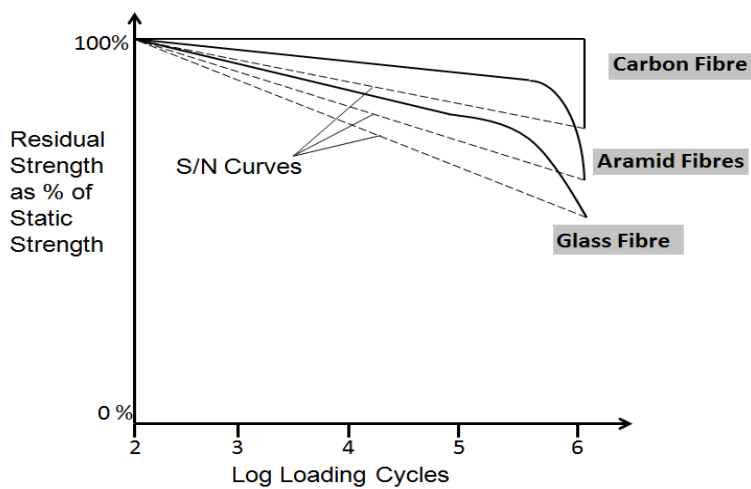


Figure 85: Residual Strength Curves of the Composites [edited-32]

Fatigue failure models aim at mathematically describing failure modes such as matrix micro-cracking and delamination growth rate, which are dependent on the strain energy release rate [45]. The fitness function of the rim will be based on the maximum strain failure criterion, which must remain below the limit value of 1 [45]. The maximum strain failure criterion distinguishes between compressive and tensile strengths of a lamina [25]. The maximum strain failure evaluates if the maximum allowable of the compression, tensile and shear strain is exceeded.